155p.

N64-20583

CAT. 06 CODE-1

POROUS IONIZER
DEVELOPMENT AND TESTING

by

M. LaChance, G. Kuskevics, and B. Thompson

prepared for

NATIONAL AERONAUTICS AND SPACE ADMINISTRATION

CONTRACT NAS3-2519

OTS PRICE 11.50 ph.

$

XEROX

E●S ELECTRO-OPTICAL SYSTEMS, INC., PASADENA, CALIFORNIA

FINAL REPORT

POROUS IONIZER
DEVELOPMENT AND TESTING

by

M. LaChance, G. Kuskevics, and B. Thompson

prepared for

NATIONAL AERONAUTICS AND SPACE ADMINISTRATION

12 May 1964

ELECTRO-OPTICAL SYSTEMS, INC.
300 No. Halstead Street
Pasadena, California

20583   ABSTRACT   A

Extensive research on the fabrication and performance testing of spherical powder tungsten ionizers is described. Research of the entire spectrum of powder metallurgy, from powder classification through .naracterization of the ionizers fabricated, is also described. Ionization testing of classified spherical powder ionizers, at three different levels of pore size refinement, was performed. The data presented indicate that successive refinement of pore structure leads to progressively improved ionization performance.   AUTHOR

TABLE OF CONTENTS

LIST OF ILLUSTRATIONS

LIST OF TABLES

SUMMARY

Extensive research on the fabrication and performance testing of spherica. powder tungsten ionizers is described. By holding constant all fabrication parameters except powder size distribution, an ionizer series of increasingly fine porosity was prepared. Thus it became possible to ascertain the effect of pore structural refinement on ionization performance at essentially constant levels of ionizer density and purity.

Research on the entire spectrum of powder metallurgy, from powder classification through characterization of the ionizers fabricated, is described. Ionization testing of classified spherical powder ionizers, at three different levels of pore size refinement, was performed. Performance of this select series is compared to that of relatively coar·.-structured H_2-reduced ionizers, available commercially in large size. The data presented indicate that successive refinement of pore structure leads to progressively improved ionization performance. Use of the finest classified starting powder increased the number of pores per unit area by a factor of >5, and reduced mean pore size by a factor of about 0.4 (based on comparison with ionizers from coarse unclassified powder). Thus, the improved ionization performance of the finer pore structures appears to be associated more closely with increased pores per unit area than with reduced pore size.

In recognition of the fact that fine pore structures have inherently less thermal stability (than coarse structures), due to their larger specific surface areas, a study of the stabilizing effect of tantalum and chromium on spherical tungsten powder was conducted. No stabilization of porous sintered tungsten by chromium was detected. On the other hand, tantalum is indicated to be very promising, markedly

reducing the sintering rate and increasing the thermal stability of tungsten. Microscopical evidence is presented to demonstrate, however, that addition of tantalum <u>in particle form</u> does not lead to fine uniform porosity, consistent with efficient ionizer performance. Use of an advanced technique, wherein fine tungsten microspheres are precoated with tantalum and with other probable (diffusion) barrier elements, forms the basis for the follow-on program NAS3-5248.

1. INTRODUCTION

This report describes research on the fabrication and ionization testing of porous ionizers. The research program is a logical continuation of the preceding NAS 8-2547 contract, details of which have been reported[1]. The primary objective of the present contract is the improvement of materials and fabrication technologies and development of ion emitter buttons for use in electrical propulsion systems.

The preceding research program[1] demonstrated numerous metallurgical advantages of using spherical tungsten powder as the basic element of ionizer construction. In addition, a marked improvement in ionization performance was demonstrated, despite the fact that relatively coarse spherical particles, having a broad size distribution, were used for construction. The combination of structural uniformity, good performance, and high purity of these first spherical powder ionizers indicated that further research was well warranted.

Toward the goal of further improved performance, the current program was designed by NASA to encompass the complete powder metallurgical process, from method of spherical powder classification through powder size analysis, ionizer fabrication, infiltration, infiltrant removal and pore characterization. This broad program led, in turn, to an unusually detailed knowledge of the ionizer buttons tested subsequently for ionization performance.

The scope of the research reported herein includes the following primary phases:

    I. Classification, Size Analysis, and Chemical Analysis of Spherical Tungsten Powder

---

1. M. LaChance and G. Kuskevics, "Ionizer-Reservoir Development Studies", Electro-Optical Systems, Inc. 2150 Final Report, May 1963.

2. CLASSIFICATION, SIZE ANALYSIS, AND CHEMICAL ANALYSIS OF SPHERICAL
    TUNGSTEN POWDER

The objectives of the work described in this section were (1) to
determine the optimum classification method for spherical tungsten
powder, (2) to obtain size fractions containing >75 percent by count
of particles within the 1-4, 3-6, and 4-8 micron diameter ranges, and
(3) to determine a reliable means of particle size analysis. Four
methods of classifying and three methods of particle size analysis were
tried. In addition, the initial purities of the powders used in the
research were determined.

2.1 Classification Methods and Results

2.1.1 Wilfley Tabling

Approximately one pound of spherical tungsten powder
was processed on a Craig Concentrator table. This unit had a 72" x 36"
bed, coated with polyurethane plastic, and was equipped with both con-
cave nd raised riffles running parallel to its length. The powder in
water slurry form was introduced into the feed box at the highest corner
of the table bed. Through the combined forces of flowing water, gravity
and longitudinal reciprocation of the bed, the powder was moved toward
the lowest or discharge corner.

Thirteen powder samples, one from each table riffle,
were collected and examined microscopically. All samples contained the
same variation in particle size as did the initial unclassified powder.
Thus the Wilfley test indicated no promise for the separation of tung-
sten microspheres. While it is believed that some degree of classifi-
cation may be achieved by modifying table design (shallower riffles,
riffle spacing, angle of incline, etc.) it is improbable that sufficiently
sharp separations could be obtained by this method.

2.1.2 Kinetic Water Film

A simple experiment was conducted to determine whether tungsten microspheres could be separated by the mechanism of differential velocity within a thin film of flowing water. For this, a jet of water was impinged tangentially onto a 23" x 16" glass plate, to yield a kinetic water film. The glass plate was inclined at angles varied between 10° to 15^C from horizontal and the water nozzle was center positioned at the lower (longer) edge. Spherical tungsten powder (as a slurry with methanol) was injected by eyedropper into the water stream, immediately in front of the nozzle tip.

Maximum water velocity occurring at the point of impingement, the film spread fan-wise over the plate and moved toward the lower edge. In such a pattern, it was reasoned that the largest and heaviest tungsten particles would move to the bottom edge to a position closest to the inlet, while the smallest particles would be carried up and outward to the furthest distance. In actual test, the following effects were noted:

1. adherence of the tungsten particles to the glass, with subsequent blocking of particle flow;

2. backing-up of the water film at the lower edge of the plate, due to surface tension, with horizontal movement of powder particles in the water trough thus formed;

3. agglomeration of the tungsten particles;

4. need for large water-to-powder volume.

The test was repeated with the lower edge of the glass plate rounded. Effect 2 was reduced, consequently, but not eliminated. It was concluded from these tests that classification in a kinetic water film was not feasible for fine spherical tungsten powder.

2.1.3 Water Elutriation

This method of classification is based on Stokes principle of free fall of a solid body in a fluid medium, assuming laminar or non-turbulent motion. According to Stokes' Law, terminal velocity of settling is given as:

$$v_T = \frac{2gr^2(\rho_s - \rho_f)}{9\eta} = (217.92r^2)\frac{\rho_s - \rho_f}{\eta}$$

Where

g is acceleration of gravity in cm/sec^2

r is particle radius in cm,

$(\rho_s - \rho_f)$ is differential density between solid and fluid, and

η is absolute viscosity of fluid in poise or gm/cm·sec.

For tungsten particles of $\rho_s = 19.3$ g/cm^3 in water at 25°C,

Where $\rho_f = 1.0$ g/cm^3 and

$\eta = (8.937)(10)^{-3}$ poise,

Stokes' expression reduces to

$$v_T = (4.459)(10)^5(r)^2.$$

Using this reduced expression, a multi-tube Morgan elutriator was designed according to the calculated values of Table 2-I. In operation, the water-tungsten mixture would enter the lower end of a vertical column 1.588 cm in diameter at a volume flow rate of 0.141 cm^3/sec. According to the calculation, the upward current would equal the terminal settling velocity, 0.071 cm/sec, of 8-micron diameter tungsten particles. Particles <8 microns in diameter would be carried upward and into the bottom of the next vertical column of 1.815 cm diameter, designed to suspend 7-micron-diameter particles, etc.

A Morgan elutriator was assembled for testing, with the first and smallest column of 1.6 cm diameter, to make a single separation of ⪤8 micron from >8 micron particles. This equipment is shown in Fig. 2-1. At the upper right of the photo is a 5-gal. reservoir

TABLE 2-I

TERMINAL VELOCITIES OF SETTLING OR TUNGSTEN MICROSPHERES IN 25°C WATER; ELUTRIATION TUBE DIAMETERS REQUIRED FOR EQUAL AND OPPOSITE WATER VELOCITIES, ASSUMING A VOLUME FLOW RATE OF 0.141 cm/sec

Particle Diameter, Microns	Particle Radius		r^2, cm²	$(10)^5 r^2$, cm²	Terminal Velocity, cm/sec	Tube Diameter (relative)	Finite Tube Diameter	
	Microns	cm					cm	inch
8	4.0	$(4)(10)^{-4}$	$(16)(10)^{-8}$	$(16)(10)^{-3}$	0.0713	1.000	1.588	0.625
7	3.5	$(3.5)(10)^{-4}$	$(12.25)(10)^{-8}$	$(12.25)(10)^{-3}$	0.0546	1.143	1.815	0.715
5	2.5	$(2.5)(10)^{-4}$	$(6.25)(10)^{-8}$	$(6.25)(10)^{-3}$	0.0279	1.600	2.541	1.000
4	2.0	$(2)(10)^{-4}$	$(4)(10)^{-8}$	$(16)(10)^{-3}$	0.0178	2.000	3.176	1.250
2	1.0	$(1)(10)^{-4}$	$(1)(10)^{-8}$	$(1)(10)^{-3}$	0.0045	4.000	6.352	2.501
1	0.5	$(0.5)(10)^{-4}$	$(0.25)(10)^{-8}$	$(0.25)(10)^{-3}$	0.0011	8.000	12.704	5.002

FIG. 2-1 VERTICAL-TUBE MORGAN WATER ELUTRIATOR

of "distilled water - .05 Vol. percent Aerosol" solution. This solution is introduced through a Tygon siphon into a constant-head bottle and then into the vertical feed system. At the top of the photo is a variable-speed stirring motor with stirrer in operating position. The tungsten feed powder (also in .05 percent Aerosol solution) is contained in a separatory funnel, the bottom end of which contains a hole sufficiently large for a drop-by-drop feed. This down feed combines with the water feed, flows through a capillary tube at the lowest part of the assembly, and into the elutriator tube proper. Flow rate of solution is carefully maintained at 0.141 cm^3/sec by measuring the volume discharge rate from the top of the elutriator tube.

In operation of the elutriator, difficulties with clogging and maintaining a constant volume-flow rate were encountered. Clogging of the U-tube (bottom of Fig. 2-1) was first observed. A 1-mm diameter capillary tube was substituted to increase linear velocity at this location. This reduced the clogging tendency, however, a second and more serious clogging then occurred in the conical inlet at the elutriator tube bottom. Clogging at this location was also reduced, but not eliminated, by a preliminary sedimentation and decantation step to remove the larger and heavier particles. The elutriator column was operated for a cumulative time of approximately 10 hours. Particles passed, totaling less than 1 gram, were examined microscopically and very few oversized particles were observed. However, because of the low yield and the clogging difficulties inherent with this design, no further tests were conducted.

2.1.4 Cyclonic Air

To obtain sufficient quantity of a sized tungsten powder for this research, various manufacturers of cyclonic-air powder separators were contacted. From among these, the Sharples Corporation of Bridgeport, Pennsylvania was selected, since this firm was equipped to classify small sample lots on a service basis, and to furnish complete particle-size analysis data for the fractions separated.

Two lots of Linde spherical tungsten powder (Electro-Optical Systems Lots D and E) were submitted to Sharples for separation in their K8 Super Classifier. The principle of operation of this unit is as follows. Feed material falls onto a rotating distributor which accelerates the powder, deflecting it downward into the center area of the classifying zone. Air flow, induced by an exhauster downstream from the classifier, enters the classification zone through a vane assembly. This assembly produces an air vortex of the proper angle for the separation desired. The vortex angle and rotor speed are adjusted to set the selected separation point. Particles coarser than the separation point are carried outward by centrifugal force, until they impinge on the coarse collector ring which guides them to the dual coarse discharge outlets. Particles finer than the separation point are carried inward by the drag force of the air vortex and pass into a fines discharge scroll, and then to the fines collector.

To determine the sharpness of separations achieved, both powder Lots D and E were analyzed by the Sharples Corporation. Results are presented in the following section.

2.2 Particle Size Analysis - Methods and Results

2.2.1 Micromerograph

Particle-size distribution of Lots D and E spherical tungsten powder, and of the powder fractions separated therefrom, were determined in a Sharples Micromerograph Analyzer. The Micromerograph consists essentially of three parts, described as follows:

1. Powder Deagglomerator

   The deagglomerating system consists of a source of high-pressure dried gas, a charging solenoid valve, a small pressure chamber, a "firing" solenoid valve, a powder chamber, and the deagglomerator proper. The deagglomerator itself consists of an accurately machined and polished cone which fits a mating

conical seat. The annular region between these surfaces forms the deagglomerating space. The spacing may be set to the desired value by turning a lever, which is calibrated directly in microns. When the "firing" button is pressed, the pressure chamber discharges through the powder chamber and carries the powder through the deagglomerator where the powder is dispersed by the viscous shearing action of the gas. By varying gas pressure and deagglomerator opening, controlled deagglomerating forces of the proper size may be created.

2. **Sedimentation Column**

Made of aluminum insulated with a fiberglass blanket, this tube is 85 inches long and 3-1/2 inches in inside diameter. The large settling distance (220 cm) compared with the relatively small dimensions of the burst of particles from the deagglomerator makes insignificant any difference in settling times of particles of the same size.

3. **Servo-Electronic Balance and Recorder**

The falling particles collect on the balance pan and are weighed by the current required to maintain the balance in the null position. Due to the action of the servo-electronic system, the total deflection of the balance pan is imperceptible to the eye. The record on the chart is, at any point, a measure of the total weight accumulated on the pan for a given interval of time from the start of the determination. In accordance with Stokes' Law, time of fall of a particle through the column is inversely proportional to the square of the particle diameter and to the density of the particle. A

simple transparent overlay template, incorporating
the constants of proportionality for the Micromero-
graph, provides the means for deriving the data for
plotting a complete particle-size distribution
curve.

Particle-size distribution data are given in Table 2-II
for Lot D tungsten microspheres prior to classification. These data
indicate that only 27.5 wt. percent of the particles were less than
10 microns in diameter. However, 27.5 percent by weight is equivalent
to 94.8 percent by number.

Nine fractions were separated from the Lot D micro-
spheres. Analyses data for these fractions, determined by Micromerograph,
are also given in Table 2-II. Here, brackets are drawn to indicate the
size range groupings containing the maximum numbers of particles. Photo-
micrographs of the unclassified Lot D powder and of Sharples' Run
Numbers 9, 7, and 1 are shown in Fig. 2-2. For these photomicrographs,
the particles were dispersed in a 0.5 percent aqueous solution of sodium
silicate and contained between thin glass slides. To provide adequate
contrast, the sample slides were photographed against a highly-polished
steel backing. In Fig. 2-2, it is important to note the coherence of
small particles (Run No. 1) and of small particles to large particles.
This agglomerating tendency is related, very probably, to the difficulty
encountered in water elutriation (previously described) and to the
problems associated with electronic particle counting (described sub-
sequently).

In order to obtain percentages of particles within
still narrower size ranges, as well as to increase the percentage of
usable powder, the Linde Company was requested to supply microspheres
having a much higher percentage of less than 10μ-diameter particles.
Ten pounds of a much finer powder (described subsequently as Lot E)
were produced and were analyzed by Micromerograph. Results are listed
in Table 2-III. Here the weight percentage of less than 10μ particles

TABLE 2-II

PARTICLE-SIZE DISTRIBUTION DATA FOR NINE FRACTIONS SEPARATED
FROM LOT D TUNGSTEN MICROSPHERES BY K8 AIR CLASSIFIER

Sharples Run No.	% of Particles	Particle Diameter Range, Microns																	
		1-2	2-3	3-4	4-5	5-6	6-7	7-8	8-9	9-10	10-11	11-12	12-13	13-14	14-15	15-16	16-17	17-18	>18
Unclass. Starting Material	By Wt.	0.7	0.8	1.5	3.0	3.0	4.5	4.5	5.0	4.5	5.5	5.0	5.1	5.4	5.5	5.1	5.1	5.2	30.6
	By No.	51.1	12.6	8.6	8.1	4.5	4.0	2.6	2.0	1.3	1.2	0.8	0.6	0.5	0.4	0.3	0.3	0.2	0.7
1	By Wt	5.4	16.4	31.5	31.3	10.4	4.1	0.9	Nil	--	--	--	--	--	--	--	--	--	--
	By No.	42.0	27.5	19.3	9.0	1.6	0.4	0.1	Nil	--	--	--	--	--	--	--	--	--	--
2	By Wt	1.4	8.6	19.6	32.4	23.0	9.8	4.6	0.6	Nil	--	--	--	--	--	--	--	--	--
	By No.	21.1	28.0	23.3	18.1	7.0	1.8	0.6	0.1	Nil	--	--	--	--	--	--	--	--	--
3	By Wt	Nil	3.3	12.7	34.5	30.2	11.9	5.8	1.6	Nil	--	--	--	--	--	--	--	--	--
	By No.	Nil	18.7	26.3	33.6	16.1	3.8	1.3	0.2	Nil	--	--	--	--	--	--	--	--	--
4	By Wt	Nil	1.1	8.4	24.1	32.4	21.3	8.4	3.7	0.6	Nil	--	--	--	--	--	--	--	--
	By No.	Nil	8.5	23.6	31.9	23.5	9.3	2.4	0.7	0.1	Nil	--	--	--	--	--	--	--	--
5	By Wt	Nil	Nil	3.0	13.4	22.6	30.2	20.4	7.1	3.3	Nil	--	--	--	--	--	--	--	--
	By No.	Nil	Nil	13.3	27.9	25.8	20.9	9.2	2.2	0.7	Nil	--	--	--	--	--	--	--	--
6	By Wt	Nil	Nil	0.8	8.4	19.6	24.8	18.2	11.5	7.8	4.5	2.7	1.6	0.1	Nil	--	--	--	--
	By No.	Nil	Nil	4.7	23.3	29.7	22.8	10.9	4.7	2.3	1.0	0.4	0.2	0.0	Nil	--	--	--	--
7	By Wt	Nil	Nil	0.2	6.7	15.7	22.6	17.9	13.6	9.9	6.0	3.7	2.5	1.2	Nil	--	--	--	--
	By No.	Nil	Nil	1.4	21.6	27.7	24.2	12.5	6.5	3.4	1.5	0.7	0.4	0.1	Nil	--	--	--	--
8	By Wt	Nil	Nil	Nil	1.4	6.0	7.9	11.7	13.0	12.9	11.5	10.6	8.1	6.8	4.0	2.7	2.0	1.4	Nil
	By No.	Nil	Nil	Nil	9.0	21.1	16.9	16.3	12.4	8.8	5.8	4.1	2.4	1.6	0.7	0.4	0.3	0.2	Nil
9	By Wt	Nil	Nil	Nil	Nil	2.9	6.1	7.4	8.2	8.9	9.3	10.0	10.7	11.0	10.0	6.3	3.4	2.1	3.7
	By No.	Nil	Nil	Nil	Nil	15.6	19.8	15.7	11.9	9.3	7.1	5.9	4.9	4.0	2.9	1.5	0.7	0.3	0.4

Bracketed cumulative values (By No.): Run 1: 88.9; Run 2: 72.4; Run 3: 78.6; Run 4: 79.0; Run 5: 74.6; Run 6: 75.8; Run 7: 73.5; Run 8: 66.7; Run 9: 72.3

Unclassified   Run No. 1
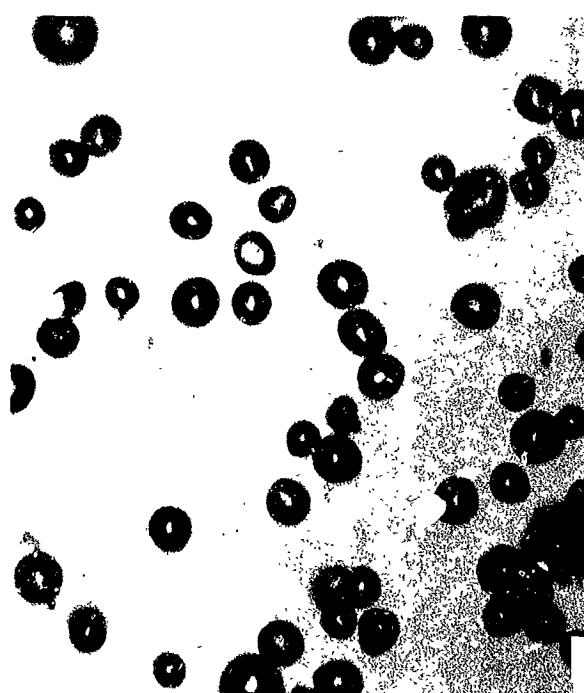
Run No. 7   Run No. 9

FIG. 2-2   PHOTOMICROGRAPHS AT 600X MAGNIFICATION OF LINDE SPHERICAL TUNGSTEN
           POWDER SHOWING INITIAL SIZE DISTRIBUTION (UPPER LEFT) AND THREE
           SIZE FRACTIONS OBTAINED FROM SHARPLES K8 CLASSIFIER.

TABLE 2-III

PARTICLE SIZE DISTRIBUTION DATA OBTAINED BY MICROMERO-APH ANALYSES

FOR LOT E SPHERICAL TUNGSTEN POWDER AND FOR FRACTIONS SEPARATED THEREFROM

(Powder fractions separated in Sharples K8 superclassifier)

Sharples Run No.	Percent of Particles	PARTICLE DIAMETER RANGE, Microns																		
		0-1	1-2	2-3	3-4	4-5	5-6	6-7	7-8	8-9	9-10	10-11	11-12	12-13	13-14	14-15	15-20	20-25	25-30	30-40
Unclassified Starting Material 2F	By Wt.	1.6	4.0	15.4	22.5	22.4	15.7	5.9	2.5	1.6	1.1	1.0	1.1	0.8	0.6	0.8	2.6	0.4	Nil	
	By No.	80.7	7.5	6.2	3.3	1.5	0.6	0.1	<0.1	<0.1	<0.1	<0.1	<0.1	<0.1	<0.1	<0.1	0.3	<0.1	Nil	
2C	By Wt.	Nil	5.2	24.9	29.5	22.7	11.8	5.9	Nil											
	By No.	Nil	37.0	38.3	16.5	6.0	1.7	0.5	Nil											
3	By Wt.	Nil	2.8	22.4	28.0	23.3	14.0	7.7	1.8	Nil										
	By No.	Nil	25.2	43.6	19.9	7.8	2.6	0.9	0.1	Nil										
4	By Wt.	Nil	Nil	9.4	27.4	31.8	16.3	8.9	4.2	Nil										
	By No.	Nil	Nil	34.5	36.7	20.0	6.3	1.9	0.6	Nil										
4A	By Wt.	Nil	Nil	4.4	24.7	32.7	23.2	10.0	5.0	Nil	Nil									
	By No.	Nil	Nil	20.1	41.0	25.6	9.9	2.6	0.8	Nil	Nil									
5	By Wt.	Nil	Nil	3.6	19.5	27.7	28.2	13.3	6.6	1.1	Nil									
	By No.	Nil	Nil	18.8	37.1	24.8	13.8	4.0	1.3	0.1	Nil									
6	By Wt.	Nil	Nil	Nil	8.0	23.3	29.7	22.3	11.9	4.8	Nil				Nil					
	By No.	Nil	Nil	Nil	25.3	34.6	24.2	11.0	3.8	1.1	Nil				Nil					
7	By Wt.	Nil	Nil	Nil	Nil	7.2	12.8	15.1	16.7	16.5	13.3	8.9	6.0	3.5	Nil					
	By No.	Nil	Nil	Nil	Nil	25.8	25.1	17.9	12.9	8.8	5.1	2.5	1.3	0.6	Nil					
7AC (coarse)	By Wt.	Nil	Nil	Nil	Nil	2.2	8.3	12.0	10.4	8.0	6.1	4.5	3.6	3.2	3.1	3.2	13.6	10.4	6.4	5.0
	By No.	Nil	Nil	Nil	Nil	13.7	28.3	24.8	14.0	7.4	4.0	2.2	1.3	0.9	0.7	0.6	1.5	0.5	<0.1	<0.1

Grouped (bracketed) By No. subtotals: 2F — 89.2; 2C — 91.8; 3 — 88.7; 4 — 88.7; 4A — 86.7; 5 — 94.5; 6 — 84.1; 7 — 81.7; 7AC — 80.8

is indicated to have increased (from 27.5 for Lot D) to 92.7, corresponding to an increase by count (from 94.8 for Lot D) to more than 99.1. The size distributions of Lot D and E powders are compared graphically in Fig. 2-3.

The special fine powder of Lot E was classified in the K-8 cyclonic air unit. Details of this separation are included in pages A1 through A6 of the Appendix as "K-8 Sharples Classifier Report No. 1374." Pages A2 and A3 describe the classifier setting, feed weights, yields, and losses; page A4 shows a flow sheet of the successive separations made; pages A5 and A6 show the particle-size distribution curves for the unclassified starting material and for the fractions separated, respectively. The classifier report indicates the use of a duplex process sequence, wherein each separation was performed twice at the same classifier settings to remove a greater percentage of fines, thus decreasing the percentage of such fines carried over as feed material in subsequent cuts. It is obvious that the duplex separation scheme must increase the sharpness of separations obtained.

Data extracted from the curves of pages A5 and A6, Appendix, were converted by calculation from percentage by weight to percentage by number. Results of this conversion are listed in Table 2-III, with brackets to show the narrowest groupings of the "percentage by number" data. In general, the fine powder fractions have narrower groupings than do the coarser fractions. Particle frequencies drop sharply at the fine ends of the distributions and tail-off rather gradually at the coarser ends. This tail-off effect is more pronounced for the coarser fractions, an inherent characteristic of cyclonic air classification. Data of Table 2-III also show that all $0-1\mu$ particles were lost during classification. This occurrence is referred to as blow-out. Finally, it is pertinent that classifier run Nos. 4 and 4A, performed at identical classifier settings, have very similar particle size distributions.
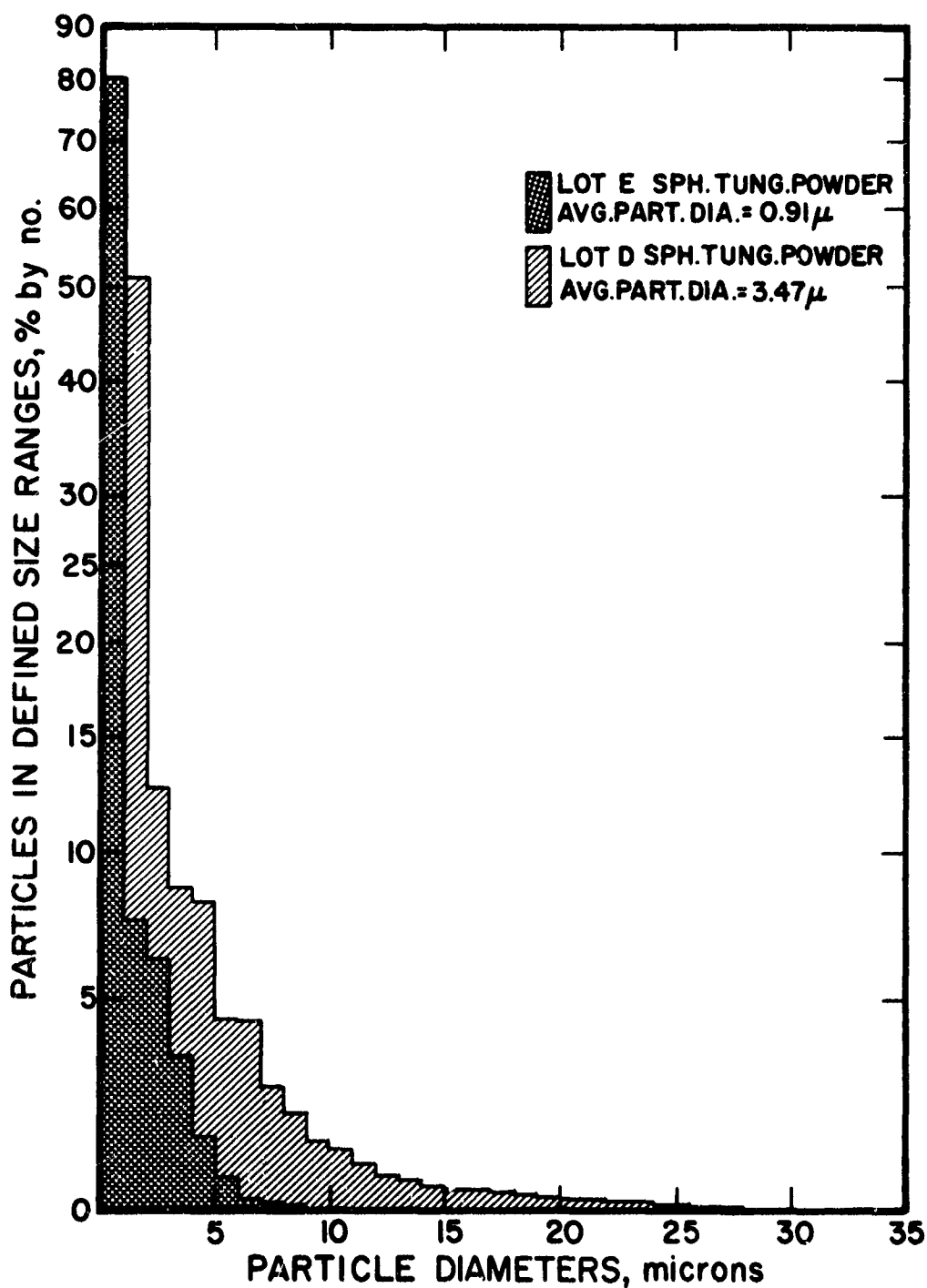
FIG. 2-3 GRAPHICAL COMPARISON OF PARTICLE SIZE DISTRIBUTION,
OBTAINED BY MICROMEROGRAPH ANALYSES, ON AS-PRODUCED
LOT D AND LOT E SPHERICAL TUNGSTEN POWDER

2.2.2 Microscopic Measurement

In order to check the Micromerograph particle distribution analyses, two microscopic counts were conducted on Lot D7 microspheres (refer to Table 2-II and Fig.2-2). Glass slides of the powder, dispersed in 0.5 percent sodium silicate solution, were prepared and optical traverses were made on a metallograph. Measurement of particle diameters was made with a calibrated Reichert micro-hardness reticule. This device permitted each particle to be focused within a square frame, the size of which was adjusted by means of a calibrated micrometer screw. Comparison of the two 500-particle counts with Micromerograph data is given in Table 2-IV. Here it is noted that the No. 1 and No. 2 counts are in reasonable agreement with each other, but that they are slightly offset from the Micromerograph determination. Considering the inherent difficulties of optical measurement, and the relatively limited number of particles measured, the data of Table 2-IV demonstrate the general agreement of the microscopic and Micromerograph methods. Further, the acceptance of the Micromerograph by industry as a rapid and economical tool for analysis serves to rule out use of the tedious and costly microscopic method.

2.2.3 Coulter Electronic Counter

In order to check particle size distribution data obtained by the Micromerograph and microscopic methods, four samples* of spherical tungsten powder were analyzed by the Coulter method. The analyses were performed at the Particle Data Laboratories of Elmhurst, Illinois.

The Coulter electronic method is described in the paper "Electronic Size Analysis of Subsieve Particles by Flowing through a Small Liquid Resistor", by R. H. Berg**, published by the ASTM in 1958. Briefly, "suspension of particles in conductive liquid flows through

---

* Powder fractions D8, E3, E6, and E7A.
** President of Particle Data Labs.

TABLE 2-IV

COMPARISON FOR LOT D, SHARPLES RUN NO. 7, TUNGSTEN MICROSPHERES
BETWEEN CONVERTED MICROMEROGRAPH WT. ANALYSIS DATA AND
TWO 500-PARTICLE COUNTS, PERFORMED ON METALLOGRAPH AT EOS

Particle Dia. Size Range, Microns	Calculated from Sharples Micromerograph Wt. Data	No. 1 Count on 500 Particles	No. 2 Count on 500 Particles	Combined No. 1 and 2 Counts of 1000 Particles
1-2	0.00	0.20	0.00	0.10
2-3	0.00	1.40	3.20	2.30
3-4	1.37	3.00	7.20	5.10
4-5	21.60	5.80	10.00	7.90
5-6	27.73 ⎫ 73.51	18.40 ⎫	20.40 ⎫	19.40 ⎫
6-7	24.18 ⎬	42.00 ⎬ 81.60	38.40 ⎬ 74.00	40.20 ⎬ 77.80
7-8	12.47 ⎭	21.20 ⎭	15.20 ⎭	18.20 ⎭
8-9	6.51	4.60	4.60	4.60
9-10	3.39	2.60	0.80	1.70
10-11	1.52	0.40	0.20	0.30
11-12	0.72	0.20	0.00	0.10
12-13	0.38	0.00	0.00	0.00
13-14	0.14	0.20	0.00	0.10

an aperture wich simultaneous flow of electric current, resulting in a series of electrical pulses, each pulse being proportional in magnitude to the volume of the particle causing it. The pulses are amplified, scaled, and counted to provide direct data for plotting cumulative frequency against particle size."

Each of the four powder samp'es submitted was tested about 10 times, with variable results, particularly at the small-diameter settings of the counter. Because of the variations encountered, particles below 1.81μ diameter were not counted and complete "particle count vs diameter" curves could not be drawn. Therefore, the percentage of total particles within the various particle size ranges could not be calculated.

An aqueous electrolyte, containing 4 percent $Na_4P_2O_7 \cdot 10H_2O$ and 0.5 percent sodium silicate, was used for all tests. This solution has been found by PDL to be effective in dispersing other metal powders. However, it apparently is not an effective, or even a stable, dispersant for tungsten microspheres. While these tests have not yielded the size distribution data desired, they do serve to confirm that spherical tungsten powder has a strong tendency to agglomerate. For this reason, it is not amenable either to wet classification or to wet size-analysis methods.

2.3   Selection of Classification and Size Analysis Methods

Based on the data of Table 2-III it was agreed, by technical representatives of NASA-Lewis and Electro-Optical Systems*, that classification by cyclonic air was the most feasible classfir... ion method available and that the program proceed using powder fractions E3, 6 and 7A (size distrib. graphs in Fig. 2-4). In order to increase the amounts of powder required for the wor', size fractions were thoroughly reblended as follows: 3 + 3A, 6 + 6A, and 7AF + 7A, which fraction combinations were produced at identical classifier settngs. On first consideration, one might think that such recombination merely

---

* Meeting of 12 June 1963 at Electro-Optical Systems, Inc.
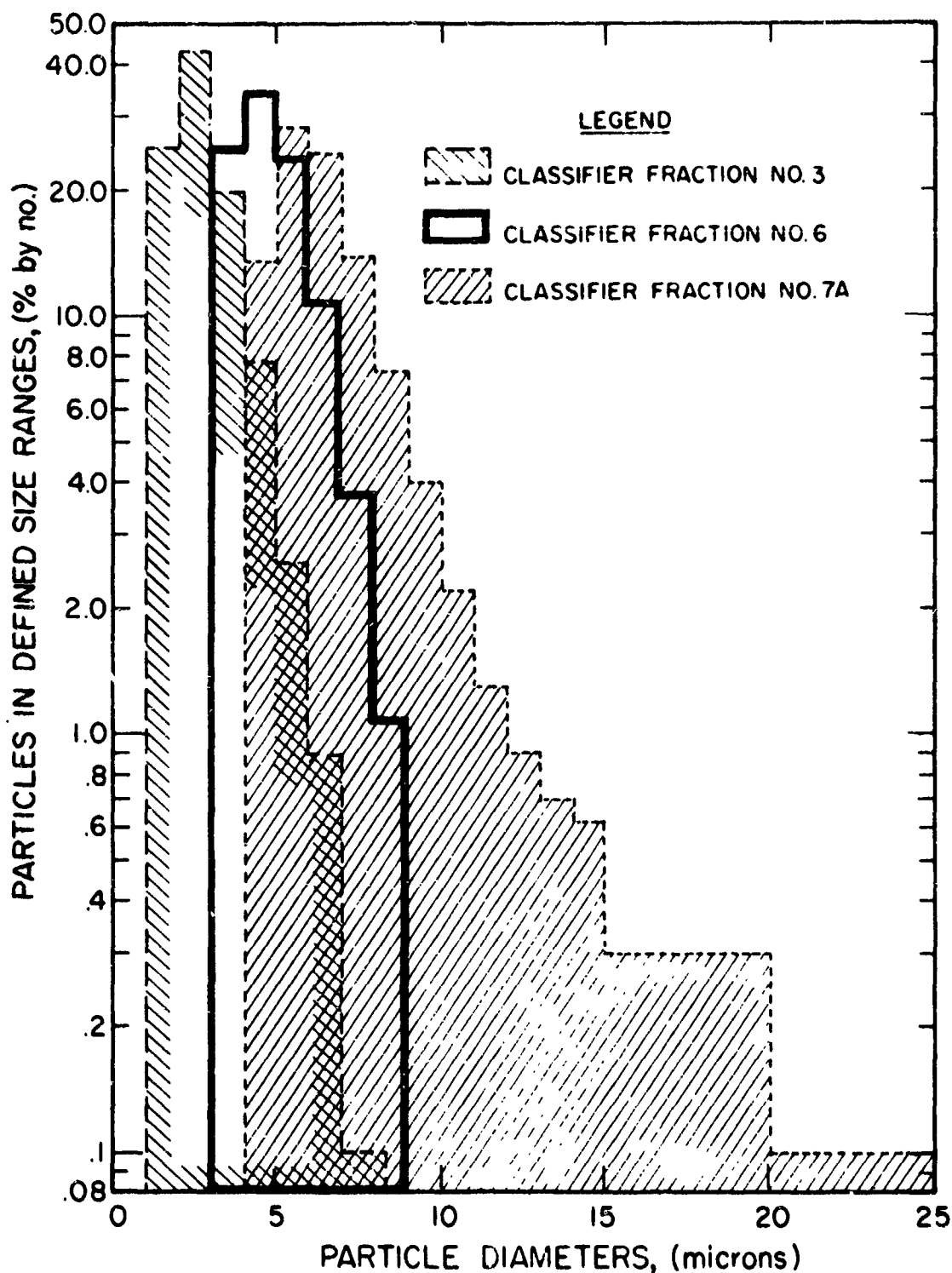
FIG. 2-4 GRAPHICAL COMPARISON OF PARTICLE SIZE DISTRIBUTION,
OBTAINED BY MICROMEROGRAPH ANALYSES ON CLASSIFIED
FRACTIONS OF LOT E SPHERICAL TUNGSTEN POWDER

reverses what is accomplished by the classifier. However, this is not the case. By duplicate separation steps, the classifier is given a double opportunity to remove fines from the relatively coarse feed powder, such that the second cycle fines are not available for capture by the subsequent classifier setting. It is believed that the duplex separations reported represent the best K-8 Classifier procedure, and that the sharpness of powder fractions obtained are as good as, or better than, those obtainable with other types of air classifiers. At this juncture it was decided, also, to utilize the Micromerograph method to characterize size distribution of the powders used. The inherent agglomerating tendency of fine tungsten microspheres when wet has been discussed. The Micromerograph method for analyses of dry powders is unsurpassed in the present state of the art.

2.4 Chemical Analysis Methods and Results

All chemical analyses performed under this contract were done by quantitative spectroscopy, with carbon by the standard conductometric method. For the former, an ARL 1.5-meter-grating spectrograph (linear dispersion first order of $6\overset{\circ}{A}$ per mm) was used. Line intensities were determined using an ARL Spectroline Scanner (densitometer) with 15 x magnification. The analyses were performed by the Materials Testing Labs.of Los Angeles. Standards were prepared as follows: To spectrographic grade WO_3 (of guaranteed 99.995+ percent purity) controlled amounts of 41 different elements were added (as oxides in the greater majority of cases). Amounts of impurity oxides added were such as to yield 1.42 weight percent of each impurity element in the master mixture. This master mixture was then dilution blended with various additional quantities of the base WO_3 to yield 7 standards, containing 1000, 300, 100, 30, 10, 3, and 1 ppm levels of each impurity element.

The purities of companion samples of coarse Lot C and of (relatively) fine Lot E spherical tungsten powders were determined. Results of these analyses are given in the certified reports of the Materials Testing Laboratories on pages A6 and A7 of the Appendix. Purities of the two powder lots are nearly identical, with Lot C having

a slightly lower copper content than, and approximately twice the carbon content of, Lot E. The cobalt and zirconium values, indicated as less than 100 ppm, were analyzed previously on Lot C powder to be approximately 1 ppm. Totaling the maximum impurity values of the certified reports and subtracting the totals from 100 percent, the purity of these powder lots exceeds 99.94 weight percent. This excludes, of course, the elements O, N, and H, not detectable by spectrographic means. Since the Lot C powder (used in the previous contract) was produced from the same tungsten and by the same method as Lot D powder (used in this research) it is reasonable to assume that the purity of the latter is also greater than 99.9 percent. A closely comparable baseline of initial powder purity is thus indicated for the previous and current research programs.

3. INFILTRATION OF COMPACTS OF SPHERICAL TUNGSTEN POWDER

An investigation of various infiltrants for sintered tungsten microspheres will be described in this section. The initial objectives of this phase of the research were to determine (for Cu-B, Cu-Be, Cu-P, Cu-Te, and pure silver infiltrants) the following:

(a) ability to infiltrate tungsten

(b) particle growth and alloying or other reactions
     (by photomicrograph)

(c) machinability of composites

(d) residual elements after vacuum distillation
     (by spectrographic analyses)

The research has encompassed the above objectives. In addition, a Cu-2 Fe infiltrant composition was included for comparison purposes, since it had been used in the previous research contract. A test to compare the wetting of tungsten by the various infiltrants was included and the compositional stability of the various infiltrant baths was determined as well.

Infiltration of porous tungsten is essential in facilitating machine operations (sawing, turning, milling, and grinding) where the relatively soft infiltrant acts as an effective lubricant. Infiltration also acts to protect the pore openings from closure by metal distortion during surfacing operations, being essential even in careful metallographic surface preparation.

Prior to the present contract, infiltration of sintered tungsten compacts had been done by immersing them in a Cu-2 wt. percent Fe bath at $1200^{o}C$ for 30 minutes. The investigation reported here compares the merit of six infiltrant compositions, one of which is essentially the same as the Cu-Fe alloy previously used. The experimental work

included: (1) preparation of infiltrant alloys and sintered tungsten compacts, (2) infiltration and wetability testing, (3) compositional stability of infiltrant baths, (4) machinability of infiltrants and infiltrated compacts, (5) microstructures of infiltrated compacts, (6) density and permeability of infiltrated compacts after vacuum distillation, (7) residual infiltrant elements in compacts after vacuum distillation, and (8) conclusions of infiltration study. The investigation will be discussed in this sequence.

3.1 Preparation of Infiltrant Alloys and Sintered Tungsten Compacts

Five binary copper-base alloys and pure silver were prepared for evaluation as infiltrants. The copper, silver, and tellurium constituents were of 99.999+ percent purity and were purchased from the American Smelting and Refining Co. Boron crystals of 99.15 percent purity from Matheson Coleman and Bell, C. P. grade Cu_6P_2 (fused lump) from Amend Drug and Chemical Co., Pechiney beryllium (lump) of 99.25+ purity furnished by ASD-Wright Patterson, and high purity electrolytic iron were used. The binary copper-base compositions were prepared with 2 atom percent of the additives B, Be, Fe, P, and Te. Constituents were sealed under vacuum in quartz capsules and heated to $1200^{\circ}C$ for 2 hours, to effect complete melting and/or solution of the additives and homogeneous alloying.

The porous sintered tungsten to be infiltrated was fabricated from Lot D spherical powder, size fraction 8. The powder was comprised of 67 percent by number of the total particles in the 5-9μ diameter range* and was selected with the approval of NASA-Lewis technical representatives. Eight compacts were pressed hydrostatically at 56,600 psi and subsequently vacuum sintered at $1800^{\circ}C$ for 10 minutes and at $2000^{\circ}C$ for 60 minutes.

3.2 Infiltration and Wetability Testing

Infiltration of the porous sintered compacts was accomplished

---

* Complete size distribution given in Table 2-II.

by immersing them individually in the various molten infiltrant baths. First, a prealloyed infiltrant ingot was melted under hydrogen in a quartz boat, placed within a resistor-wound quartz tube. The tungsten compacts then were preheated for 10 minutes, adjacent to the bath, to minimize surface oxides prior to immersion. Bath temperature and time were held constant at $1175^{O}C$ and 30 minutes during the six immersions performed. After removal of the samples, the six infiltrant baths were held at $1175^{O}C$ for an additional period, such that total time in the molten state totaled 60 minutes. This was done in order that subsequent analyses of additive concentrations would be significant indications of infiltrant compositional stability.

In conjunction with immersion of compacts, a technique for rating the wetting of tungsten by the various infiltrants was used. Each compact was cradled in a frame of sheet tungsten throughout the preheating, immersion and cooling periods. This test arrangement is shown in Fig. 3-1. The extent to which the various infiltrants coated the tungsten, and the completeness of coverage, are shown in Fig. 3-2. The extent of wetting or alloying appeared to decrease in the order Cu-B, Cu-Fe, Cu-Be, Ag, Cu-Te, and Cu-P. The Cu-B alloyed extensively with the tungsten, such as to effect disintegration of the frame. Cu-Fe coated the tungsten surface with a thin continuous layer. The Cu-Be alloy provided a relatively thick continuous coating, the surface of which was oxidized. (This oxide is believed to be BeO, formed by reduction of H_2O vapor* by Be. This same oxide was observed as a dross on the surface of the Cu-Be bath.) The pure silver bath wetted the tungsten discontinuously, as did the Cu-Te to a lesser extent. Wetting by Cu-P was nil. From these tests, it is concluded that Cu-Fe has the most favorable wetting characteristic, followed by Cu-Be.

---

* Water vapor in H_2 atmosphere, originating from burning H_2 at furnace tube exit.
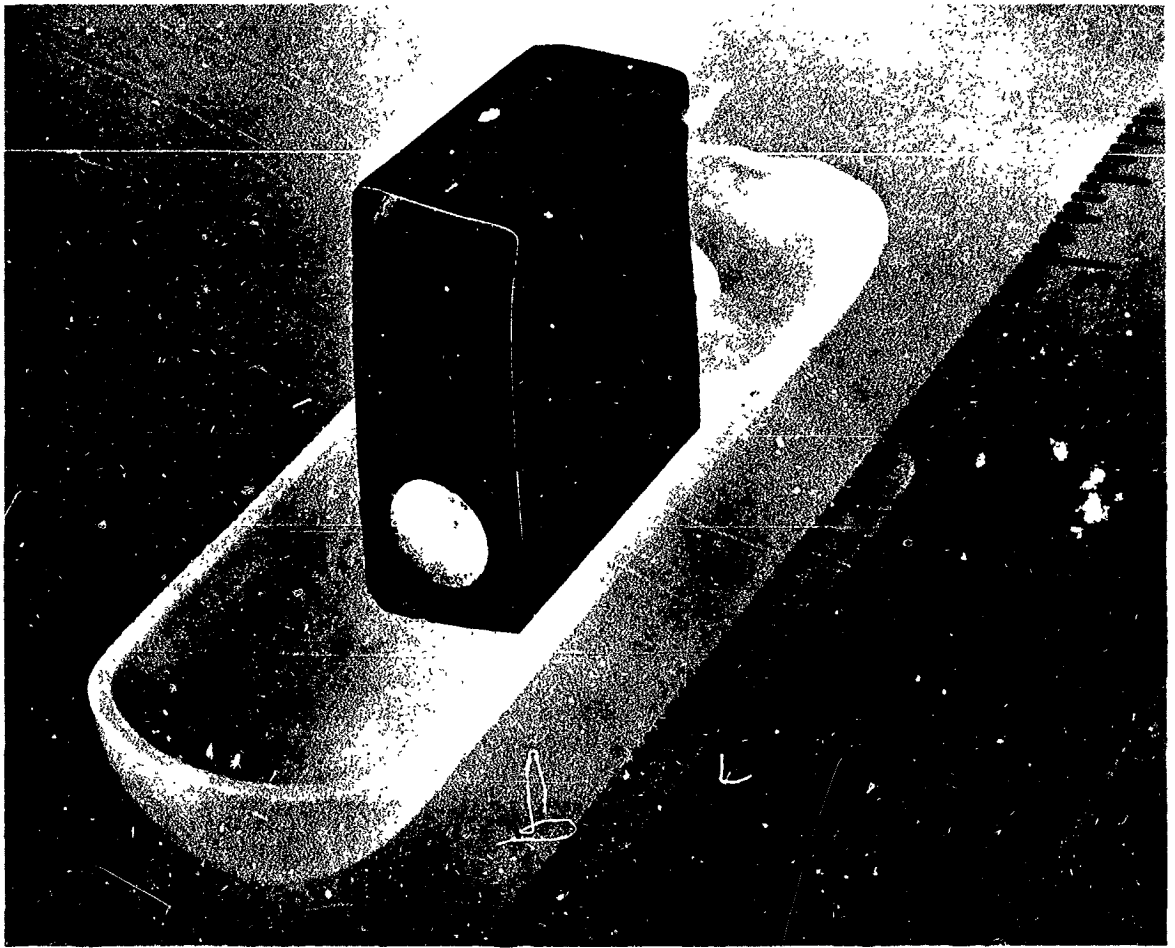
FIG. 3-1   ARRANGEMENT OF SINTERED TUNGSTEN COMPACT WITHIN TUNGSTEN
           FRAME AND QUARTZ BOAT

BEFORE IMMERSION

Cu-B

Cu-Fe

Cu-Be

Ag

Cu-Te

Cu-P
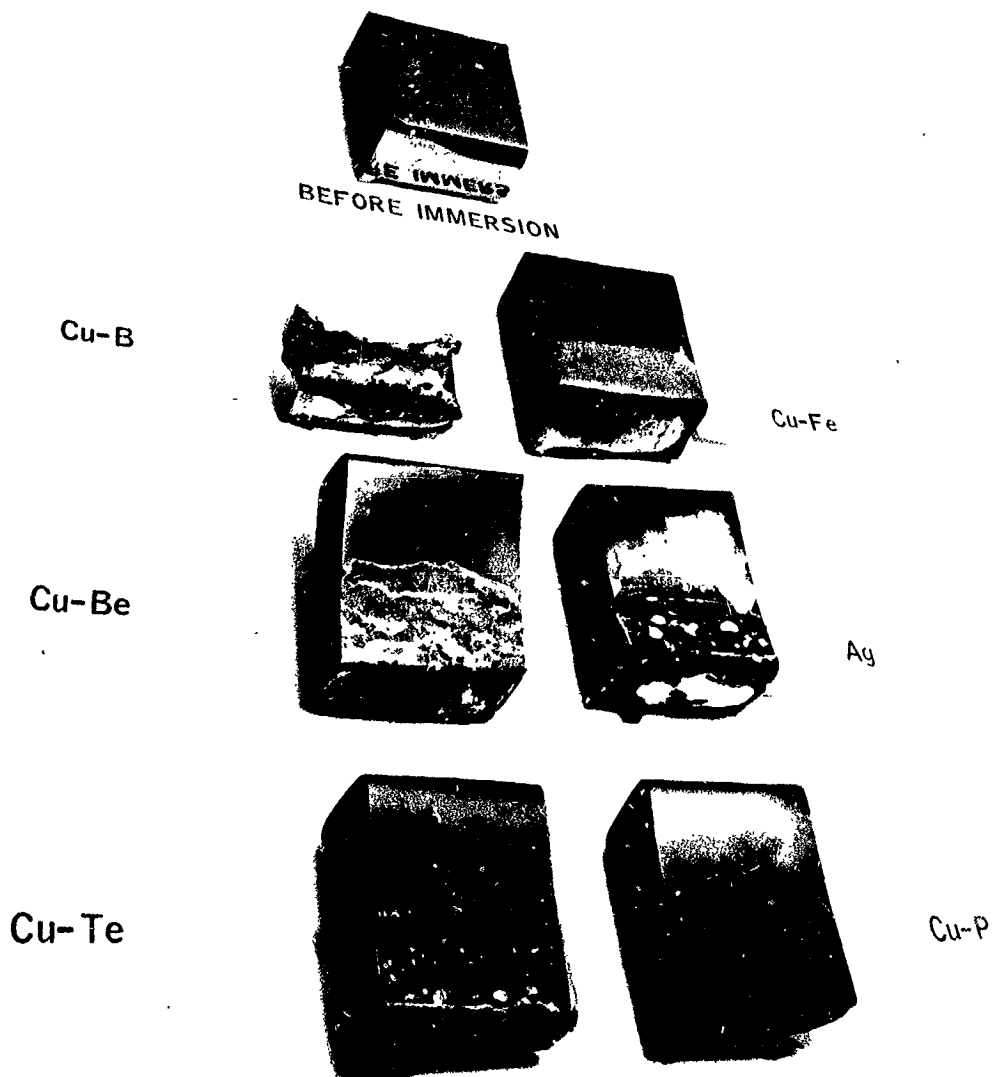
FIG. 3-2 WETTING OF TUNGSTEN SHEET BY VARIOUS INFILTRANTS

3.3 Compositional Stability of Infiltrant Baths

The compositional stability of an infiltrant bath in service is pertinent to its continued effectiveness and to the quality control of the ionizers infiltrated. Therefore, determinations of infiltrant losses were included in this investigation. Chemical analyses of the various baths, after immersion of the tungsten compacts and being held molten at $1175^{\circ}C$ for a total of 60 minutes, are listed in the following tabulation:

Binary Additive to Cu Base	Initial Composition Atom %	Wt. %	Final Composition* Atom %	Wt. %	Loss, % of Initial Additive	Analytical Method
B	2.0	0.346	1.91	0.33	4.5	Spectrographic
Be	2.0	0.289	1.52	0.22	24.0	Spectrographic
Fe	2.0	1.762	1.99+	1.76	< 0.5	Wet
P	2.0	0.986	1.98	0.975	1.0	Wet
Te	2.0	3.937	1.93	3.81	3.5	Wet

* All baths contained a trace of dissolved tungsten, defined as <0.1 wt.

Loss of beryllium was highest at 24 percent of the amount added, followed by boron, tellurium, phosphorus and iron, in decreasing order. The relatively large loss of beryllium is believed to have resulted from the $Be + H_2O = BeO + H_2$ reaction, the low-density BeO reaction product rising to the bath surface and being removed when the surface of the analytical sample was cleaned. The results tabulated above indicate that the Cu-Fe infiltrant was the most stable in the moist hydrogen atmosphere, followed by Cu-P, Cu-Te, Cu-B, and Cu-Be, in order of decreasing compositional stability.

3.4 Machinability of Infiltrants and Infiltrated Compacts

Machinability of the infiltrant alloys per se, and of the infiltrated tungsten compacts, was determined. All information pertinent to the machinability testing is given in Fig. 3-3. Information on chip toughness, breakage and length, plus ratings of machinability by the machinist, are given in Table 3-I. These ratings, while necessarily
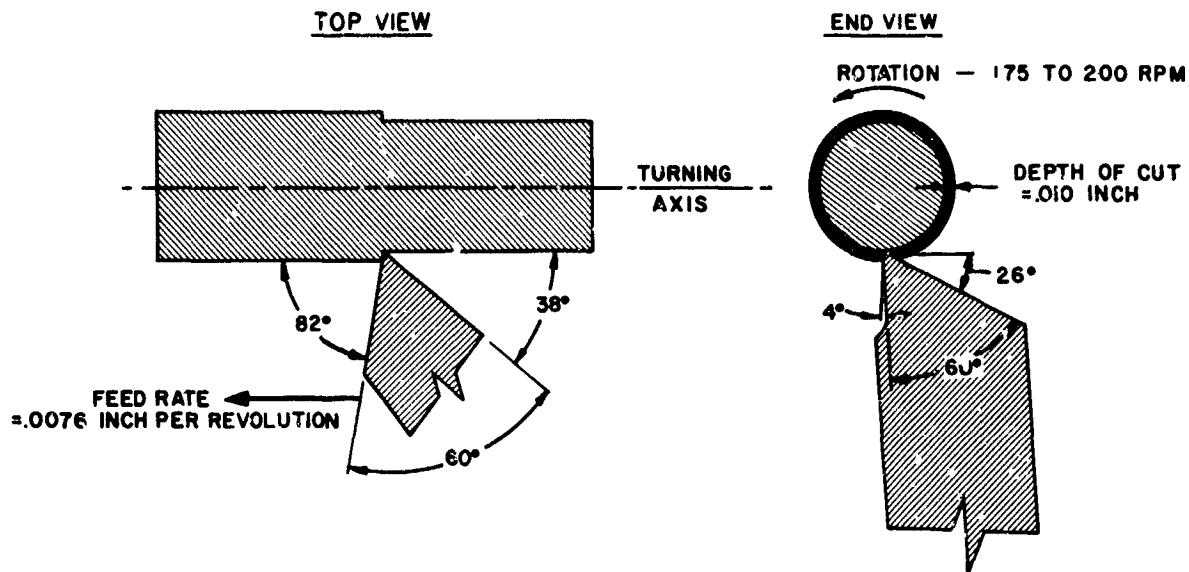
FIG. 3-3   TOOL SETTING AND CLEARANCES USED IN MACHINABILITY TESTS; HIGH-SPEED STEEL TOOL, BESLY MOMAX-COBA H, STYLE 956

TABLE 3-I COMPARISON OF MACHINING CHARACTERISTICS OF VARIOUS INFILTRANT COMPOSITIONS.

Infiltrant Composition	Tests on Infiltrant per Se			Tests on Infiltrated Tungsten		
	Chip Rating(a)		Chip Length	Chip Rating		Machinist's Preference Rating (b)
	Tough-ness	Break-age		Tough-ness	Break-age	
Silver	2	2	short	2	2	5
Cu-Fe	4	4	medium	4	4	2
Cu-Be	5	3	medium	5	5	1
Cu-Te	1	1	very short	1	1	3
Cu-P	3	5	long (tight curl)	3	3	4
Cu-B	6	6	very long (quite straight)	6	6	6

(a) Chip Rating - #1 rating indicates least tough, best-breaking chip

(b) Machinist's Preference - #1 rating indicates most favorable over-all machining characteristic.

relative in nature, are based on extensive machining experience on experimental materials. Machinability of compacts infiltrated with Cu-Be, Cu-Fe, Cu-Te, Cu-P, and Ag differed only slightly, all being very satisfactory and causing no detectable tool wear. However, machining of the compact infiltrated with Cu-B proved to be impossible with the high-speed-steel lathe tool. Using a tungsten carbide tool, it was machined with great difficulty and with appreciable wearing of the tool. The hardness of this compact is believed to have resulted from reaction of the tungsten with boron, to form hard tungsten borides.

3.5 Microstructures of Infiltrated Compacts

The variously infiltrated compacts were machined to test buttons (3/16-inch diameter x 0.04-inches thick) for metallographic examination of pore structures. Typical structures are shown in Fig. 3-4. Based on examination of pertinent features (such as width of tungsten diffusion bridges, frequency of occluded voids, tungsten particle size, and degree of tungsten agglomeration) any effects of various infiltrants on the structures do not differ significantly. Some difference in shade of the infiltrants is apparent, as effected by slight differences in their etching character. Further, some localized differences in density are probable. However, these are believed related to the fabrication of the samples, rather than to infiltration effects. All of the structures of Fig. 3-4 are about 75 percent the theoretical density of tungsten, as subsequent density measurements showed. Ionizers fabricated and tested subsequently in the program were about 80 percent dense and, therefore, had much smaller pores.

3.6 Density and Permeability of Infiltrated Compacts after Vacuum Distillation

Several machined buttons from each of the infiltrated compacts were vacuum distilled at $1500^{\circ}C$ for 15 minutes and finally at $1800^{\circ}C$ for 45 minutes (at a pressure down to 1×10^{-5} torr) to remove the infiltrants. Permeability and density data were then determined. These are listed in Table 3-II. It is immediately apparent that the

Neg.1069   Ag   Neg.1070   Cu-B   Neg.1071   Cu-Be

Neg.1072   Cu-Fe   Neg.1067   Cu-P   Neg.1068   Cu-Te
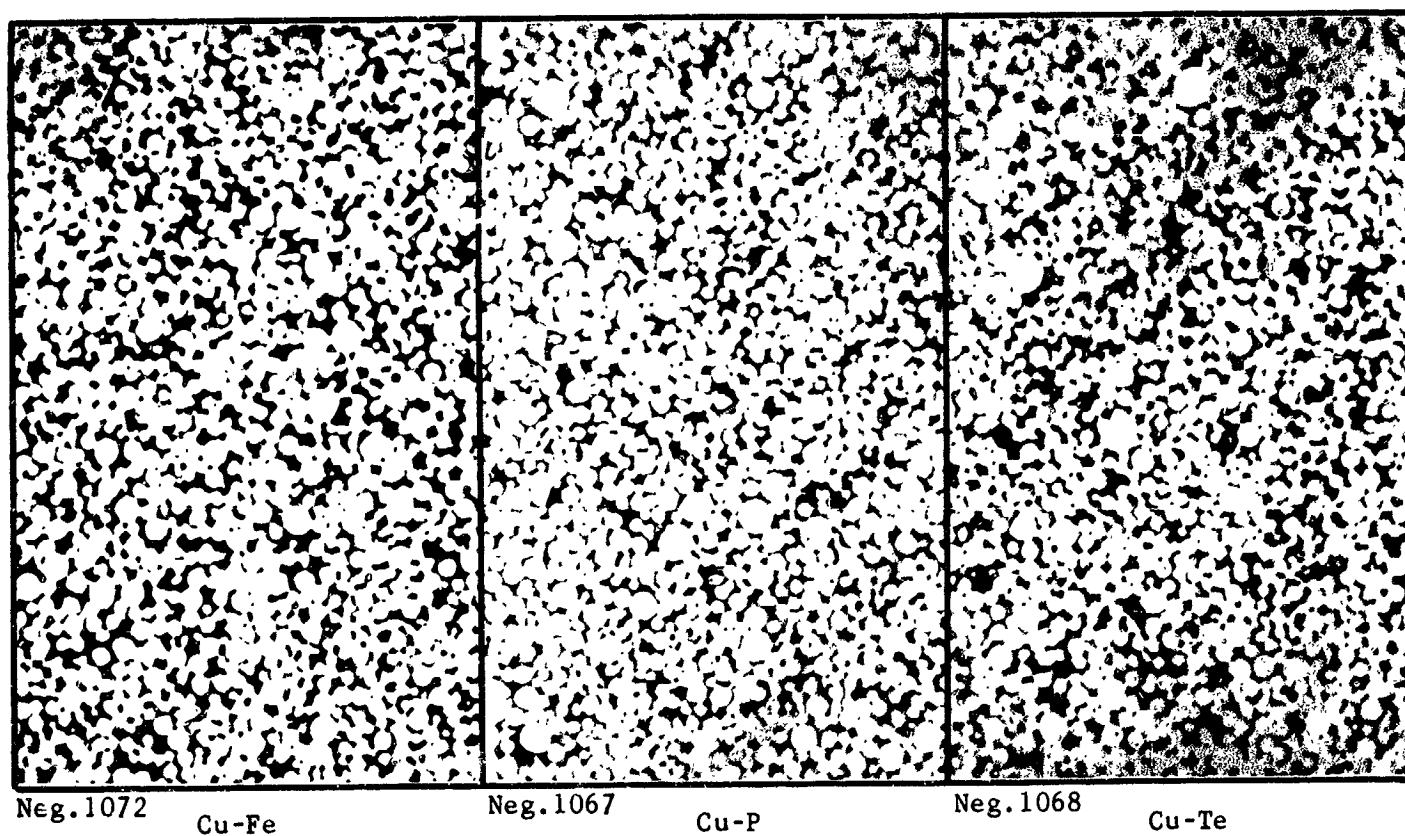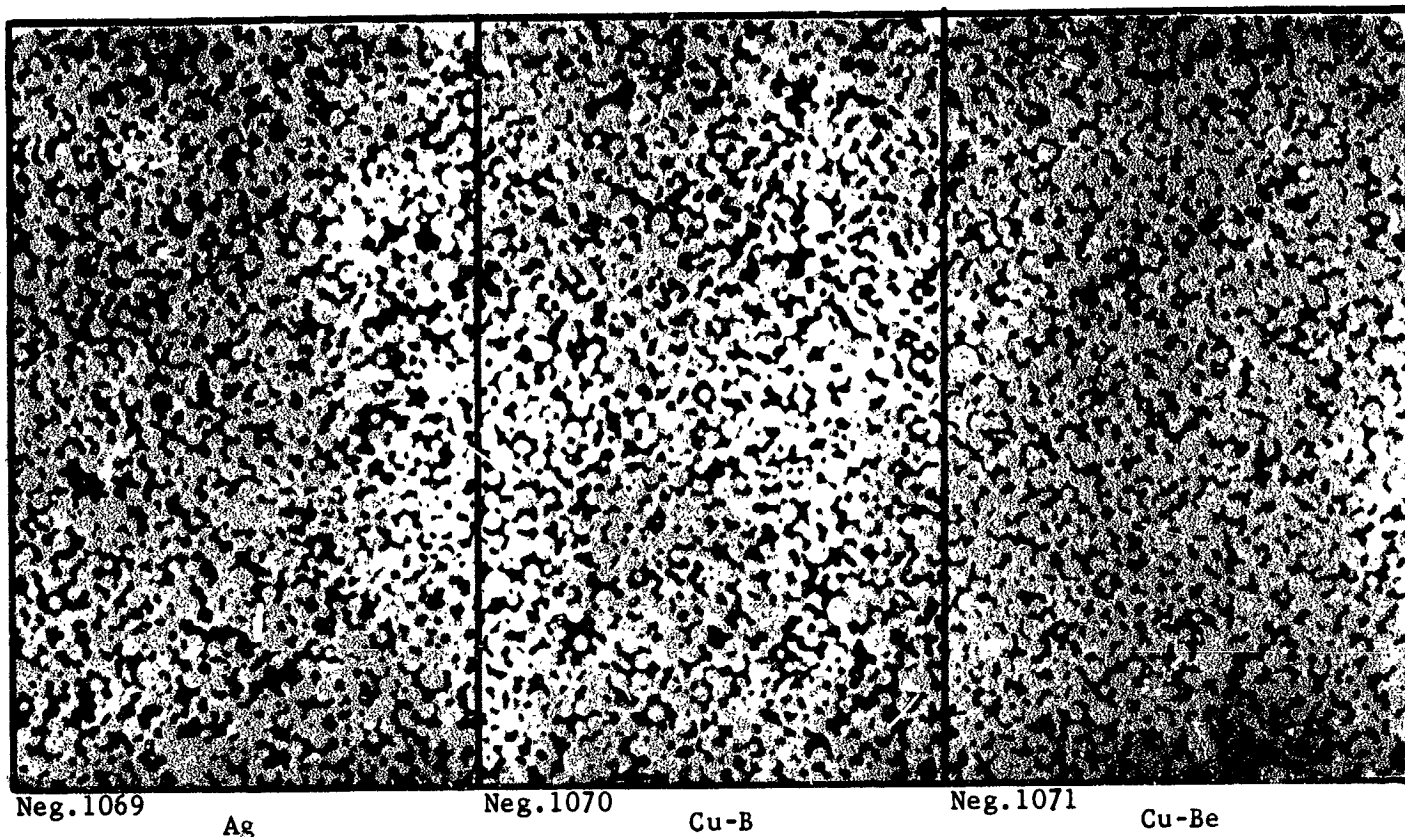
FIG. 3-4 COMPARISON OF MICROSTRUCTURES (At 300X Mag.) OF SPHERICAL TUNGSTEN

Table 3-II

DENSITY AND PERMEABILITY DATA FOR VARIOUSLY INFILTRATED TUNGSTEN BUTTONS, AFTER REMOVAL OF INFILTRANTS BY VACUUM DISTILLATION

Infiltrant	Button No.	Density, % of Theoretical	Mass Permeability Coefficient,* $g \cdot cm^{-1} \cdot sec^{-1} \cdot torr^{-1}$	Transmission Coefficient,** dimensionless
Silver	1	75.03	1.56×10^{-6}	
	2	75.39	1.51	
	3	75.28	1.55	
	4	75.13	1.58	
	Avg.	75.21	1.55×10^{-6}	1.97×10^{-4}
Cu-B	1	74.82	1.64×10^{-6}	
	2	75.28	1.62	
	3	74.82	1.65	
	4	75.13	1.69	
	5	75.34	1.65	
	Avg.	75.08	1.65×10^{-6}	2.08×10^{-4}
Cu-Be	1	74.92	1.62×10^{-6}	
	2	74.97	1.67	
	3	74.82	1.58	
	4	75.34	1.57	
	5	75.23	1.63	
	Avg.	75.06	1.61×10^{-6}	2.05×10^{-4}
Cu-Fe	1	75.08	1.56×10^{-6}	
	2	75.34	1.54	
	3	74.97	1.62	
	4	75.03	1.61	
	5	75.44	1.65	
	Avg.	75.17	1.60×10^{-6}	2.05×10^{-4}
Cu-P	1	74.30	1.66×10^{-6}	
	2	75.44	1.89	
	3	75.23	1.86	
	4	74.82	1.71	
	5	75.03	1.57	
	Avg.	74.96	1.74×10^{-6}	2.21×10^{-4}
Cu-Te	1	75.60	1.49×10^{-6}	
	2	75.65	1.52	
	3	75.13	1.59	
	4	74.77	1.60	
	5	74.25	1.67	
	Avg.	75.08	1.57×10^{-6}	2.12×10^{-4}

*Based on N_2 at 298°K

**Transmission Coef. $= \dfrac{(18.973)(\text{Perm. Coef.})}{(\text{Sample thickness, cm})}$

(Derived subsequently in report)

average values of density, mass permeability coefficient and trans-
mission coefficient are very similar. There does not appear to be
sufficient variation in these values to indicate varied interactions
with the different infiltrants. This conclusion agrees with that of
the metallographic evaluation, previously discussed.

3.7 Residual Infiltrant Elements in Compacts After Vacuum Distillation

As a final step in the infiltration study, residual elements
(remaining in the buttons after distillation) were determined by quan-
titative spectroscopy. Results obtained are as follows:

Buttons infiltrated with Ag	<10 ppm Ag*
Buttons infiltrated with Cu-B	< 1 ppm B, <3 ppm Cu
Buttons infiltrated with Cu-Be	< 1 ppm Be*, < 3 ppm Cu
Buttons infiltrated with Cu-Fe	<10 ppm Fe*, <3 ppm Cu
Buttons infiltrated with Cu-P	50 ppm P (wet analysis), <3 ppm Cu
Buttons infiltrated with Cu-Te	<500 ppm Te*, <3 ppm Cu

---

* Indicates lowest limit of detection with standards available.

The foregoing results indicate very efficient removal of Cu, Ag, B,
Be, and Fe. Since phosphorus has a relatively high vapor pressure,
and since one would expect it to be very readily removed by distilla-
tion, the 50 ppm phosphorus residual value seems too high. The
residual tellurium value is probably much lower than the 500 ppm
minimum detection limit of the comparator standards used.

3.8 Conclusions of Infiltration Study

Results of this study are summarized briefly in the following
tabulation:

Characteristic Evaluated	Best Infiltrant Compositions
Wetting of Tungsten	Cu-Fe, Cu-Be
Infiltrant Compositional Stability	Ag, Cu-Fe
Machinability of Infiltrated Tungsten	Cu-Be, Cu-Fe
Effect of Porous Tungsten Structure	(No significant differences)
Effect on Final Density and Permeability	(No significant differences)
Least Residual Elements in Tungsten after Vacuum Distillation	Ag, Cu-B, Cu-Be, Cu-Fe

In general, results of this investigation indicate that the Cu-2 A/o Fe infiltrant is at least as favorable as the other compositions, such that use of another could not be justified.

4. FABRICATION AND PORE CHARACTERIZATION OF SINTERED SPHERICAL
   TUNGSTEN POWDER

Using three classified fractions of tungsten microspheres, compacts
were pressed, sintered, infiltrated with Cu-2 A/o Fe, machined to button
form, and vacuum distilled. The porous structures resulting were evalu-
ated by means described subsequently in this section. Prerequisites of
this research phase were (1) preparation and analysis of various powder
size fractions (Section 2) and (2) investigation of infiltrant alloys
(Section 3). Having completed (1) and (2), the fabrication of ionizers
from three selected powder fractions to a target density of 80 percent
theoretical proceeded. Thus, for the first time, a controlled series
of ionizers, of common purity and at three levels of pore size, was
prepared and thoroughly evaluated. Details of fabrication and evalua-
tion are described in the following subsections.

4.1 Hydrostatic Pressing of Powder Compacts

All compacts were pressed hydrostatically under 59,000 psi
in the die assembly shown in Figs. 4-1 and 4-1A. The use of a rubber
mold to apply hydrostatic pressure was adopted because of previous
unsuccessful attempts to compact spherical tungsten in a conventional
steel die. Compacts produced in the latter invariably contained con-
choidal fractures. The reason for such fractures is believed to be as
follows: Upon application of uniaxial ram pressure to the powder,
about 1/4 of the load is transmitted by the powder to the steel die
walls. The walls are deflected outward, elastically, a very small but
significant amount. To the instant of initial pressure decrement, the
pressed powder is under compression from all sides. However, as ram
pressure is decreased, the die walls begin to recover elastically,
exerting a radial compressive force on the powder mass. Thus the com-
pact is subjected simultaneously to decreasing ram pressure and to

FIG. 4-1

DIE ASSEMBLY USED TO COMPACT
TUNGSTEN MICROSPHERES UNDER
HYDROSTATIC PRESSURE
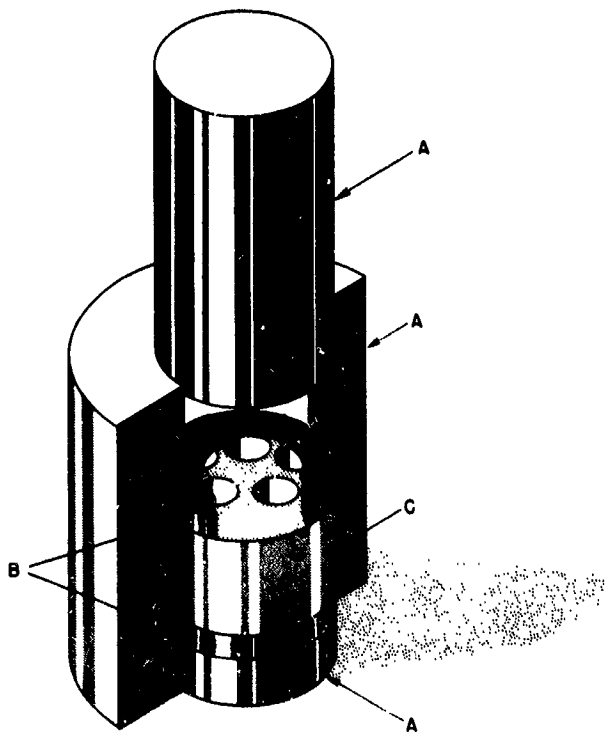
A - STEEL DIE COMPONENTS
B - RUBBER DISCS
C - MULTI-CHAMBERED RUBBER CYLINDER
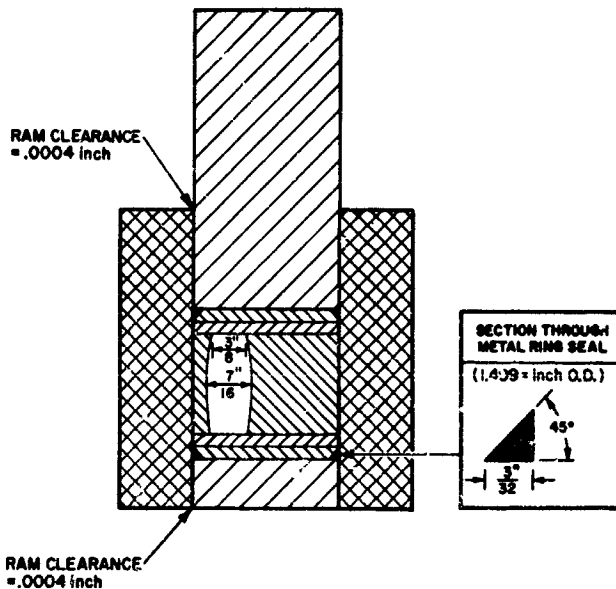
FIG. 4-1A

CROSS SECTION VIEW OF CYLINDRICAL
POWDER-PRESSING DIE SHOWING STEEL RAM,
BASE INSERT, AND FEMALE SECTION, WITH
SILASTIC RUBBER MOLD, NEOPRENE DISCS,
AND LEADED BRONZE PRESSURE SEALS IN
SITU (DRAWING SCALE 1/2 X)

increasing lateral pressure, with the result that shear occurs.

Pressing of tungsten microspheres within the rubber insert fixture of Figs. 4-1 and 4-1A eliminates shear forces since, on decompression, the rubber moves away from the compacts. The barrel shape of the mold cavities is also a very important design feature. Upon decompression, the mold tends to elongate before recovering laterally. Unless the mold vacity is adequately tapered, the compact is subjected to tension and, therefore, can readily be pulled apart.

4.2 Vacuum Sintering of Powder Compacts

Sintering of all compacts was performed at temperatures of 1800-2200°C under 10^{-5} to 10^{-6} torr. The furnace used is shown in Fig. 4-2. It consists of tungsten sheet-resistor elements in a bell-type chamber, with appropriate vacuum pump, electrical accessories and controls. The furnace is equipped with both thermocouple and ion vacuum gauges. Temperature of the work is monitored by optical pyrometer through a sighting window, which is shielded from condensates except during brief periods of temperature determination. The pyrometer is calibrated at regular intervals by sighting on pure metals of known melting point and thus cross-checking on "absolute temperature vs indicated temperature." This method has proven to be much more versatile at the high temperatures than the use of a thermocouple.

4.3 Infiltration of Powder Compacts

The method used to infiltrate sintered tungsten microspheres was the same as that described in Section 3.2. The Cu- 2 A/o Fe infiltrant, described in Section 3.1, was used for all unalloyed tungsten compacts. The Cu-Fe alloy is usually prepared by heating the constituents in Vitrosil boats at 1175°C under hydrogen for 30 minutes. Solution of the iron in the copper, effected under these conditions, is relatively rapid and a homogeneous alloy is obtained.
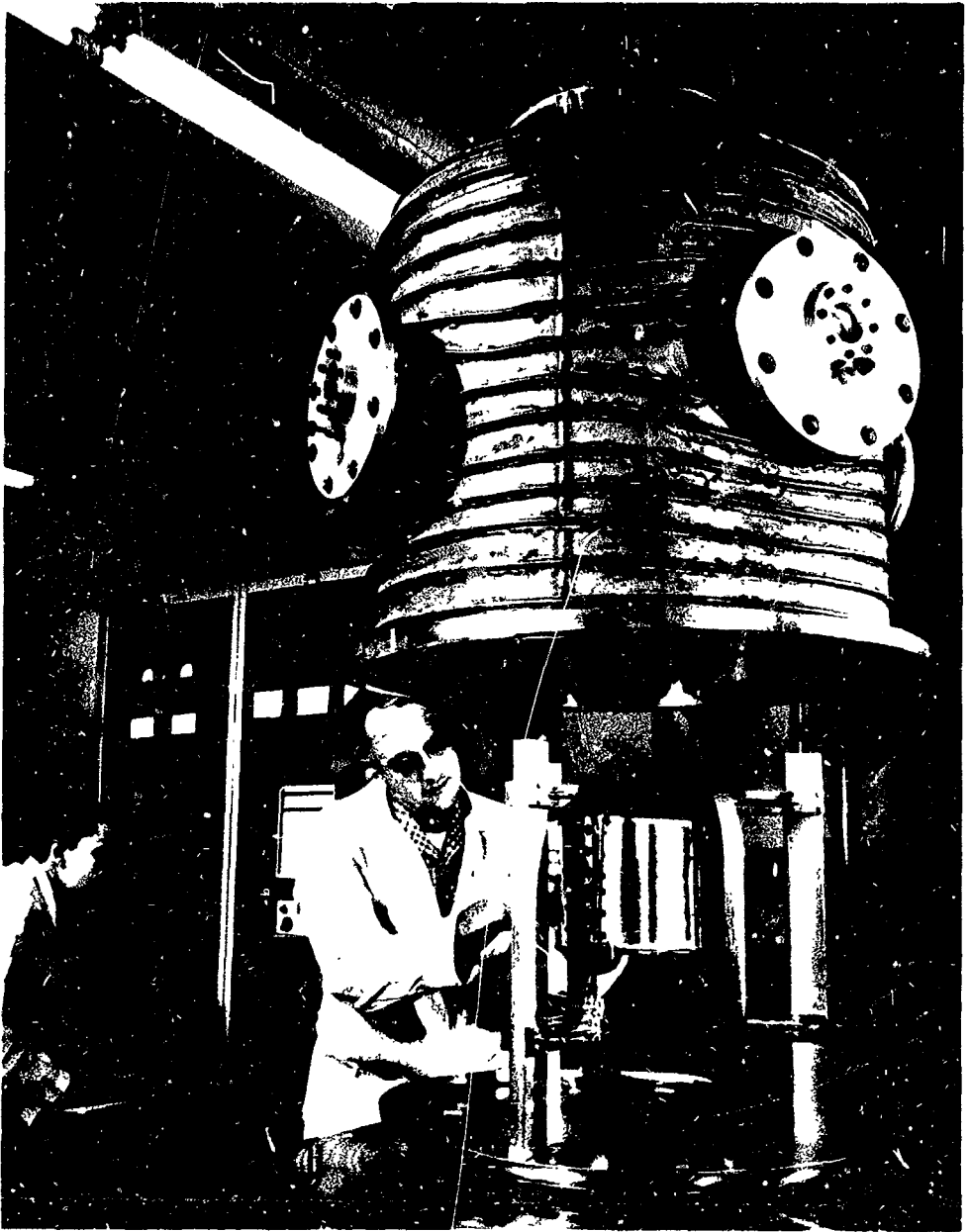
FIG. 4-2   VACUUM SINTERING FURNACE WITH TANTALUM SHEET-RESISTOR
HEATING ELEMENTS

4.4 Machining and Surfacing

In order to determine the effect of surface texture on permeability, ionizer buttons were machined with three different surface finishes: lathe turned, machine ground, and metallographically polished. These surfaces were produced as follows:

The lathe turned finishes on the faces of the ionizer buttons were produced according to the tool set-up shown in Fig. 4-3.

The machine ground faces were produced with a Norton 37C36-KVK grinding wheel (36 grit silicon carbide, K hardness with vitrified bond). Wheel diameter was 5.82 inch so that, at 3450 RPM, linear grinding velocity at the button surfaces was 87.6 ft/sec. This grinding was done wet (water-oil emulsion) in 0.001" increments down to the last two grinding passes, where 0.0005" increments were used.

The metallographic mirror polishes were produced by first grinding in the foregoing manner. The buttons were then mounted in Plexiglas and wet ground on 400- and 600-grit silicon carbide emery paper. Final grinding was done dry on successive 0, 00, 000, and 0000 alumina papers. Polishing was done using a Nylon cloth, with Linde A, and finally, Linde B alumina suspensions in water. After removal of the buttons from the Plexiglas, they were reversed, remounted, and the same polishing procedure was used on the opposite faces. Final polishing was implemented by microscopic examination to ascertain that the copper-filled pores were fully exposed. This precaution is important, since tungsten has a marked tendency to smear over the pores, covering them with a thin layer of distorted metal.

Using a Profilometer device*, an attempt was made to determine quantitatively the surface contours of the surfaced, infiltrated buttons. This was not successful because of (a) marring of the surfaces by the diamond stylus of the device, (b) the very short reciprocating stroke

---

*Profilometer made by the Micrometrical Mfg. Co. of Ann Arbor, Michigan.
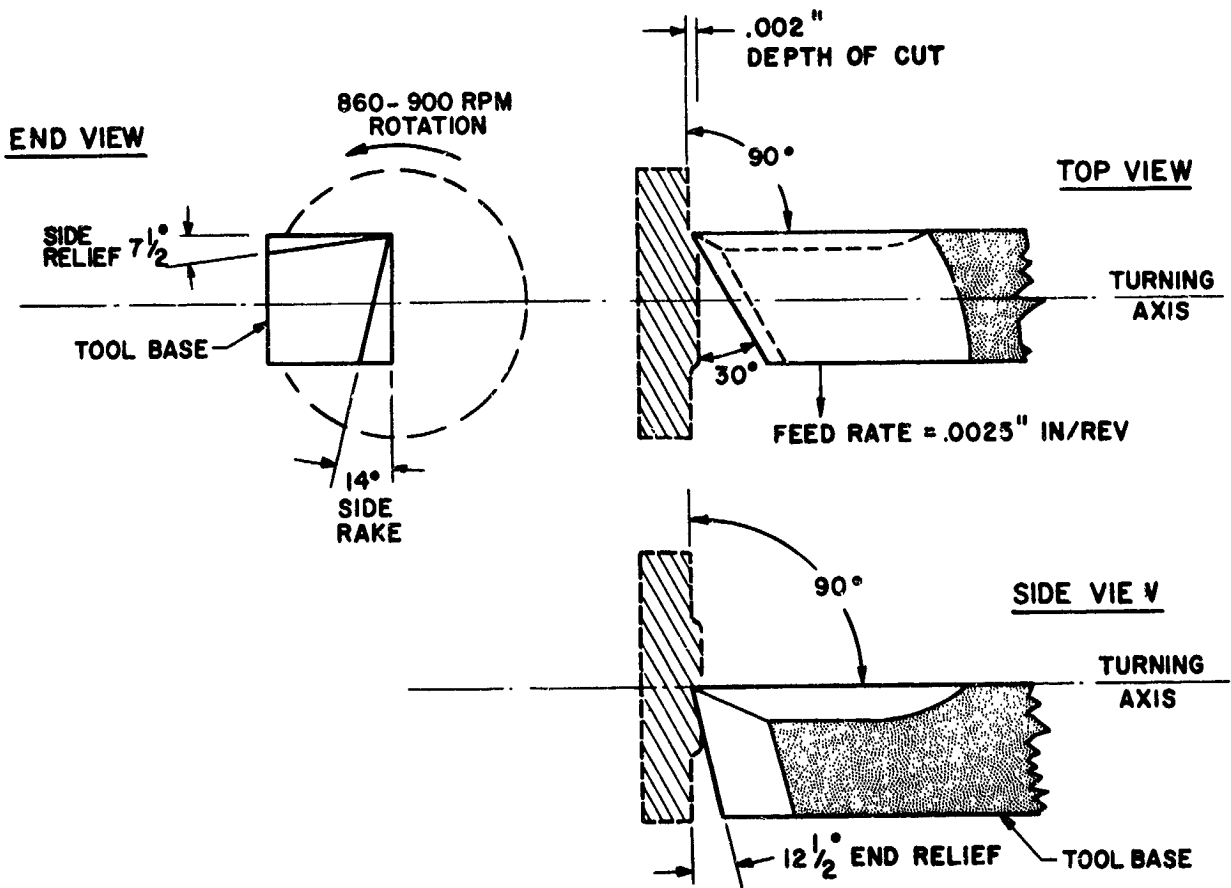
FIG. 4-3 LATHE TOOL CONFIGURATION AND ORIENTATION WITH RESPECT TO FACE OF
IONIZER BUTTONS (HIGH-SPEED STEEL VASCO HYPERCUT TOOL)

necessitated on the 3/16"-diameter faces, and (c) lack of a proper fixture to hold the small buttons immobile during testing. It was decided, therefore, to determine the average contours of surfaces produced by identical machining procedures on high-carbon drill-rod steel. While the inherent machinabilities of the ionizer buttons and the steel are not the same, the material substitution does provide a reasonable approximation. The replicated steel samples had average peak-to-valley contours of:

60 RMS (microinches) for the lathe-turned surface,

6-1/2 RMS (microinches) for the machine-ground surface,

<1 RMS (microinch) for the metallographically-polished surface.

A second replicated turned surface on 347 stainless steel was found to have a 55 RMS finish. Since an austenitic stainless steel and high-carbon tool steel are known to have different machinabilities, it is thus indicated that machining procedure, rather than machinability, is the major factor influencing the surface finish produced.

After distillation of the infiltrant, typical buttons were photographed. Buttons with 3 different surfaces are shown in Fig. 4-4. The white lines across the buttons were caused by contact with tungsten wires, used as spacers during distillation.

The effect of the various surface-finishing operations on permeability coefficient will be discussed in Section 4.8.2.

4.5 Preparation of Comparison Ionizers from H_2-Reduced Porous Tungsten

It was considered technically sound to obtain a complete pore characterization of a commercial porous tungsten and to include it as a comparison material in the ionization performance testing. Therefore, a bar of sintered (infiltrated) H_2-reduced tungsten was purchased from the Philips Metalonics Corporation of Mt. Vernon, New York. The Mod. B grade obtained was reported* to be made from the finest H_2-reduced powder fabricated currently to large porous pieces by Philips. Several

---

* Private communication with R. M. Klein, Sales Mgr., Philips Metalonics.
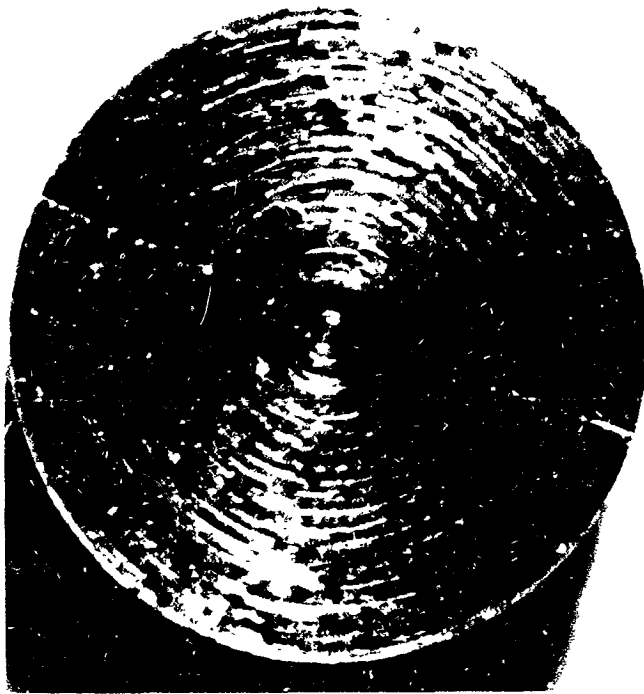
Neg. 106388   Ionizer E6-T-1

Lathe Turned
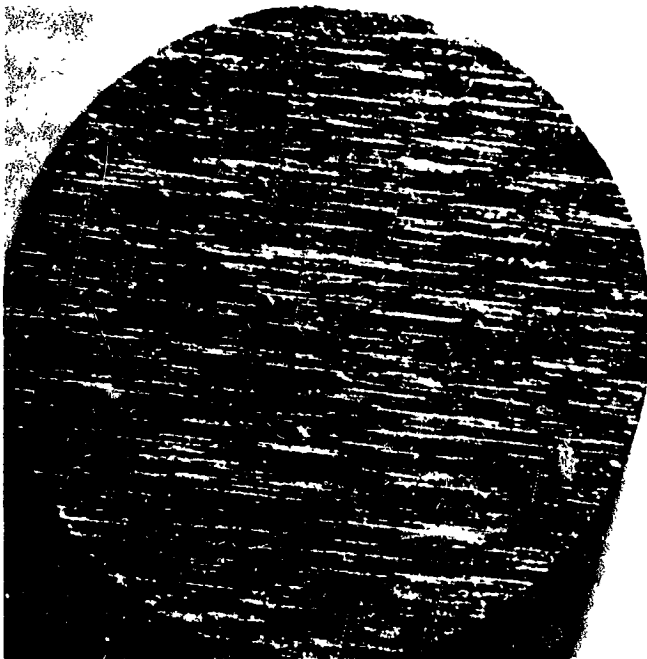
Neg. 116350   Ionizer E6-G-8   Neg. 116349   Ionizer E6-P-3

Surface Ground   Metallographically Polished

FIG. 4-4 APPEARANCE OF IONIZER BUTTONS WITH THREE DIFFERENT SURFACE FINISHES
          (Mag. = 18X)

ionizer buttons were prepared with a surface ground finish, following the same procedure given in Section 4.4. A cylindrical Porosimeter sample was also machined.

4.6 Vacuum Distillation of Infiltrant from Ionizers

Removal of the Cu-2 A/o Fe infiltrant from porous ionizers is usually effected at temperatures of $1800-2000^\circ C$ and at pressures down to 1×10^{-5} torr. For work under this contract, a final distillation temperature $50^\circ C$ below the $1800^\circ C$ sintering temperature of the finest powder buttons (E3, $1-4\mu$) was selected. The distillation conditions were held constant for all buttons and porosimeter samples fabricated, including the Philips Mod. B samples. Thus the probability of additional sintering, shrinkage, and structural change during distillation was minimized. However, the lowering of distillation temperature also introduced the factor of less thorough removal of (infiltrant) iron, as discussed in the subsequent subsection.

For vacuum distillation, the ionizer buttons were placed on edge in rectangular tungsten boats. The interiors of the boats were coated with MgO to prevent coherence of the buttons to the boats. Tungsten wire stables were used as spacers to separate the buttons. While use of the MgO "parting" film has no apparent detrimental effect on pure tungsten, its use is not recommended in close proximity with W-Ta alloys. This will be discussed further in Section 6.5.

A complete flow sheet of the process, used to fabricate the three size fractions of tungsten microspheres, is shown in Fig. 4-5. This includes data on pressing, sintering, machining, and vacuum distillation, as well as on average final densities achieved.

4.7 Final Purity of Ionizers

Spectrographic analyses of the E3 $(1-4\mu)$, E6 $(3-6\mu)$, E7A $(4-8\mu)$, and Philips Mod. B buttons were obtained after the constant vacuum distillation treatment. In review, this treatment consisted of heating at $1500^\circ C$ for 15 minutes and at $1750^\circ C$ for 45 minutes at 1×10^{-5} torr

E3 POWDER (1-4μ)   E6 POWDER (3-6μ)   E7A POWDER (4-8μ)

PRESS 5 COMPACTS OF EACH AT 59,000 psi, ISOSTATIC

SHAPE 1 COMPACT OF EACH TO RECTANGULAR FORM FOR DENSITY MEASUREMENT

VACUUM SINTER at 5×10^{-5} torr

E3 1800°C for 60 min.   E6 1900°C for 90 min.   E7A 2100°C for 70 min.

INFILTRATE DENSITY SAMPLE AND 4 COMPACTS FROM EACH IN Cu-2Fe AT 1175°C FOR 30min

MACHINE 4 COMPACTS FROM EACH INTO CYLINDERS 3/16" dia. x ~3/4" long

1 SAMPLE FOR DENSITY MEASUREMENT   3 CYLINDERS FOR IONIZER BUTTONS   1 CYLINDER FOR PORE SPECTRAL ANALYSIS

9 BUTTONS WITH LATHE TURNED SURFACE   11-12 BUTTONS WITH MACHINE GROUND SURFACE   11-12 BUTTONS WITH POLISHED SURFACE

VACUUM DISTILL INFILTRANT AT 1500°C -15min + 1750°C -45min

E3	DENSITY
TARGET	80.00 %
28 BUTTONS AVERAGE	80.71 %
POROSIMETER SAMPLE	79.63 %

E6	DENSITY
TARGET	80.00 %
30 BUTTONS AVERAGE	80.51 %
POROSIMETER SAMPLE	80.31 %

E7A	DENSITY
TARGET	80.00 %
29 BUTTONS AVERAGE	80.66 %
POROSIMETER SAMPLE	80.73 %

FIG. 4-5   FABRICATION PROCEDURES FOR IONIZER BUTTONS FROM 3 FRACTIONS OF SPHERICAL TUNGSTEN POWDER, BUTTONS FROM EACH HAVING 3 SURFACE FINISHES

ambient pressure. Results of the analyses are given on page A9, Appendix, in a certified spectrographic report of the Materials Testing Laboratories. These results indicate no differences in impurity levels to the lower detection limits, other than in the residual iron contents. The latter are surprisingly high in view of values previously obtained with final distillation at 1800°C, as follows:

	Powder Lot-Size Fraction	Buttons Distilled at, °C/min	Residual Iron, ppm
Previous	C-unclassified	1500/30 and 2000/15	10
	D-Frac. 8	1500/15 and 1800/45	10
Recent	E-Frac. 3	1500/15 and 1750/45	170
	E-Frac. 6	1500/15 and 1750/45	165
	E-Frac. 7A	1500/15 and 1750/45	94
	Philips Mod. B	1500/15 and 1750/45	290

* Sample density = ∼75 percent.
For all other samples, density = ∼80 percent.

The foregoing values would indicate a much greater efficiency of iron removal at 1800 than at 1750°C. While this is possible, it does not seem probable. Therefore, the spectral line densities obtained for these samples have been rechecked. Since no interpretational errors were found, additional samples will be submitted for checking in the follow-on contract. Should these higher iron contents, detected after final distillation at 1750°C, be verified subsequently, the conclusion that residual iron is not as detrimental to ionization performance as initially feared would be indicated.

4.8 Pore Characterization of Ionizers

4.8.1 Density

In order to determine the conditions necessary to sinter the three different fractions of spherical powder to 80 percent target density, preliminary samples were first pressed under 59000 psi, hydrostatic pressure. These samples were shaped to rectangular form, measured, weighed, and their as-pressed densities were determined. They were then sintered under 5×10^{-5} torr pressure in 30, 30, and

60-minute increments, such that a cumulative sintering-time series of 0, 30, 60, and 120 minutes was obtained.

"Density vs sintering time" curves obtained are plotted in Fig. 4-6 (for 1800°C) and Fig. 4-7 (for 2000°C). The trends shown are in agreement with theoretical expectations, i.e., a continuous increase in density with sintering time for all samples, more rapid sintering of the finer powder fractions than of the coarser fractions at both temperatures, and more rapid sintering of all samples at 2000°C than at 1800°C. In order to intercept the 80 percent density level, an additional sample of powder fraction E7A was sintered at 2200°C and the curve obtained is included in Fig. 4-7. Curves showing the sintering rates of the unclassified base Lot E powder are also drawn in these figures.

Based on interpolation of the curves of Figs. 4-6 and 4-7, and on the final vacuum distillation treatment used, sintering conditions were selected to yield the densities estimated below. Actual final (avg.) densities of buttons produced subsequently are listed also.

Powder Fraction	Temp., °C	Sintering Time, min.	Estimated Sintered Density, percent of theoretical	Estimated Density after Vacuum Distillation of Infiltrant*	Actual Density after Vacuum Distillation (29 Button Avgs.)
E3 (1-4μ)	1800	60	75.3	79	80.7
E6 (3-6μ)	1900	90	77.8	79.3	80.5
E7A(4-8μ)	2100	70	78.6	79.6	80.7

* Distillation at 1500°C for 15 min., plus 1750°C for 45 min.
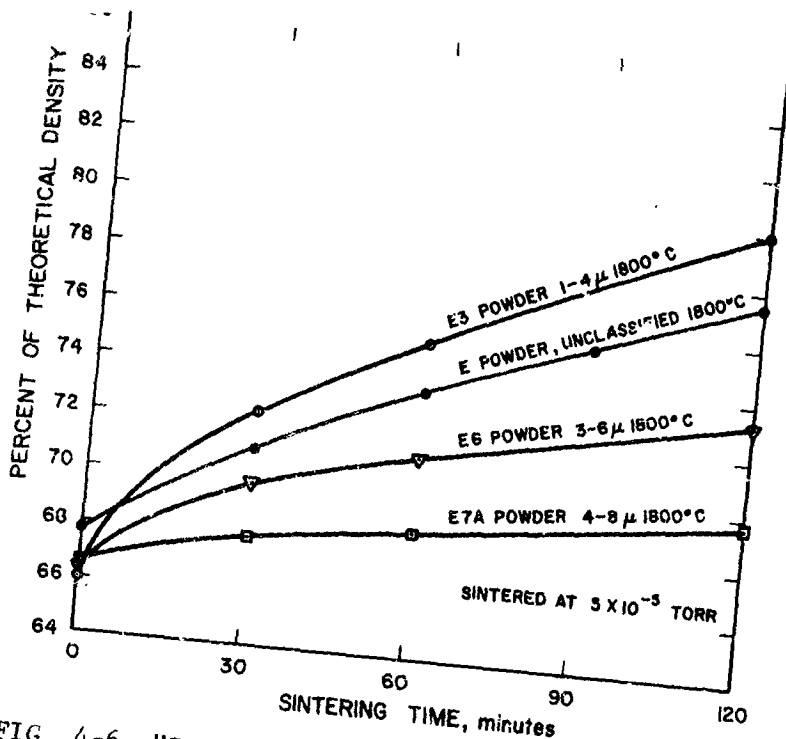
FIG. 4-6 "DENSITY VS SINTERING TIME" CURVES
FOR THREE SIZE FRACTIONS OF LOT E
SPHERICAL TUNGSTEN POWDER (Rectangular compacts of ~4 cm³ volume, pressed isostatically at 59,000 psi)
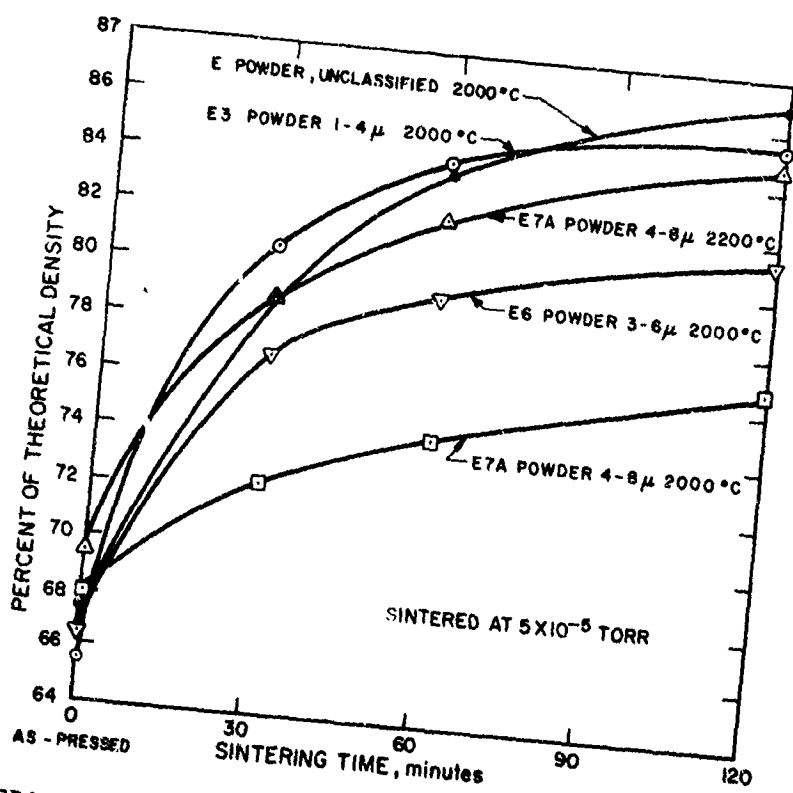
FIG. 4-7 "DENSITY VS SINTERING TIME" CURVES
FOR THREE SIZE FRACTIONS OF LOT E
SPHERICAL TUNGSTEN POWDER (Rectangular compacts of ~4 cm³ volume, pressed isostatically at 59,000 psi)

Final density data on all buttons prepared from the E3, E6, and E7A powders are listed in Tables 4-I, II, and III. Final density data on the Philips Mod. B tungsten are listed in the tabulation below:

Button No.	Density, percent of theoretical
PB-G-1	80.62
PB-G-2	80.57
PB-G-3	80.62
PB-G-4	81.19
PB-G-5	81.30
PB-G-6	81.40
PB-G-7	80.36
Avg.	80.87

As Tables 4-I, II, III, and the above tabulation show, the density of all the ionizer buttons used in this research were held as close as was technically feasible to the target density of 80 percent.

4.8.2 Mass Permeability Coefficient

Determination of the permeability of porous bodies, with respect to a diffusing gas or vapor, is a reliable and simple means of determining fluid-transmitting efficiency. Permeability coefficients, in contrast to density values, are extremely sensitive to subtle changes in pore structure. For these reasons, permeability coefficients have been determined on all ionizer buttons produced under the current and previous NASA contracts.

A sketch of the permeability apparatus used at Electro-Optical Systems is included as Fig. 4-8, with the associated electrical circuits shown in Fig. 4-9. A porous sample button (of 3/16" dia. x .04" thick) is clamped in the test fixture within a neoprene "O" ring. Compression exerted by the fixture presses the "O" ring tightly against the cylindrical surface of the button, sealing it so that only the button face area is exposed to the diffusant gas. Other components of

TABLE 4-I

Dimensions, Densities, Permeability and Transmission Coefficients for Ionizers Prepared from E3 (1-4μ) Spherical Tungsten Powder (Designations T, G, and P indicate lathe turned, machine ground, and metallographically polished finishes, respectively)

Ionizer No.	Face Area, cm^2	Thickness, cm	Volume, cm^3	Weight, gm	Density, g/cm^3	% of Max. Theoretical Density	δt, sec.	Mass Permeability Coefficient, $gm \cdot cm^{-1} \cdot sec^{-1} \cdot torr^{-1}$	Transmission Coefficient, dimensionless
E3-T-1	.16914	.10211	.01727	.2681	15.52	80.41	15.00	0.179 x 10^{-6}	3.322 x 10^{-5}
E3-T-2	.16969	.10262	.01741	.2708	15.55	80.57	15.56	0.173 x	3.192 x
E3-T-3	.16934	.10287	.01742	.2722	15.63	80.98	22.57	0.120 x	2.205 x
E3-T-4	.16934	.10160	.01720	.2715	15.78	81.76	22.13	0.120 x	2.249 x
E3-T-5	.16990	.10236	.01739	.2663	15.31	79.33	11.89	0.225 x	4.172 x
E3-T-6	.17005	.10312	.01754	.2680	15.28	79.17	12.46	0.216 x	3.978 x
E3-T-7	.17025	.10312	.01756	.2696	15.35	79.53	13.71	0.196 x	3.611 x
E3-T-8	.16990	.10262	.01744	.2682	15.38	79.69	12.26	0.219 x	4.046 x
E3-T-9	.17005	.10287	.01749	.2678	15.31	79.33	12.75	0.211 x	3.887 x
Average					15.46	80.10		0.184 x 10^{-6}	3.407 x 10^{-5}
E3-G-1	.16914	.09373	.01585	.2456	15.50	80.31	11.11	0.222 x 10^{-6}	4.485 x 10^{-5}
E3-G-2	.16934	.09373	.01587	.2469	15.56	80.62	11.07	0.222 x	4.496 x
E3-G-3	.16893	.09373	.01583	.2458	15.53	80.47	11.38	0.217 x	4.384 x
E3-G-4	.16914	.09347	.01581	.2461	15.57	80.67	12.42	0.198 x	4.012 x
E3-G-5	.16914	.09373	.01585	.2460	15.52	80.41	10.59	0.232 x	4.705 x
E3-G-6	.16914	.09347	.01581	.2463	15.58	80.73	12.86	0.191 x	3.875 x
E3-G-7	.16893	.09296	.01570	.2472	15.75	81.61	19.81	0.123 x	3.347 x
E3-G-8	.16934	.09119	.01544	.2456	15.91	82.44	10.54	0.227 x	4.722 x
E3-G-9	.16934	.09398	.01591	.2503	15.73	81.50	13.72	0.180 x	3.628 x
E3-G-10	.16914	.09347	.01581	.2448	15.48	80.21	10.54	0.253 x	4.728 x
Average					15.61	80.88		0.205 x 10^{-6}	4.238 x 10^{-5}
E3-P-1	.16878	.08992	.01518	.2361	15.55	80.57	11.54	0.205 x 10^{-6}	4.237 x 10^{-5}
E3-P-2	.16990	.09067	.01540	.2385	15.49	80.26	9.57	0.248 x	5.184 x
E3-P-3	.16914	.09042	.01529	.2356	15.41	79.84	10.11	0.235 x	4.929 x
E3-P-4	.16914	.09017	.01525	.2364	15.50	80.31	9.85	0.240 x	5.059 x
E3-P-5	.17005	.08992	.01529	.2462	16.10	83.42	35.62	0.066 x	1.391 x
E3-P-6	.16878	.09067	.01530	.2374	15.52	80.41	10.83	0.220 x	4.611 x
E3-P-7	.16914	.09093	.01538	.2491	16.20	83.94	38.24	0.062 x	1.303 x
E3-P-8	.16878	.09067	.01530	.2408	15.74	81.55	13.25	0.180 x	3.761 x
E3-P-9	.16893	.09042	.01527	.2356	15.43	79.95	9.67	0.246 x	5.159 x
Average					15.66	81.14		0.189 x 10^{-6}	3.969 x 10^{-5}
Overall Avg.						80.71		0.193 x 10^{-6}	3.881 x 10^{-5}

Dimensions, Densities, Permeability and Transmission Coefficients for Ionizers Prepared from
E6 (3-6μ) Spherical Tungsten Powder (Designations T, G and P indicate lathe turned,
machine ground, and metallographically polished finishes, respectively)

Ionizer No.	Face Area, cm^2	Thickness, cm	Volume, cm^3	Weight, gm	Density, g/cm^3	% of Max. Theoretical Density	δt, sec.	Mass Permeability Coefficient, $gm \cdot cm^{-1} \cdot sec^{-1} \cdot torr^{-1}$	Transmission Coefficient, dimensionless
E6-T-1	.17588	.10287	.01809	.2774	15.33	79.43	9.71	0.268×10^{-6}	4.935×10^{-5}
E6-T-2	.17588	.10414	.01832	.2852	15.57	80.67	12.52	$0.210 \times$	$3.820 \times$
E6-T-3	.17623	.10312	.01817	.2779	15.29	79.22	8.75	$0.297 \times$	$5.466 \times$
E6-T-4	.17588	.10262	.01805	.2785	15.43	79.95	10.14	$0.256 \times$	$4.726 \times$
E6-T-5	.17603	.10312	.01815	.2832	15.60	80.83	13.48	$0.193 \times$	$3.552 \times$
E6-T-6	.17588	.10490	.01845	.2818	15.27	79.12	9.63	$0.275 \times$	$4.976 \times$
E6-T-7	.17588	.10414	.01832	.2862	15.62	80.93	14.52	$0.181 \times$	$3.300 \times$
E6-T-8	.17588	.10414	.01832	.2811	15.34	79.48	10.27	$0.256 \times$	$4.666 \times$
Average					15.43	79.75		0.242×10^{-6}	4.430×10^{-5}
E6-G-1	.17532	.09601	.01683	.2594	15.41	79.84	7.95	0.306×10^{-6}	6.048×10^{-5}
E6-G-2	.17512	.09627	.01686	.2664	15.80	81.87	9.96	$0.245 \times$	$4.832 \times$
E6-G-3	.17547	.09652	.01694	.2721	16.06	83.21	16.80	$0.45 \times$	$2.859 \times$
E6-G-4	.17567	.09627	.01691	.2683	15.87	82.23	15.37	$0.158 \times$	$3.121 \times$
E6-G-5	.17567	.09652	.01696	.2615	15.42	79.90	7.93	$0.308 \times$	$6.050 \times$
E6-G-6	.17547	.09627	.01689	.2618	15.50	80.31	8.09	$0.301 \times$	$5.937 \times$
E6-G-7	.17567	.09627	.01691	.2622	15.51	80.36	8.35	$0.292 \times$	$5.746 \times$
E6-G-8	.17588	.09652	.01698	.2629	15.48	80.21	8.32	$0.293 \times$	$5.760 \times$
E6-G-9	.17532	.09677	.01697	.2589	15.26	79.07	7.63	$0.321 \times$	$6.300 \times$
E6-G-10	.17512	.09728	.01704	.2641	15.50	80.31	8.43	$0.293 \times$	$5.709 \times$
E6-G-11	.17588	.09703	.01707	.2631	15.41	79.84	8.13	$0.301 \times$	$5.894 \times$
Average					15.57	80.67		0.269×10^{-6}	5.296×10^{-5}
E6-P-1	.17532	.08966	.01572	.2515	16.00	82.90	15.07	0.151×10^{-6}	3.190×10^{-5}
E6-P-2	.17547	.09195	.01613	.2565	15.90	82.38	16.03	$0.155 \times$	$2.996 \times$
E6-P-3	.17547	.09246	.01622	.2487	15.33	79.43	7.62	$0.307 \times$	$6.303 \times$
E6-P-4	.17491	.09169	.01604	.2478	15.45	80.05	9.87	$0.233 \times$	$4.882 \times$
E6-P-5	.17567	.09220	.01620	.2588	15.98	82.80	17.62	$0.132 \times$	$2.723 \times$
E6-P-6	.17547	.08992	.01578	.2457	15.57	80.67	8.42	$0.270 \times$	$5.704 \times$
E6-P-7	.17512	.09220	.01615	.2465	15.26	79.07	7.27	$0.322 \times$	$6.621 \times$
E6-P-8	.17512	.09246	.01619	.2499	15.44	80.00	7.60	$0.309 \times$	$6.333 \times$
E6-P-9	.17547	.09220	.01618	.2491	15.40	79.79	7.18	$0.325 \times$	$6.689 \times$
E6-P-10	.17512	.09017	.01595	.2468	15.47	80.16	10.89	$0.210 \times$	$4.419 \times$
E6-P-11	.17532	.09144	.01603	.2511	15.66	81.14	9.71	$0.239 \times$	$4.952 \times$
Average					15.59	80.78		0.241×10^{-6}	4.983×10^{-5}
Overall Avg.						80.51		0.252×10^{-6}	4.950×10^{-5}

TABLE 4-III

Dimensions, Densities, Permeability and Transmission Coefficients for Ionizers Prepared from E7A (4-8μ) Spherical Tungsten Powder (Designations T, G and P indicate lathe turned, machine ground, and metallographically polished finishes, respectively)

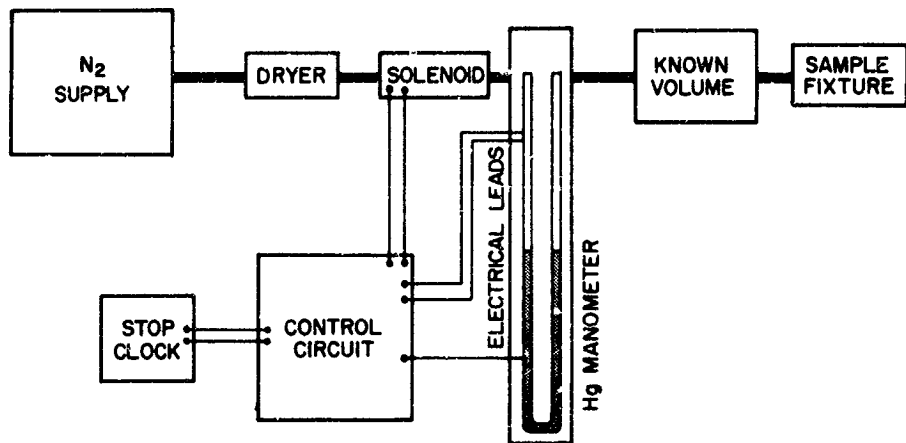| Ionizer No.	Face Area, cm²	Thickness, cm	Volume, cm³	Weight, gm	Density, g/cm³	% of Max. Theoretical Density	St, sec.	Mass Permeability Coefficient, gm·cm⁻¹·sec⁻¹·torr⁻¹	Transmission Coefficient, dimensionless
E7A-T-1	.17795	.10439	.01858	.2846	15.32	79.38	5.65	0.461×10^{-6}	8.383×10^{-5}
E7A-T-2	.17831	.10312	.01839	.2826	15.37	79.64	5.75	0.447	8.220
E7A-T-3	.17775	.10414	.01851	.2875	15.53	80.47	5.80	0.449	6.434
E7A-T-4	.17816	.10262	.01828	.2858	15.63	80.98	6.77	0.378	6.988
E7A-T-5	.17775	.10490	.01865	.2905	15.58	80.73	6.63	0.395	7.151
E7A-T-6	.17816	.10389	.01851	.2877	15.54	80.52	6.94	0.373	6.817
E7A-T-7	.17679	.10465	.01850	.2891	15.63	80.98	6.30	0.417	7.567
E7A-T-8	.17795	.10490	.01867	.2893	15.50	80.31	6.31	0.415	7.506
E7A-T-9	.17816	.10338	.01842	.2826	15.34	79.48	5.84	0.441	8.100
Average					15.49	80.26		0.420×10^{-6}	7.463×10^{-5}
E7A-G-1	.17775	.09677	.01720	.2671	15.53	80.47	4.63	0.522×10^{-6}	10.241×10^{-5}
E7A-G-2	.17740	.09652	.01712	.2651	15.48	80.21	4.83	0.511	9.837
E7A-G-3	.17719	.09576	.01697	.2665	15.70	81.35	5.26	0.456	9.043
E7A-G-4	.17740	.09677	.01717	.2697	15.71	81.40	5.96	0.407	7.971
E7A-G-5	.17775	.09601	.01707	.2685	15.73	81.50	5.80	0.414	8.175
E7A-G-6	.17775	.09601	.01707	.2686	15.74	81.55	5.94	0.404	7.983
E7A-G-7	.17775	.09652	.01716	.2667	15.54	80.52	5.06	0.467	8.371
E7A-G-8	.17740	.09677	.01717	.2664	15.52	80.41	5.00	0.485	9.502
E7A-G-9	.17740	.09601	.01703	.2651	15.57	80.67	4.33	0.555	10.973
E7A-G-10	.17775	.09601	.01707	.2678	15.69	81.30	5.51	0.434	8.605
E7A-G-11	.17775	.09576	.01702	.2669	15.68	81.24	5.34	0.448	8.879
Average					15.63	80.98		0.464×10^{-6}	9.053×10^{-5}
E7A-P-1	.17719	.08865	.01571	.2441	15.54	80.52	4.45	0.499×10^{-6}	10.689×10^{-5}
E7A-P-2	.17740	.08738	.01550	.2443	15.76	81.66	5.92	0.370	8.025
E7A-P-3	.17740	.08865	.01573	.2464	15.66	81.14	5.31	0.418	8.947
E7A-P-4	.17740	.08687	.01541	.2381	15.45	80.05	4.25	0.512	11.178
E7A-P-5	.17740	.08890	.01577	.2443	15.49	80.26	4.27	0.521	11.125
E7A-P-6	.17740	.08839	.01568	.2440	15.56	80.62	4.38	0.505	10.847
E7A-P-7	.17775	.08738	.01553	.2412	15.53	80.47	4.68	0.467	10.131
E7A-P-8	.17719	.08915	.01580	.2452	15.52	80.41	4.80	0.466	9.909
E7A-P-9	.17775	.08941	.01589	.2482	15.61	80.88	5.36	0.417	8.846
Average					15.57	80.67		0.464×10^{-6}	9.966×10^{-5}
Overall Avg.					15.57	80.66		0.450×10^{-6}	8.843×10^{-5}

FIG. 4-8   BLOCK DIAGRAM OF PERMEABILITY APPARATUS

1. CLOCK START SPDT } 1 amp 6.3 VDC
2. CLOCK STOP SPDT }
3. CLOCK CIRCUIT OPEN DURING RESET DPDT 3 amp CONTINUOUS 115 VAC
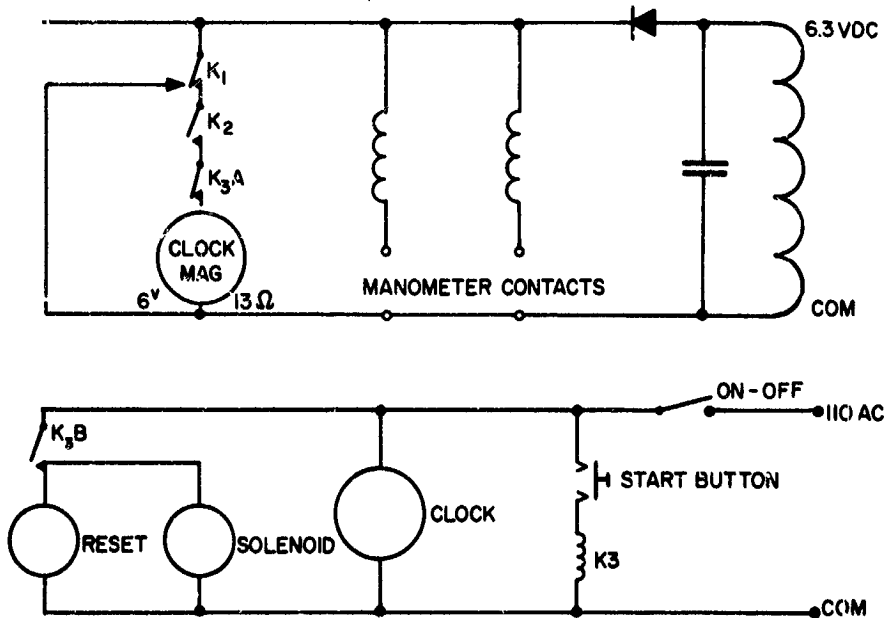
ALL RELAYS SHOWN UNENERGIZED

FIG. 4-9   ELECTRICAL CIRCUIT DIAGRAM OF PERMEABILITY APPARATUS

the apparatus consist of a nitrogen tank, drying tower, solenoid gas valve, mercury manometer, and a gas chamber of known volume. The nitrogen pressure between the tank and the solenoid valve (see Fig. 4-8) is first adjusted so that, when the solenoid valve is opened, the mercury in the manometer rises to above the upper electrical contact embedded in the manometer wall. Energizing of the solenoid also admits nitrogen to the gas chamber of known volume and initiates diffusion of nitrogen through the porous sample. The solenoid is then deenergized by releasing the "start button", and the nitrogen pressure begins to decrease by diffusion through the sample. As the mercury in the manometer breaks from the upper electrical contact, the stop clock is actuated electrically. It continues to run until the mercury breaks from the lower contact, located 40 mm below the upper contact. At this instant, the clock stops, recording the time increment "δt" required for the known gas volume "V" to undergo a 40 mm Hg pressure decrement "δP_{mm}" by diffusion through the porous sample. The "δt" value obtained in this way is accurate to within $\pm$ 0.01 second.

Mass permeability coefficient is then calculated by Carman's formula[1]:

$$K = (\delta m)\left(\frac{L}{A}\right)\left(\frac{1}{\delta t}\right)\left(\frac{1}{\Delta P_{mm}}\right), \quad \text{gm} \cdot \text{cm}^{-1} \cdot \text{sec}^{-1} \cdot \text{mm Hg}^{-1}$$

where

$$\delta m = \frac{\delta P_{mm} \cdot V \cdot M}{RT}, \quad \text{gm of N}_2 \text{ diffusing in } \delta t \text{ seconds}$$

M = gm/mole, molecular weight of N_2

R = ideal gas constant

T = $^\circ$K, absolute temperature

L/A = cm^{-1}, length/area ratio of test sample

ΔP_{mm} = mm Hg, mean differential between gas chamber and atmospheric pressures during δP_{mm} decrement.

1. Carman, P. C., "Flow of Gases Through Porous Media", Butterworth, London, 1949.

All permeability coefficients reported herein were determined using the following parameters:

Diffusant gas, nitrogen

M, 28.02 gm·mole^{-1}

δP_{mm}, 40 mm Hg $\cong$ .0526 atmosphere

ΔP_{mm}, 380 mm Hg

R, 82.057 cm^3·atm·$^{\circ}K^{-1}$·mole^{-1}

T, 298$^{\circ}K$

V, 28 cm^3 } or { 1000 cm^3

δm, $(1.688)(10)^{-3}$ gm } { $(60.273)(10)^{-3}$ gm

The values of permeability coefficient, derived by the foregoing method, not only provide accurate comparisons between porous samples, but are reputed to be independent of the diffusant gas used (providing the gases are stable and non-reactive with the sample).

Permeability coefficients are listed in Tables 4-I, II, and III for all E3, 6, and 7A ionizer buttons prepared. "Permeability vs density" data from these tables are plotted in Fig. 4-10. Here it is seen that the data points lie within distinct bands, the permeability coefficients increasing with decreasing density in a logical manner. Average "permeability vs density" values for the various button categories are indicated by oversized legend characters. Data scatter bands for the machine ground and metallographically polished ionizers are essentially congruous (within each particle size category). This indicates that the machine grinding and polishing operations do not have significantly different effects on ionizer surface distortion and pore closure. However, the data bands for the lathe-turned buttons are consistently shifted to the left toward lower permeabilities, indicating pore closure by surface deformation. As

a result of these findings, it was decided that all ionization testing would be performed on buttons having a standard machine ground surface, rather than the deformed turned surface or the costly metallographic surface.
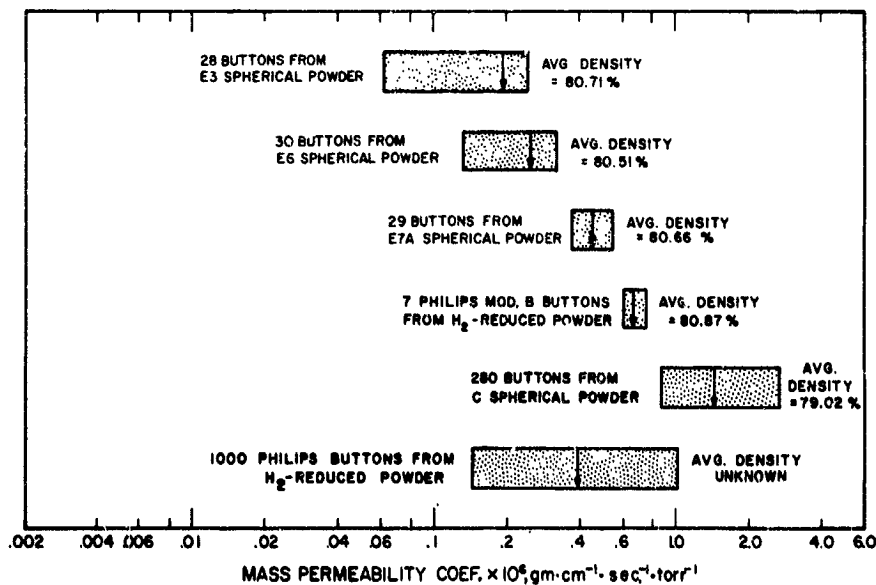
Permeability and transmission coefficient data for the seven buttons of Philips Mod. B tungsten are given in the following tabulation:

Button No.	Density, Percent of Theoretical	Mass. Perm. Coef. $gm \cdot cm^{-1} \cdot sec^{-1} \cdot torr^{-1}$	Transmission Coefficient
PB-G-1	80.62	0.693×10^{-6}	12.845×10^{-5}
PB-G-2	80.57	0.657	12.088
PB-G-3	80.62	0.722	13.383
PB-G-4	81.19	0.602	11.076
PB-G-5	81.30	0.627	11.480
PB-G-6	81.40	0.527	10.919
PB-G-7	80.36	0.752	13.870
Avg.	80.87	0.664×10^{-6}	12.237×10^{-5}

Permeability values for these seven buttons, machined from adjacent locations in a small bar, are quite uniform. Their average permeability of 0.66×10^{-6} is somewhat higher than the 0.46×10^{-6} value obtained for the coarsest spherical powder category, E7A (machine ground). This is shown graphically in Fig. 4-11, where the permeability variance (for all button lots evaluated, current and previous contracts) is plotted.

4.8.3 Derivation of Transmission from Permeability Coefficients

Correlation of mass permeability coefficients with dimensionless transmission coefficients was requested. That such correlation may be invalid is recognized, since transmission coefficient assumes free molecular flow while permeability coefficient was determined with continuum flow. In order to translate permeability to transmission coefficients, it was necessary first to derive the latter in terms of

FIG. 4-10

RELATIONSHIP BETWEEN DENSITY
AND PERMEABILITY FOR IONIZER
BUTTONS, MADE FROM 3 SIZE
FRACTIONS OF TUNGSTEN MICRO-
SPHERES AND PROVIDED WITH
3 DIFFERENT SURFACE FINISHES.
(See Fig. 4-5 for fabrication
procedures.)

FIG. 4-11

COMPARISON OF TOTAL SCATTER
IN PERMEABILITY, OBTAINED
FOR IONIZER BUTTONS MADE
FROM SPHERICAL AND H_2-REDUCED
TUNGSTEN POWDERS. (Average
permeabilities indicated by
arrows.)

the mm Hg pressure units used in the former. This derivation, together with definitions and units of the symbols used, is included as page A10 of the Appendix. It indicates that, for nitrogen gas at 298°K, the transmission coefficient may be expressed as

$$C = \frac{(8.428)(10)^{-5}(V)(\delta P_{mm})}{(A)(\delta t)(P_{mm})} \quad ; \quad or \quad (A)(\delta t) = \frac{(8.428)(10)^{-5}(V)(\delta P_{mm})}{(C)(P_{mm})}$$

As described in Section 4.8.2, mass permeability coefficient is

$$K = \frac{(\delta m)(L)}{(A)(\delta t)(\Delta P_{mm})} \quad ; \quad or \quad (A)(\delta t) = \frac{(\delta m)(L)}{(\Delta P_{mm})(K)}$$

Equating (a) and (b),

$$C = \frac{(8.428)(10)^{-5}(V)(\delta P_{mm})(\Delta P_{mm})}{(P_{mm})(\delta m)} \cdot \frac{K}{L}$$

Substituting in (c)
the parameters: $V = 28$ cm^3, $\delta P_{mm} = 40$ mm Hg, $\Delta P_{mm} = 380$ mm Hg

$$P_{mm} = 1120 \text{ mm Hg, and } \delta m = (1.688)(10)^{-3} \text{ gm}$$

$$C = \frac{18.973 \text{ K}}{L} \text{ , dimensionless}$$

In checking that the value of C (calculated from C = 18.973 K/L) is non-dimensional, it is necessary to refer to equation (8) on page 10 of the Appendix. Here the units of $\sqrt{2\pi \text{ M/RT}}$ [*] $\textbf{t}$ $(8.428)(10)^{-5}$ are sec·cm^{-1}. Inserting (into equation (c) above) the sec·cm^{-1} units for $(8.428)(10)^{-5}$, along with units of the other para-meters used, the units of the 18.973 factor become cm^2·sec·mm Hg·gm^{-1}. These units, in turn, cancel those of the K/L ratio.

-----

[*] Where M = gm/mole, R = ergs/mole·deg, and T = deg.

4.8.4 Mercury Intrusion

The feasibility of characterizing the pore structures of tungsten ionizers by mercury intrusion was determined under this contract. The intrusion method appeared to offer several advantages over optical methods, since it eliminates the need for developing the true pore structure by metallographic polishing and removes the element of human error possible with pore counting and intercept methods. Further, mercury intrusion offered promise as an economical quality-control method.

All mercury intrusion data reported herein were obtained at the Prado Laboratories of Cleveland, Ohio, using an Aminco-Winslow Porosimeter. This apparatus consists primarily of a pump to evacuate the sample, a mercury pressurizing mechanism, and a Penetrometer component shown in Fig. 4-12. After evacuation of air from the sample, mercury is forced into the pores under pressures up to about 5,000 psi and the cumulative volumes intruded are measured at standardized levels of increasing pressure. For pores of the capillary type, correlation of mercury pressure with cylindrical pore diameter is obtained through the Dupré formula $D = -4\varepsilon \cos \theta / P$, cm. Here ε (the surface tension of Hg) is taken as 473 dynes/cm, and θ (the wetting angle of Hg) as 130°, such that the units of P are dynes/cm^2.

Application of the Dupré formula to the intrusion data for sintered tungsten ionizers yielded mean pore diameter values several times smaller than values calculated from pore counts on random cross sections. In retrospect, the reason for such discrepancies appears to be that the ionizer structures are not of the simply capillary type. Rather, they consist of interconnected networks of channels of greatly variable cross section. Thus, what appears in a plane view as a large pore is actually a void space, connected to the maze structure by perhaps several restricted channels or necks. Thus, treatment of the intrusion data <u>as for capillary porosity</u> can lead to interpreting a single (relatively) large void as many small capillaries, having

SAMPLE ENCLOSED IN
HEAD OF PENETROMETER

VACUUM TUBING

FILLING DEVICE (UPPER)

PENETROMETER STEM

FILLING DEVICE (LOWER)

ATMOSPHERE TUBE
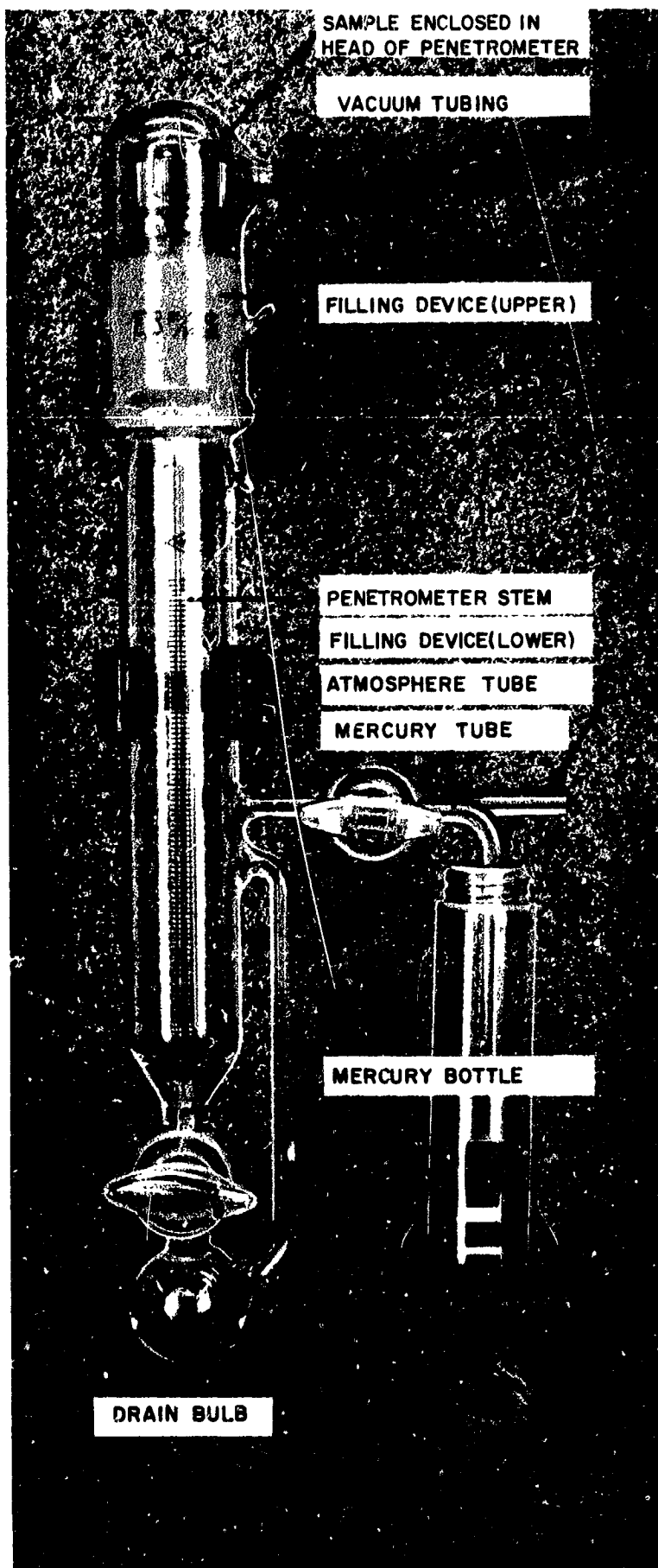
MERCURY TUBE

MERCURY BOTTLE

DRAIN BULB

FIG. 4-12   AMINCO-WINSLOW PENETROMETER IN OPERATING
POSITION WITH FILLING DEVICE

the diameter of the largest access channel. This, in turn, leads to concluding a smaller-than-actual mean pore size and pore size distribution than determinable directly from photomicrographs.

Since complex ionizer structures apparently do not permit application of the Dupré capillary formula, actual mercury pressure ranges (rather than correlated pore size ranges) are listed in Table 4-IV. Here, the mercury intruded over the respective pressure ranges is expressed both as cm^3 volume and as a percent of sample volume. These data indicate the _relative_ restriction of the complex maze structures, i.e., the more restricted the maze, the higher the pressure required to intrude mercury. Boxed valves in Table 4-IV, indicate the largest intruded volumes and may be compared readily to the intrusion pressure for the various samples.

Densities of the intruded samples are expressed in Table 4-IV as a percent of the theoretical density of tungsten. Total pore volume, expressed as a percent of sample volume, is calculated simply as 100 percent - percent of theoretical density. Occluded pore volume is taken as total pore volume minus open pore volume, where open pore volume equals the total volume of mercury intruded. In general, Table 4-IV indicates that the finer the starting powder, the greater the occluded pore volume after sintering. This effect is more apparent for the unsized spherical powder samples than for the sized powder samples.

Data obtained on Philips Mod. B H_2-reduced tungsten and on unsized (coarse) Lot C tungsten are included in Table 4-IV for comparison purposes, the latter having been used exclusively in the previous contract. The initial average particle diameter of the Philips base powder could not be obtained, while the 3.47μ diameter given for Lot C is taken to be the same as that of Lot D (analyzed under this contract). This assumption is believed to be reasonable since Lot C and D powders were reported by the Linde Co. to have been produced by the same technique from the same starting material.

TABLE 4-IV   DENSITY, PORE VOLUME, AND MERCURY INTRUSION DATA FOR SINTERED TUNGSTEN, MADE FROM VARIOUS POWDER LOTS

Powder Type	Spherical	H₂-Reduced Philips* Metalonics Mod. B	Spherical	Spherical	Spherical	Spherical
Powder Lot No.	E		C	E	E	E
Classifier Run No.	Unsized		Unsized	3	6	7A
Avg. Particle Dia., μ	0.91		3.47	2.72	4.87	6.92
Vol. of Sample, V_s, cm³	0.32250	0.35076	0.36275	0.32509	0.34798	0.37099
Density, % of Theor.	83.52	81.50	79.02	79.63	80.31	80.73
Total Pore Vol., % of V_s	15.48	18.50	20.98	20.37	19.69	19.27
Open Pore Vol., % of V_s	15.19	17.53	20.68	19.70	19.25	18.87
Occluded Pore Vol., % of V_s	1.29	0.97	0.30	0.67	0.44	0.40

Mercury Intruded Over Respective Pressure Ranges

Mercury Pressure Range, psi	ΔV, cm³	% of V_s	ΔV, cm³	% of V_s	ΔV, cm³	% of V_s	ΔV, cm³	% of V_s	ΔV, cm³	% of V_s	ΔV, cm³	% of V_s
43-55	nil	nil	nil	nil	0.001	0.28	nil	nil	nil	nil	nil	nil
55-73	nil	nil	0.002	0.57	0.052	14.33	nil	nil	nil	nil	nil	nil
73-102	nil	nil	0.054	15.39	0.018	4.96	nil	nil	0.001	0.29	0.001	0.27
102-160	0.001	0.31	0.004	1.14	0.003	0.83	0.001	0.31	0.037	10.63	0.064	17.25
160-235	0.042	13.02	0.001	0.29	0.001	0.28	0.055	16.92	0.026	7.47	0.004	1.08
235-335	0.004	1.24	nil	nil	nil	nil	0.006	1.85	0.002	0.57	nil	nil
335-568	0.001	0.31	nil	nil	nil	nil	0.001	0.31	nil	nil	nil	nil
568-1735	0.001	0.31	0.0005	0.14	nil	nil	0.001	0.31	0.001	0.29	0.001	0.27
Totals	0.049	15.19	0.0615	17.53	0.075	20.68	0.064	19.70	0.067	19.25	0.070	18.87

*Mod. B Grade, reported to have finest pore size sold in large ionizers as of 11/63.

The data of Table 4-IV indicate, as expected, that the pore structure of the unsized (fine) E powder ionizer is finer than that of the unsized (coarse) C powder ionizer. The pore structure of the Mod. B tungsten is indicated to lie between the unsized E and C tungsten, but closer to the latter. The intrusion data, given for the unsized E sample in Table 4-IV, are surprisingly similar to those of the E-fraction 3 sample. Samples prepared from sized Lot E powder, fractions 3, 6, and 7A, are indicated to form a series having increasing coarseness of pore structure. This is readily apparent in Fig. 4-13, where open pore volume is plotted against mercury intrusion pressure.

4.8.5 Metallographic Analysis

Metallographic analysis provides information on pore diameter, number of pores per unit area, structural uniformity, pore configuration, and width of diffusion bridges, as well as allowing direct visual comparisons. Techniques for defining the structure of porous tungsten have received considerable attention under this contract, and great strides have been made toward the end objective of revealing the true pore structure.

The preferred materials and general technique used to polish unalloyed porous tungsten under this contract are as follows:

|	
Mounting Material	- Green Bakelite (Buehler No. 1382)
Mounting Pressure	- 4200 psi
Grinding Papers	- 240 Silicon Carbide (1st)
	- 320 Silicon Carbide
	- 400 Silicon Carbide
	- 600 Silicon Carbide (last)
Polishing Cloth	- Nylon (Buehler No. 40-7058)
Polishing Wheel Speed	- 930 RPM
Polishing Abrasives	- Linde A (0.3μ Al_2O_3) in water (1st)
	- Linde B (0.05μ Al_2O_3) in water (2nd)
Etching	- By differential oxidation of Cu-base infiltrant at $150^{\circ}C$ in air for 10-20 minutes.
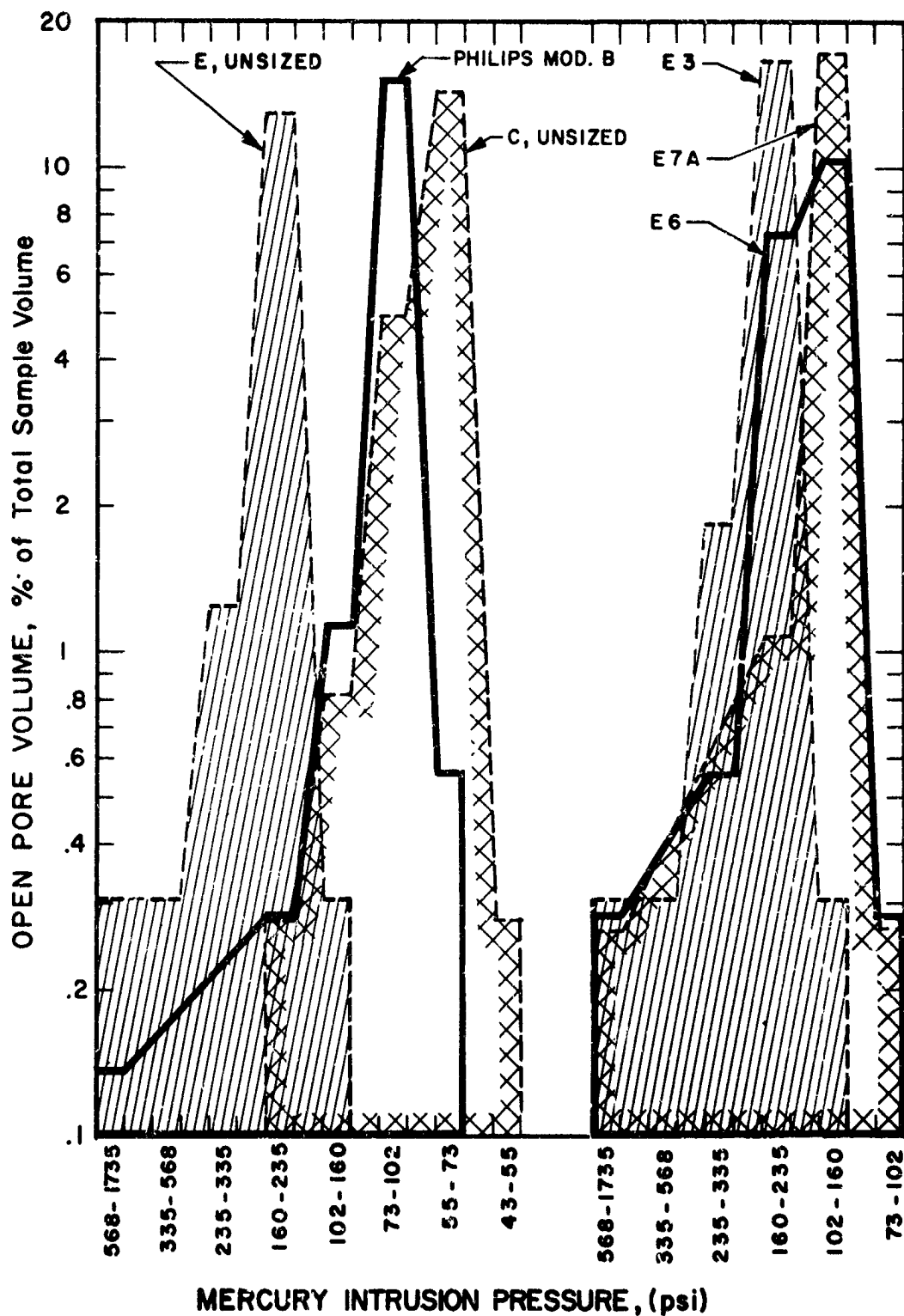
FIG. 4-13 MERCURY INTRUSION DATA FOR SINTERED TUNGSTEN SAMPLES

Microstructures were obtained on representative samples of all experimental materials developed, as well as on commercial (H_2-reduced) porous tungsten. All photomicrographs were taken on Cu infiltrated buttons and at 400 x magnifications or higher.

Figure 4-14 shows the pore structure of a fine (H_2-reduced) powder ionizer, the permeability of which was at the mean value of 1000 buttons. Its structure is compared to that of Philips Mod. B tungsten, also reported to be prepared from H_2-reduced powder. Typical and inhomogeneous areas are shown for both materials.

Figure 4-15 shows the typical pore structures of all classified spherical powder ionizers prepared under this contract, plus that of an ionizer (CU-48-2) prepared under the previous contract. Figure 4-15 also includes the structure of an ionizer button (EU-4) prepared from unclassified (fine) Lot E powder. Data on the parameters of the powders used, and on final (distilled) density and permeability are also indicated. The marked pore size difference between the unclassified Lot E (fine) and Lot C (coarse) powder buttons is immediately apparent. The increasing pore refinement of the E7A, 6, and 3 buttons is also apparent. The general pore size of EU-4 would appear to be comparable to E6-P-9. Comparison of the unclassified powder buttons with the classified buttons indicates that the former undergo appreciably more particle agglomeration than do the latter, apparently due to the relatively-large initial percentages of fine particles. This observation is in agreement with metallurgical expectation.
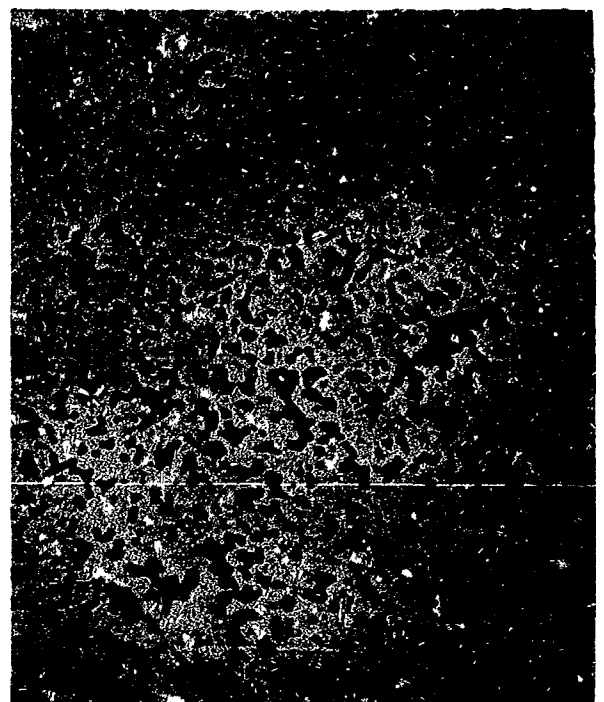
Figure 4-16 shows inhomogeneous areas in the same series of buttons (illustrated in Fig. 4-15, preceding). These areas are results of initial powder-packing faults and are not considered as serious shortcomings, due to their infrequency. This is demonstrated in the 20 x macrographs of Fig. 4-17.

Revelation of the finest pores in porous tungsten by metallographic polishing is extremely difficult, such that progressive
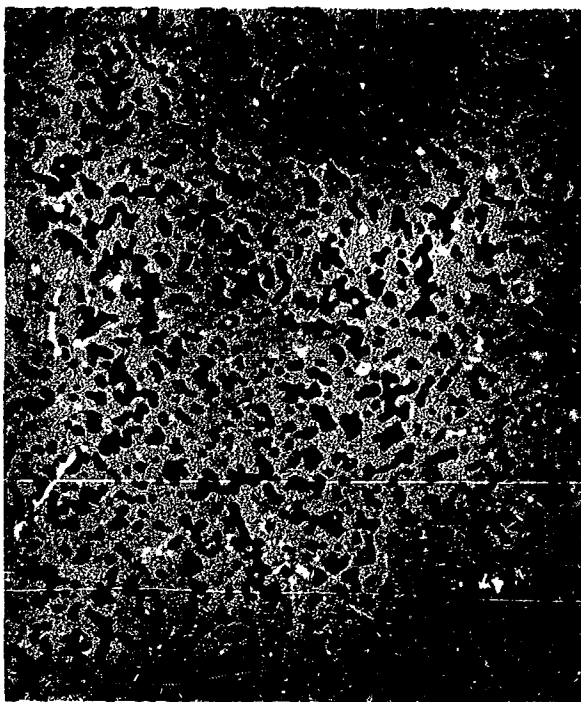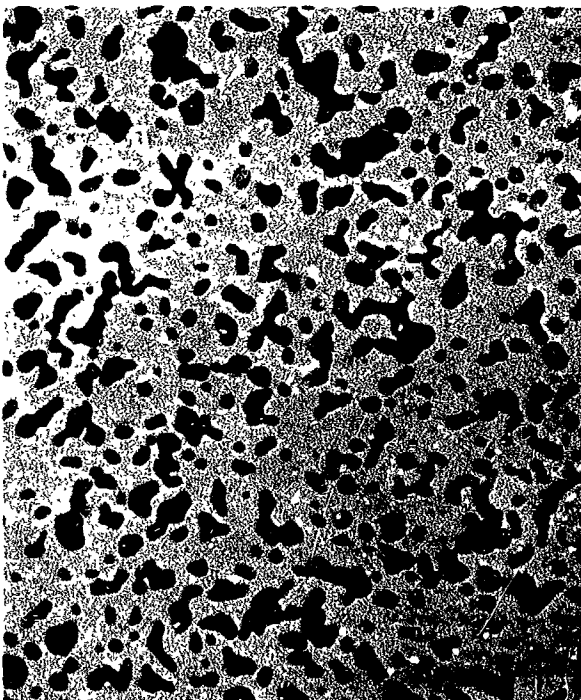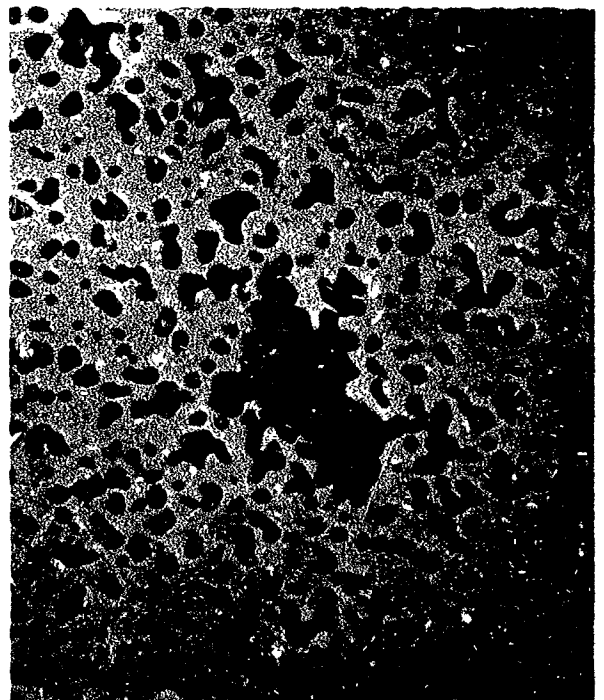
NEG. 1269   TYPICAL AREA   NEG. 1270   INHOMOGENEOUS AREA

DENSITY = 79.1%
MASS PERM. COEF. = 0.34 X 10^{-6}

NEG. 1320   TYPICAL AREA   NEG. 1321   INHOMOGENEOUS AREA

MOD. B GRADE
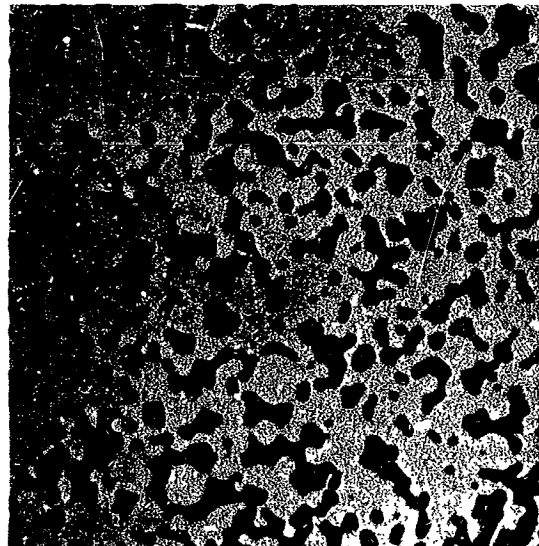DENSITY = 81.2%
MASS PERM. COEF. = 0.60 X 10^{-6}

FIG. 4-14   TYPICAL AND INHOMOGENEOUS AREAS IN IONIZER BUTTONS MADE FROM
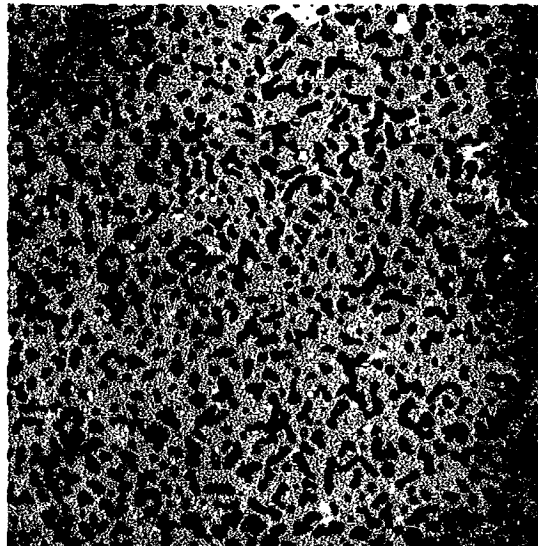H_2-REDUCED TUNGSTEN POWDER BY PHILIPS METALONICS (Mag. = 400X)

FIG. 4-15

TYPICAL PORE STRUCTURE OF TUNGSTEN
IONIZERS MADE FROM VARIOUS SIZE
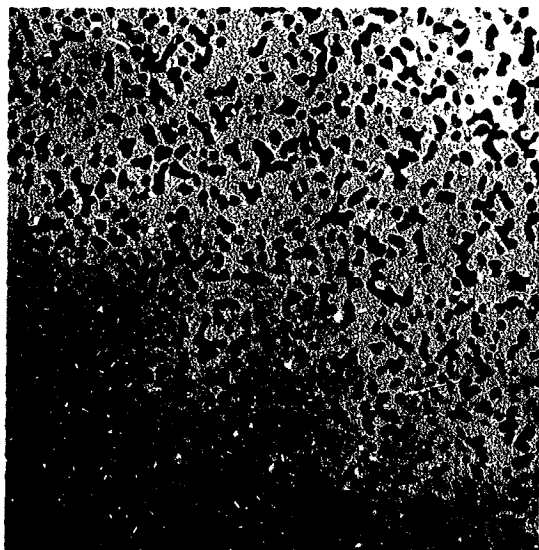DISTRIBUTIONS OF MICROSPHERES.
(Mag. = 400X)
UPPER LEFT - LOT E, UNCLASSIFIED
UPPER RIGHT - LOT C, UNCLASSIFIED
LOWER LEFT - LOT E, FRACTION 3
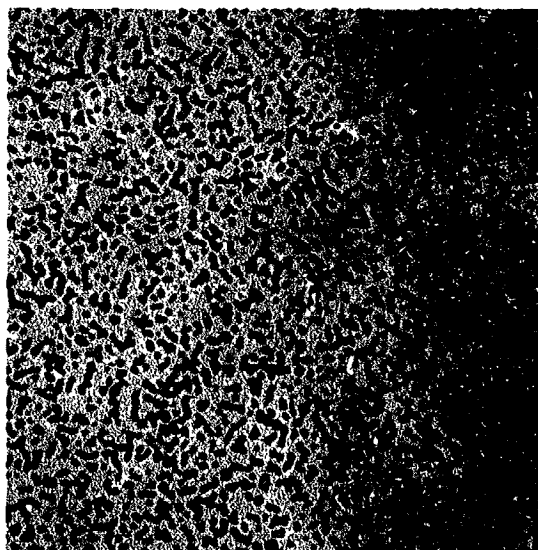LOWER CENTER - LOT E, FRACTION 6
LOWER RIGHT - LOT E, FRACTION 7A

NEG. 1312
BUTTON EU-4
DENSITY 82.4%
MASS PERM. COEF. = 0.17 X 10⁻⁶

| | % BY | PARTICLE DIA., μ | |
	NO.	RANGE	AVERAGE
	88.2	0-2	0.91

NEG. 1272
BUTTON CU-48-2
DENSITY 79.2%
MASS PERM. COEF. = 0.85 X 10⁻⁶

| | % BY | PARTICLE DIA., μ | |
	NO.	RANGE	AVERAGE
	88.9	1-7	3.47

NEG. 1267
BUTTON E7A-P-1
DENSITY 80.5%
MASS PERM. COEF. = 0.50 X 10⁻⁶
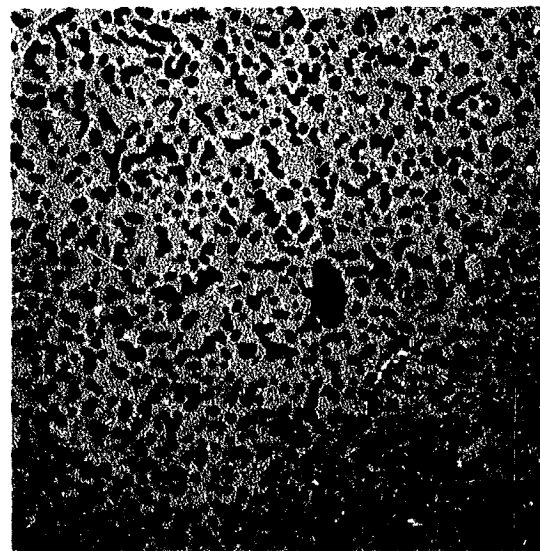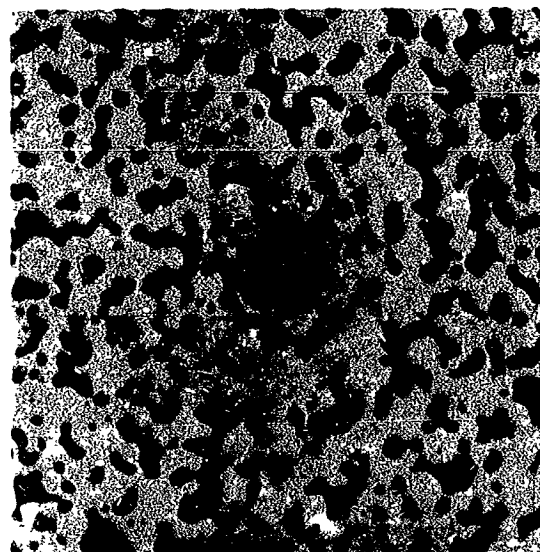
| | % BY | PARTICLE DIA., μ | |
	NO.	RANGE	AVERAGE
	88.2	4-9	6.92

NEG. 1258
BUTTON E3-P-1
DENSITY 80.6%
MASS PERM. COEF. = 0.21 X 10⁻⁶

| | % BY | PARTICLE DIA., μ | |
	NO.	RANGE	AVERAGE
	88.7	1-4	2.72

NEG. 1263
BUTTON E6-P-9
DENSITY 79.8%
MASS PERM. COEF. = 0.33 X 10⁻⁶

| | % BY | PARTICLE DIA., μ | |
	NO.	RANGE	AVERAGE
	84.1	3-6	4.87
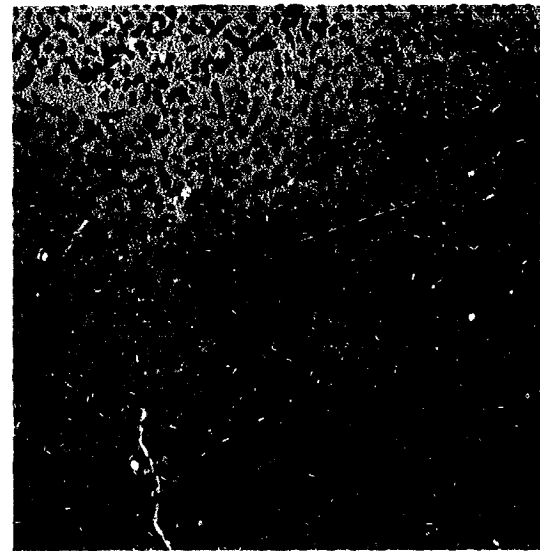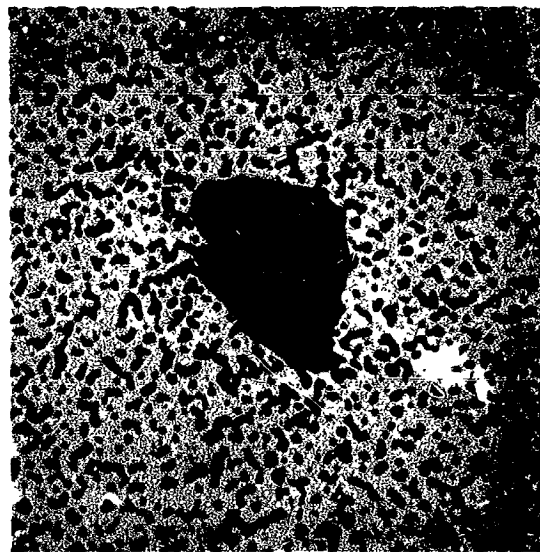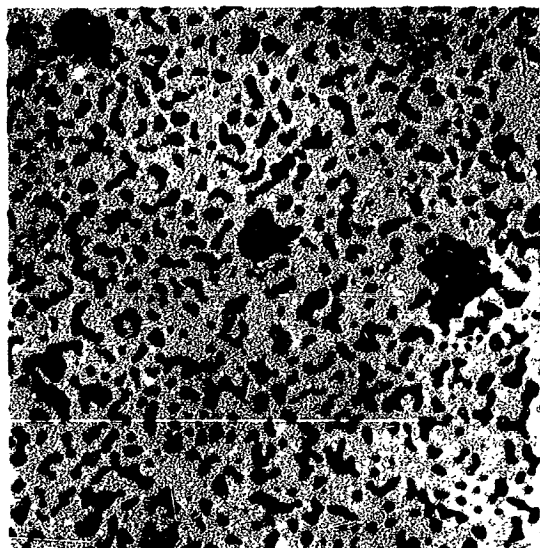
FIG. 4-16

LARGE PORES IN RESPECTIVE
IONIZERS, DESCRIBED IN
PRECEDING FIGURE

IONIZER E7A-P-1

NEG. 1266

IONIZER CU-48-2

NEG. 1273

IONIZER E6-P-9

NEG. 1264

IONIZER EU-4

NEG. 1338

IONIZER E3-P-1

NEG. 1259
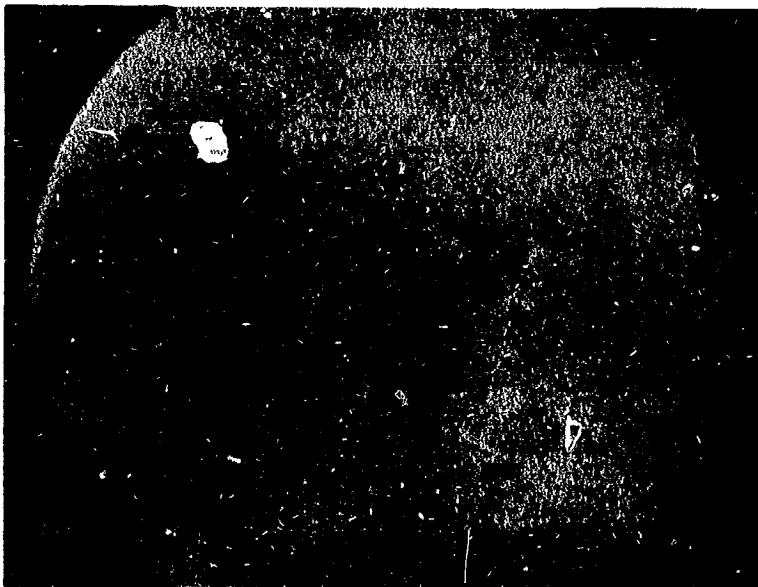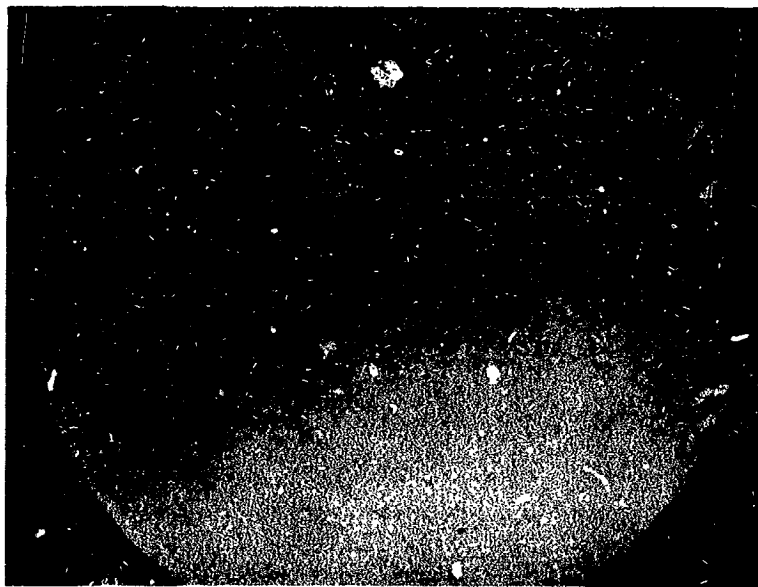
NEG. 1262   IONIZER E3-P-1   NEG. 1265   IONIZER E6-P-9   NEG. 1268   IONIZER E7A-P-1
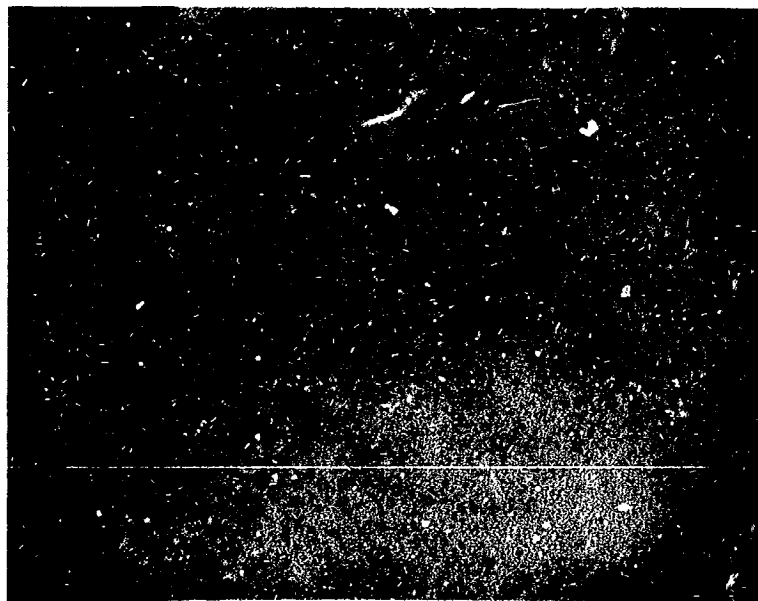
FIG. 4-17   TUNGSTEN IONIZERS, MADE FROM 3 SIZE FRACTIONS OF LOT E MICROSPHERES, SHOWING FREQUENCY OF LARGE PORES
(Mag. = 20X)

improvements in technique have brought to light finer and finer pores. The following conclusions are noted as being pertinent to this problem.

(1) A reasonable facsimile of true pore structure has not been shown on non-infiltrated tungsten.

(2) An infiltrant, softer than the tungsten matrix (such as Cu or Ag) tends to polish in relief, i.e., below the plane of the tungsten.

(3) Despite the non-ductile nature of tungsten at room temperature, it has a marked tendency to smear when polished and to cover the infiltrated pores. This tendency is particularly pronounced with respect to the very fine pores.

(4) Because of (3), it is desirable to terminate the surface preparation with alternate light polishing - chemical etching, with etching being the very last step. When properly prepared, the tungsten grain boundaries should be faintly visible.

(5) Choice of metallographic lens becomes a compromise between one having adequate depth of focus to accommodate surface relief and one having good resolving power (with lesser depth of focus).

4.8.6 Determination of Mean Pore Diameter and Pores per Unit Area from Pore Counts

Using metallographic polishing techniques described in the foregoing section, ionizers from each powder category were photographed at either 1,200 or 2,000 x magnification. A minimum of four randomly-selected areas were photographed on each ionizer. Rectangles 8 x 10 cm were drawn accurately on each photomicrograph. All pores inscribed were counted, and pores intersected by the edges of the rectangle were tallied as half pores. Pores per unit area were then calculated as:

$$\frac{(Pores\ Counted)(Mag.)^2}{(10)(80)} = \frac{Pores}{cm^2}$$

Mean pore diameters were calculated from the pores per unit area values. It was assumed that the cross section of a

photomicrograph shows a percent pore area equal to the percent open pore volume (obtained by Hg intrusion). This assumption is valid for a random section plane of homogenously porous material. Calculation of mean pore diameter was as follows:

Pore area fraction/Area of a mean pore = Pores per unit area

$$\frac{\pi \bar{d}^2}{4} = \frac{\text{Pore area fraction}}{\text{Pores per unit area}} = \frac{\text{Percent open pore volume}}{(100)(\text{Pores per unit area})}$$

$$\bar{d} = 0.1128\sqrt{\frac{\text{Percent open pore volume}}{\text{Pores per unit area}}}$$

Values of mean pore diameter and pores per unit area (obtained from pore counts) are given in Table 4-V for the various ionizer categories.

4.8.7 Spherical Powder Parameters vs Final Pore Characteristics of Ionizers

A summary correlating spherical powder parameters with ionizer pore characteristics is presented as Table 4-V. The data listed indicate generally that, as the mean diameter of the initial particles increases:

(a) the volume of occluded pores decreases

(b) the mean pore diameter increases

(c) the number of pores per unit area decreases

(d) the permeability and transmission coefficients increase

The unclassified Lot C powder, having the broadest size distribution (88.9 percent of 1-7μ particles) and a mean particle diameter of only 3.47μ, yielded the coarsest pore structure. It was necessary, however, to sinter this powder at 2,200°C for 70 minutes to reach target density. It is reasonable that appreciable diffusion of small into large particles occurred at this temperature, resulting in a much coarser porosity than the mean initial particle diameter would indicate. The

TABLE 4-V   SUMMARY DATA FOR SINTERED IONIZERS, CORRELATING THE TUNGSTEN POWDER USED WITH DENSITY, POROSITY AND PERMEABILITY VALUES OBTAINED

| Tungsten Powder | | | Predominant Particles | | Average Particle Dia., μ | Sintered Density, % of Theor. | Total Pore Vol., % of Vol total | Open* Pore Vol., % of Vol total | Occluded* Pore Vol., % of Vol total | Average** Pore Dia., μ | No. of** Pores per cm2 $\times 10^6$ | Mass Perm. Coef., g.cm^{-1} sec.torr^{-1} | | | Average Transmission Coef. $\times 10^{-5}$ |
Type	Lot	Fraction	% by No.	in μ Range								No. of Buttons	Scatter of Perm. $\times 10^{-6}$	Average Perm. $\times 10^{-6}$	
Spherical	E	As-Produced (Unclassified)	88.2	0-2	0.91	83.52	16.48	15.19	1.29	--	--	15	.018-.243	.131	2.448
Spherical	E	3	88.7	1-4	2.72	79.63	20.37	19.70	0.67	2.50	4.01	28	.062-.248	.193	3.881
Spherical	E	6	84.1	3-6	4.87	80.31	19.69	19.25	0.44	3.51	1.99	30	.132-.325	.252	4.950
Spherical	E	7A	88.2	4-9	6.92	80.73	19.27	18.87	0.40	3.83	1.64	29	.370-.555	.450	8.843
Spherical	C	As-Produced (Unclassified)	88.9	1-7	3.47	79.02	20.98	20.68	0.30	5.88	0.76	280	.848-2.677	1.411	-

*Calculated from mercury intrusion data

**Calculated from pore counts

Philips Mod. B material is not included in summary Table 4-V since it was made, reportedly, from H_2-reduced powder, the size distribution of which could not be obtained by Electro-Optical Systems.

5. IONIZATION PERFORMANCE OF SINTERED POWDER

The ionization performance was obtained by the measurement of neutral fraction and critical temperature as a function of ion current density and ionizer structure (i.e., pore size and pore density). These parameters are representative of the ionization (propellant utilization) efficiency and ion generation energy efficiency, respectively. These criteria are related to ion engine parameters and treated in detail in[1].

5.1 Test Apparatus and Instrumentation

The ionizer test apparatus was similar to that used in experiments described by La Chance, et al[2,3,4]. The modifications include a looped cesium feed tube and gas cooling coil on the ionizer-reservoir assembly, insulator shields and simplified feedthroughs for the ion engine, larger slits and larger filaments for the neutral detector, and an indirectly cooled collector (see Figs. 5-1 and 5-4).

The ionizers were Mo-C-B brazed to the molybdenum holder which was directly heated by a sheathed tantalum heater. Ionizer temperature was measured with a W5% Re - W26% Re thermocouple in a 1/16" O.D. tantalum sheath. This sheath became brittle and frequently failed during disassembly. The thermocouple junction and sheath was subsequently rewelded. The cesium reservoir temperature was measured with a chromel-alumel thermocouple in an inconel sheath. The thermocouples and cooling

1. G. Kuskevics, "Criteria and a Graphical Method for Optimization of Cesium Surface Ionizer Materials", Electro-Optical Systems, Inc. RR-3, January 1962.

2. M. LaChance and G. Kuskevics, "Ionizer-Reservoir Development Studies", Electro-Optical Systems, Inc. 2150 Final Report, May 1963.

3. G. Kuskevics and B. L. Thompson, "Comparison of Commercial Spherical Powder and Wire Bundle Tungsten Ionizers", AIAA Jour. 2, No. 2, 284-294,(1964).

4. G. Kuskevics and J. M. Teem, "Surface Ion Source Phenomena and Technology", Electro-Optical Systems, Inc. RR-16, September 1963.
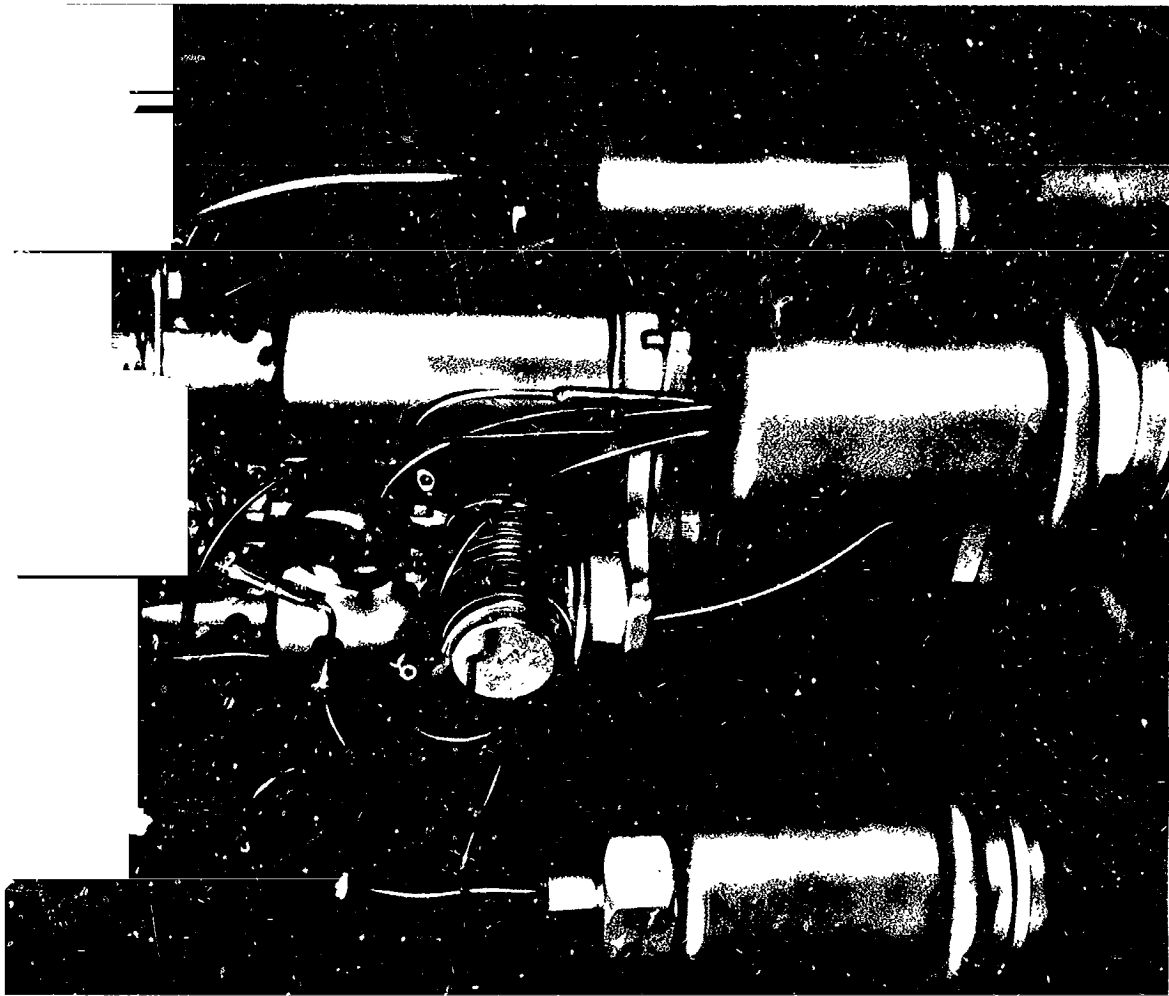
FIG. 5-1 MODIFIED ION SOURCE SHOWING LOOPED FEED TUBE, RESERVOIR COOLING
COIL AND INSULATOR SHIELDS

lines passed through one alumina high-voltage insulator with a neoprene gasket seal also serving as the low voltage insulator. Both temperatures were recorded on a 2-channel potentiometric type recorder which operated at the high voltage. A special circuit chopped the ionizer thermocouple output, then put it through a high voltage isolation transformer so that it could be recorded at near ground potential versus the ion beam current on a X-Y recorder.

The accelerator structure shown in Fig. 5-2 uses a 45° beam former and accel-decel electrodes in conjunction with -25 kv accel and +7.5 kv ionizer high voltage supplies which limited the maximum ion current density to about 60 ma/cm^2. A special tool was used to align electrodes to within $\pm$0.01".

The emitter and accelerator currents can be measured on multi-range ammeters.

For all experiments, the M2 neutral atom detector (see Fig. 5-3) could be rotated about an axis point through the ionizer. The ionizer-to-detector filament distance was 6 inches. The slits were enlarged to 0.040" x 0.200". The angular position was about 15° to the geometric beam axis with some adjustment to correct background and stay out of the energetic ion beam. The detector was equipped with a shutter operated by an electromagnet.

The ion collector shown in Fig. 5-4 has straight (instead of concentric) copper baffles at 45°. The structure is cooled by radiation and conduction (not directly as before) from the liquid nitrogen liner. The tungsten ribbons used for secondary electron suppression were 0.003" thick and 0.100" deep, intercepting several percent of the beam. A -90V suppression voltage was used. The collector current is recorded on a potentiometric chart recorder and the X-Y recorder.

The new vacuum system shown in Fig. 5-4 used in these experiments was capable of operating in the 10^{-8} torr range without load and in the high 10^{-7} torr range during the high current operation periods. The 1 x 3 ft. chamber has a flooded stainless steel LN$_2$ liner. The 10" oil diffusion
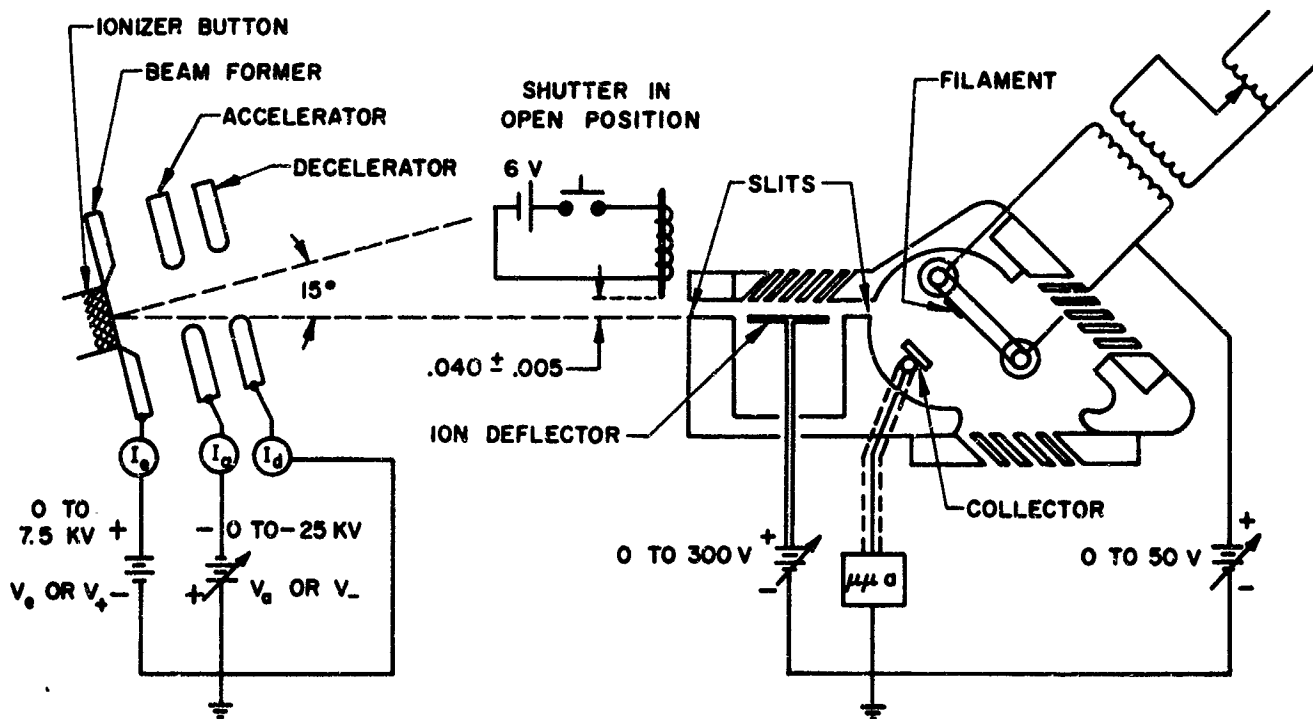
FIG. 5-2   SCHEMATIC AND CIRCUIT DIAGRAM OF ION ACCELERATOR AND
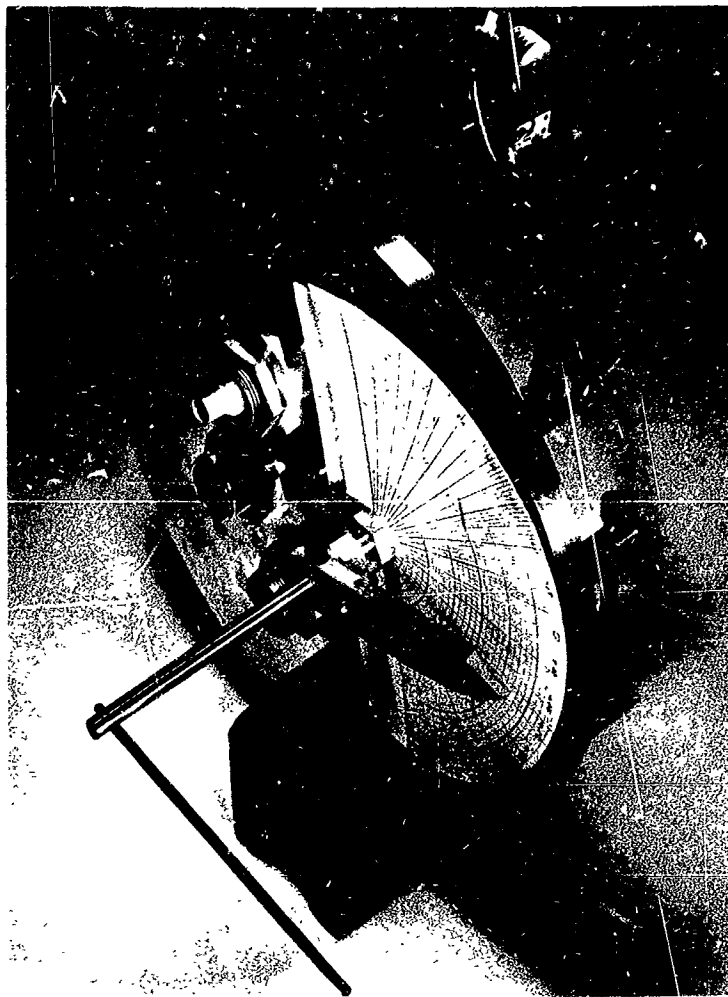NEUTRAL DETECTOR

FIG. 5-3

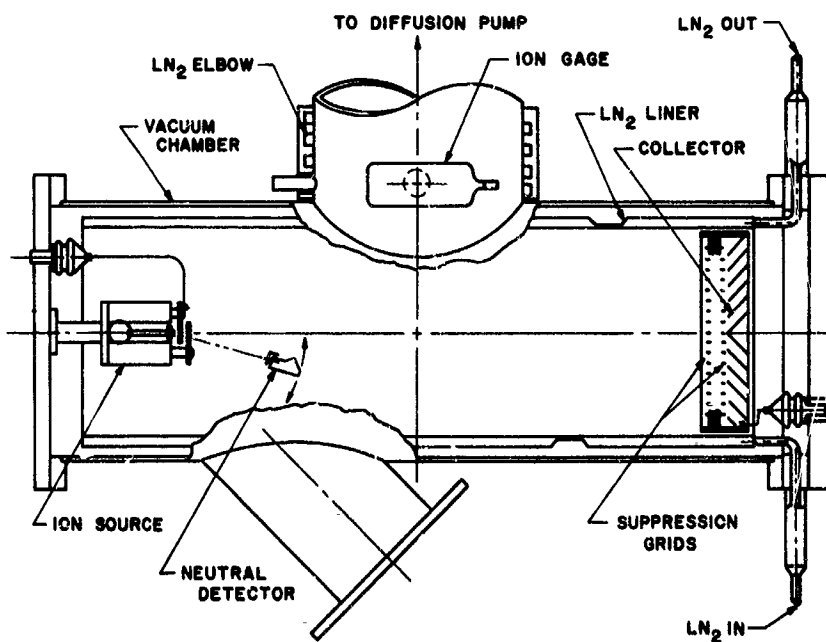MOVABLE NEUTRAL DETECTOR AND
ITS VACUUM FLANGE

FIG. 5-4

SCHEMATIC OF VACUUM CHAMBER WITH
ION SOURCE, NEUTRAL DETECTOR AND
ION COLLECTOR

pump was connected to the vacuum chamber through a liquid nitrogen cooled elbow which served as an antimigration trap. With the multihole liner in front of it and the single 45° restriction, it is a two-bounce trap.

5.2 Test Procedure

To measure the ionization properties of a porous ionizer, it must be sealed into a leak-tight high temperature assembly which is connected to a medium temperature cesium reservoir. After reservoir loading and ionizer conditioning the critical temperature and neutral fraction are measured for different cesium flow rates.

Even though the nitrogen permeabilities of the porous materials have already been measured previously, the apparent nitrogen permeability of the selected ionizers is measured again after brazing and after ionization measurements. Comparison of these values allow the detection of leaks, indicate the amount of braze infiltration, and show the ionizer stability during the test.

The ionizer temperature is raised to 1840°C in 10 min. during brazing and allowed to cool for an hour. It remains near the brazing temperature only for a few seconds. The assembly is bubble-tested under acetone and photographed to record the appearance (such as surface finish, braze infiltration, surface defects).

A few grams of cesium were loaded into the reservoir using regular dry box techniques. The oxygen content of the cesium is not known. Upon removal of the ionizer assembly from the dry box, the cesium in the reservoir is under one atmosphere pressure of nitrogen. The low permeability of the porous ionizer is the only barrier against the infusion of air while the assembly is mounted into the accelerator and transferred into the vacuum test chamber.

Next the active ion emission area is measured by the diode sputtering pattern method described in[5]. With a gap of 0.100" to 0.170" an accelerating voltage of 6 kv insures emission-limited operation and reduces

5. G. Kuskevics and B. L. Thompson, "Comparison of Commercial Spherical Powder and Wire Bundle Tungsten Ionizers", AIAA Jour. 2, No. 2, 284-294, (1964).

space charge spreading. Then with the accel-decel structure, the ionizer is heated to about 1250°C while the vacuum is about 10^{-7} torr. The reservoir temperature is raised slowly to about 0.5 ma (3 ma/cm^2) with the +5 kv on the ionizer and -10 kv on the accelerator electrode. The X-Y recorder is calibrated against the chart recorders. Ion beam is observed by raising argon pressure in the tank to see that all of it hits the target. The glow at the target within the beam impact area and target current voltage characteristic also provides a check on this. The secondary electron suppression is checked by observing constancy of target current with 45 and 90 volts.

The neutral detector alignment is checked by insuring that the light from its filament illuminates the porous ionizer. The filament is baked at 1200°C until background current is a few nanoamps. The shutter operation, ion deflection and filament voltage are checked. The neutral fraction is checked over angles between 10-20° to check on its constancy and best location. The ion current-voltage characteristics are checked prior to each measurement at a new flow rate.

Ion current and neutral fraction versus ionizer temperature curves are monitored at the low flow rate until the critical temperature and neutral fraction reaches a stable value. This is referred to as the initial conditioning period. There is some conditioning at the beginning of each day.

More detailed description of the measurement procedures and accuracy limits is given in Ref. 6.

5.3 <u>Mechanical Parameters and Nitrogen Permeability of Ionizers Selected for Ionization Tests</u>

The mechanical parameters, such as, material density, total cross section area, thickness, permeability and transmission coefficient, average pore size, and pore density for the ionizers selected for testing are given in Table 5-I. Ground finished ionizers with average density and permeability were selected for these tests. The surface usually showed pronounced grinding marks as in Fig. 4-4. Best overall representation of

6. G. Kuskevics and J. M. Teem, "Surface Ion Source Phenomena and Technology", Electro-Optical Systems, Inc. RR-16, September 1963.

3720-Final

Table 5-I

Mechanical Parameters of Selected Ionizers

Type	1-4μ			3-6μ	4-8μ		CSW	CSW
Metall. designation	E3-G-3	E3-G-2	E3-G-5	E6-G-5	E7A-G-7	E7A-G-8	PB-G-6	PB-G-5
Total area, cm²	0.169	0.169	0.169	0.176	0.178	0.177	0.178	0.179
Active area, cm²	0.154*		0.150	0.162	0.112**	0.161		
Thickness, cm	0.0937	0.0937	0.0937	0.0965	0.0965	0.0962	0.1028	0.1039
% density	80.47	80.62	80.41	79.90	80.52	80.41	81.50	81.30
Permeability, μP	0.217	0.222	0.232	0.308	0.467	0.0485	0.592	0.627
Transm. Coeff.	4.38	4.496	4.705	6.05	8.37	9.50		
P after brazing, μP	0.140	0.165	0.164	0.220	0.288	0.369	0.161	0.207
Avg. pore dia, μ		2.50		3.51	3.83		5.53	
Avg. part. size, μ		2.72		4.87	6.92		--	
Pores per cm²	4.01x10⁶			1.99x10⁶	1.64x10⁶		0.73x10⁶	

* decreased to 0.143 cm² due to melted spots

** from photograph

the structures are the photomicrographs which show not only the pore size, size distribution, interpore distance, but also pore shape, pore density and uniformity of pore distribution. Comparisons of typical structures, similar to those selected for the ionization tests, can be made by examining Figs. 4-14 and 4-15. The fine commercial porous tungsten bars available in 0.6" cross section only, appear to have a pore size somewhere between the fine (Lot EU) and coarse (Lot CU) unsized spherical powder buttons, but with larger and much less uniform pore structure than the coarsest of the sized powder ionizers (E7A). The coarse commercial porous tungsten (Philips Mod. B) is nearly similar to the coarse unsized spherical powder material. There is no question, based on the photomicrographs, that sized Lot E3 powder ionizers have the finest, most uniform structure.

The nitrogen permeability is very sensitive to the slightest change in material density, pore size and surface finish as shown in Fig. 4-10. Thus, for sized spherical powder ionizers, the permeability decreases by .01µP [this unit will be used for $\mu gm/(cm.sec.torr)$] for a 2% increase in theoretical density (i. e., from 80% to 82%). For equal theoretical density of 80%, the permeability increases from E3 (1-4µ) to E6 (3-6µ) to E7A (4-9µ) from 0.24 to 0.30 to 0.50 µp, respectively. The two finer lots have permeabilities similar to the fine commercial porous tungsten.

Brazing infiltrates and closes the perimeter of the ionizer. One indicator of the overall volume infiltration is the gas permeability. By comparing permeability before and after brazing in Table 5-I, the braze area closure of all sized spherical powder ionizers except E7A-G-7 is 25-35%. This compares with a 45-50% closure for the powder lot (coarse unclassified) ionizers and 65-75% closure of the coarse commercial (PB) ionizers. Frequently the braze closure at the surface can be observed visually, especially after test when the flow of cesium through the porous area causes a difference in color. Sometimes the porous area remains shiny while the braze is dull (either white or dark); sometimes a deposit can be observed over the porous area, most likely due to improper shutdown procedure.

3720-Final

The diode sputtering pattern method used to measure active area was developed since May, 1963, and was used for all ionizers. This method gave active areas on commercial porous tungsten which checked with visual surface observation and cross section metallographic measurements. Recently a comparison of the sputtering pattern with ion microscope scanning data was made of a spherical powder ionizer, with good agreement between the two and also with the visual surface observation. Gas permeability appears to increase slightly during the ionization tests. This can only be due to opening of smeared pores on the front surface by the high temperature cesium environment. This again shows that the surface is smeared during the grinding closing the finer pores, since no leaks or microcracks have been observed. The only defects which appeared are melted spots from sparking which close small areas, thus also reducing permeability. The surface appears to lose the sharp grind marks; the center may have a somewhat etched appearance. In some cases sparking causes some spots on the ionizer surface to melt which are then sealed and should lower the permeability.

5.4 Cesium Permeability

Cesium permeability for all ionizers is given by the ion current density since they had low neutral fraction (shown in Fig. 5-5) as a function of cesium reservoir temperature for various ionizer samples. Comparison with nitrogen permeability is difficult because of the uncertainty of area. Mass permeability, prior to brazing, has a definite cross sectional area. The apparent nitrogen permeability after brazing indicates how much of this area was closed by braze, remembering that the actual open area varies from a smaller value on the upstream side to a larger (active) area at the front face. The cesium permeability in Fig. 5-5 is based on the larger active area at the front face. However, the only true permeability value is that taken prior to brazing. Hence this value should be compared with cesium permeability, which is based on an effective cross section area obtained from the apparent nitrogen permeability measurememt after brazing.

An increase in cesium permeability was observed for ionizer E3-G-3 during the five days of testing. The change was about 30 percent at low flow rates (2-3 ma/cm^2) to 75 percent at high flow rates (20-30 ma/cm^2). This change must be responsible for the poor correlation between initial gas permeability and cesium permeability taken at an arbitrary time during the test.

The decrease of cesium permeability with ionizer temperature is small (see Fig. 5-6). With the difficulty of comparison in mind, note that the finest structures had the lowest nitrogen permeability and the highest cesium permeability.
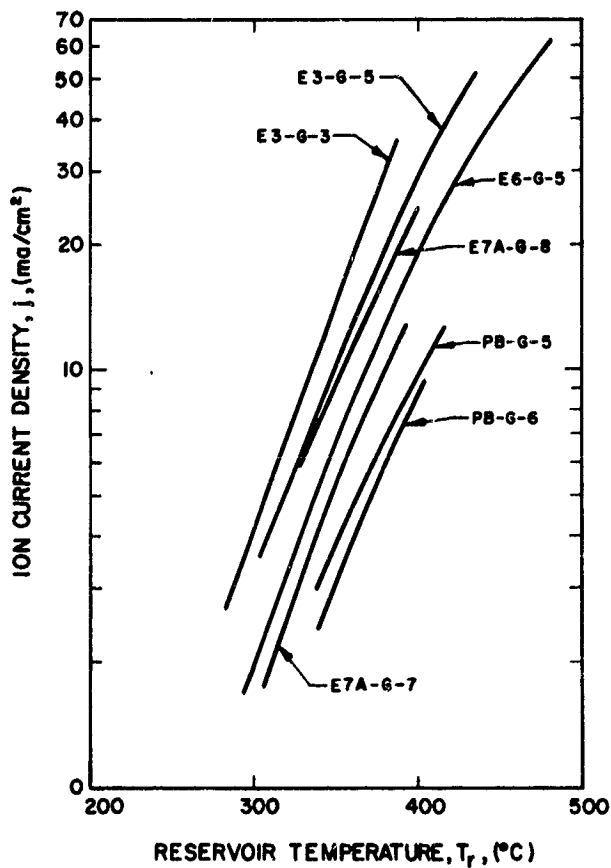
3720-Final

FIG. 5-5

CESIUM PERMEABILITY VS
RESERVOIR TEMPERATURE
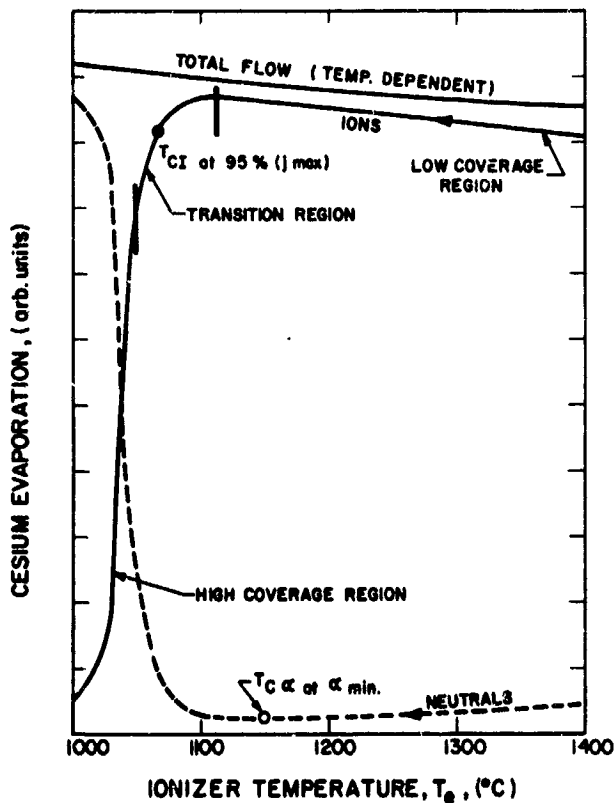(T_r) FOR POROUS IONIZERS

FIG. 5-6

ION CURRENT, NEUTRAL EFFLUX
AND TOTAL FLOW VS IONIZER
TEMPERATURE FOR POROUS
TUNGSTEN

5.5 Ion Current Density, Neutral Fraction and Critical Temperatures

The most popular measurement of surface ionization is the ion current density as a function of ionizer temperature for various cesium flow rates. A set of typical curves for solid tungsten, as measured by Langmuir[7], is shown in Fig. 5-7 to define the various regions of operation. These data were usually taken with increasing temperatures. In the high coverage region the rise is exponential. As the temperature increases to the so-called critical temperature (which is a function of the cesium flow rate), the ion current discontinuously rises by more than a decade as the surface becomes clean of cesium. At high temperature the cesium coverage is low, and for high work function surfaces the ionization is so nearly 100% that it appears essentially constant. When the ion current is measured by decreasing the surface temperature, the discontinuity occurs at a somewhat lower temperature, as indicated by hypothetical curves in Fig. 5-7. This is the lower critical temperature while the previous one was the upper critical temperature. The effect is usually called a hysteresis. The upper critical temperature is more reproducible and, for this reason, Langmuir measured only the upper T_c.

The breaking points of either T_c lie on a straight line in a log j vs 1/T plot, as shown in Fig. 5-7. This upper critical temperature line, extrapolated from the experimental ion current data given in Fig. 5-7, was used as a reference line in graphs of previous reports. The experimental data up to about 2 ma/cm^2 gave an empirical equation

$$\log_{10} \mu a = 27.791 - 14350/T_c$$

where μ_a is the rate of cesium atom incidence, which is equal to rate of cesium ion evaporation in at. cm^{-2} sec^{-1}. This line is shown in Fig. 5-8.

---

7. Taylor, J. B. and Langmuir, I. R., "The Evaporation of Atoms, Ions and Electrons from Caesium Films on Tungsten", Phys. Rev., 44, 423, (1933).
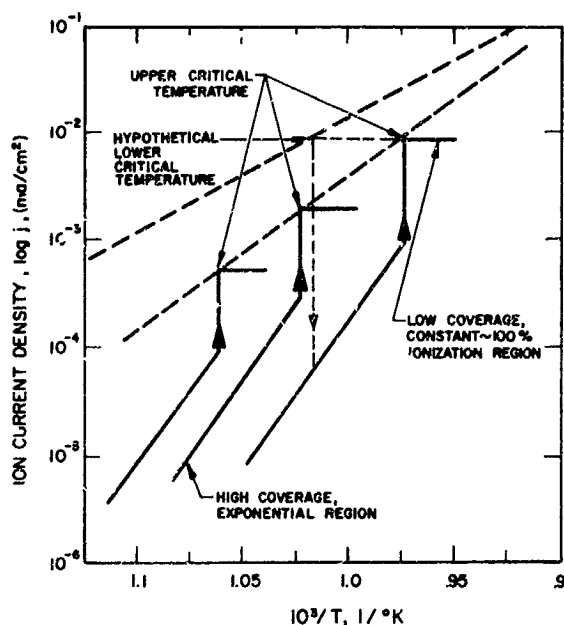
FIG. 5-7

DEFINITIONS OF SURFACE
IONIZATION REGIONS FOR ION
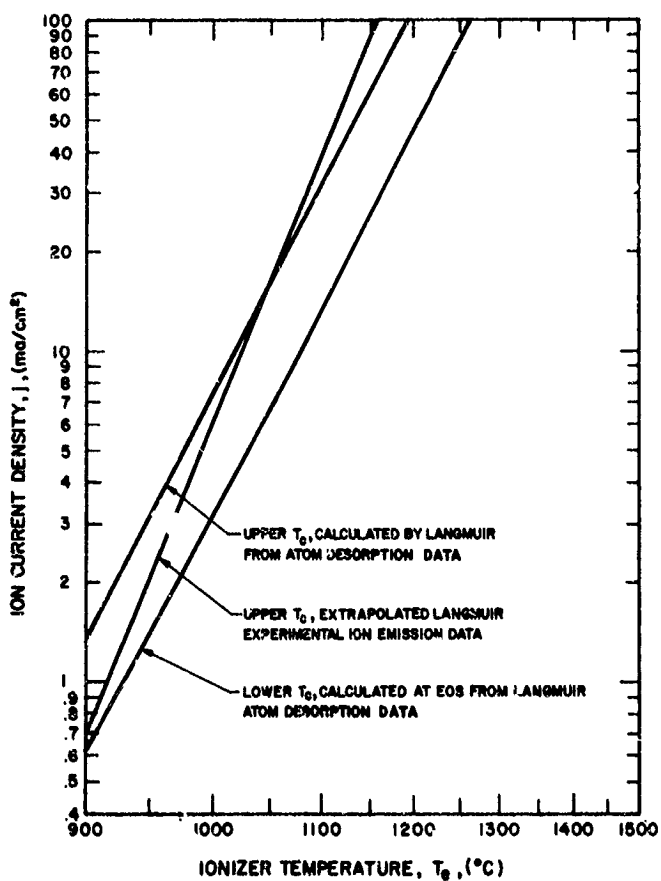CURRENT-IONIZER TEMPERATURE
CURVES FOR SOLID TUNGSTEN

FIG. 5-8

CRITICAL TEMPERATURE CURVES
FOR CESIUM IONIZATION ON SOLID
TUNGSTEN

It does not agree with the upper T_c data, calculated by Langmuir[8] from atom desorption data in the same paper which resulted in the equation

$$\log_{10} \mu a = 25.66 - 11500/T_c \quad .$$

For comparison with porous ionizers, we need the lower T_c, which can be obtained from atom desorption data and is very nearly represented by

$$\log_{10} \mu a = 24.6549 - 10730/T_c \quad .$$

The more accurate data are plotted in Fig. 5-8, which data will be used for comparison. Note the inconsistency of these Langmuir data because the lower T_c is higher than the upper T_c. The latter are believed to be in error.

For the porous ionizer the typical "ion current vs temperature" curve is more like that in Fig. 5-6, which curve is usually taken with decreasing temperature. The low coverage region is most likely no longer constant because of a change in ionization efficiency and ionizer permeability with ionizer temperature. Instead of a discontinuity, there is a transition region characterized by a large change in the slope.

There are sometimes two lower "critical temperatures" - one, T_{CI}, defined as the temperature at which the ion current has declined by 5%, (chosen as 2X the minimum detectable current change) the other - $T_{C\alpha}$, defined as the temperature corresponding to minimum neutral fraction. The $T_{C\alpha}$ point may be closer to the upper T_c. The higher the current density and the cleaner the tungsten surface, the smaller the difference between upper and lower T_c. It has not been established which temperature is best for optimum ion engine performance, but it is in the relatively small range between the lower T_{CI} and upper $T_{C\alpha}$. The sum of the

---

8. I. R. Langmuir and J. B. Taylor, "Vapor Pressure of Caesium by the Positive Ion Method", Phys. Rev., 51, 753, (1937).

3720-Final

ion and equivalent atom currents shows that the total flow rate decreases about 3.5 percent/100°C. A typical neutral fraction curve is shown in Fig. 5-6, another set in Fig. 5-9. These curves are theoretically described by the Saha-Langmuir equation which, for constant work function, is also plotted in Figs. 5-9 and 5-10. Experimental curves show a similar decrease with decreasing temperature only for ionizers having very low neutral fractions (below 1 percent). There is a region in which the work function starts to decrease, due to cesium adsorption, and the α curves exhibit a flat region. For some ionizers this flat region extends over several hundred degrees (see Fig. 5-11). At higher flow rates giving higher neutral fraction, the curves may have no minimum below 1400°C.

For all ion current and neutral fraction measurements, the appropriate voltage must be applied to insure emission-limited operation. Current-voltage characteristics in Fig. 5-12 show the required voltage for any ion current density. For some cases, the space-charge limited portion follows the 3/2 power law, while in many other experiments the slope for this region is much higher at first, then subsequently much lower. This effect is believed to be due to the accelerator and not to the ionizer.

5.6 Performance of 1-4μ Spherical Powder Ionizer

As evident from the photomicrographs and mechanical parameters shown in Table 5-I, this is the finest, most uniform structure produced to date. The 80 percent dense 1-4μ ionizers have a smaller nitrogen permeability than all other structures tested on this contract. The nitrogen permeability is about equal to that of the fine commercial tungsten tested earlier[9]. The average pore diameter, as calculated

---

9. G. Kuskevics and B. L. Thompson, "Comparison of Commercial Spherical Powder and Wire Bundle Tungsten Ionizers", AIAA Jour. 2, No. 2, 284-294, (1964)
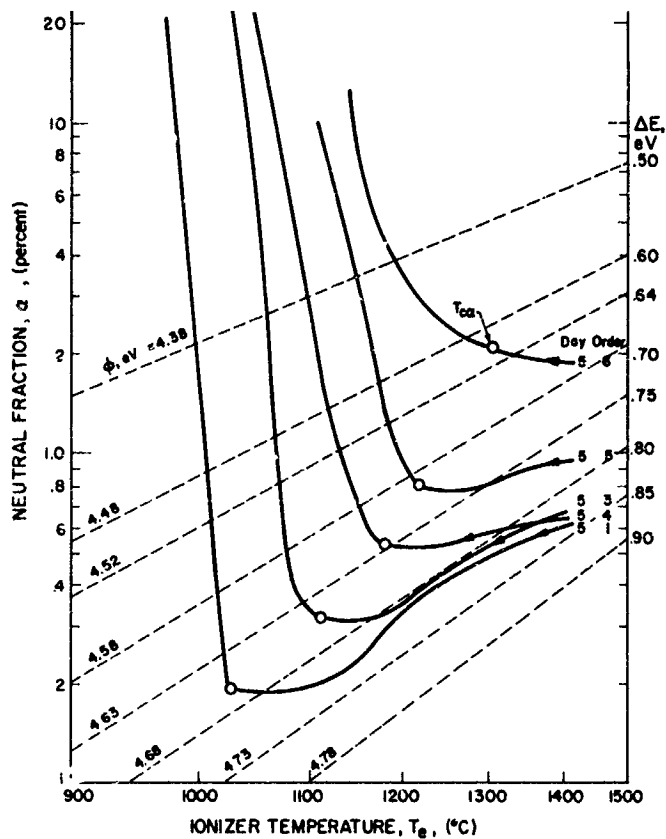
FIG. 5-9   NEUTRAL FRACTION VS IONIZER
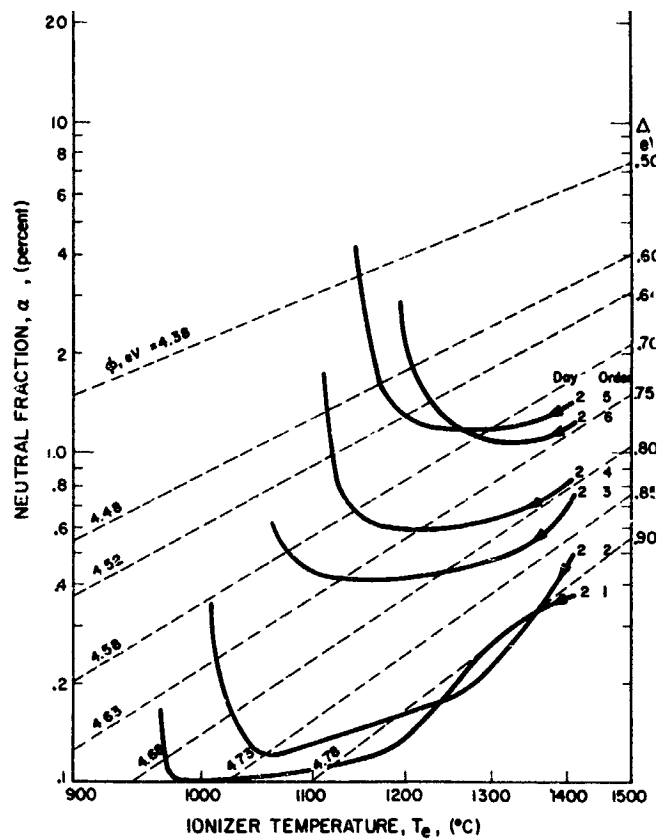   TEMPERATURE FOR E3-G-3,
            1-4μ IONIZER

FIG. 5-10   NEUTRAL FRACTION VS IONIZER
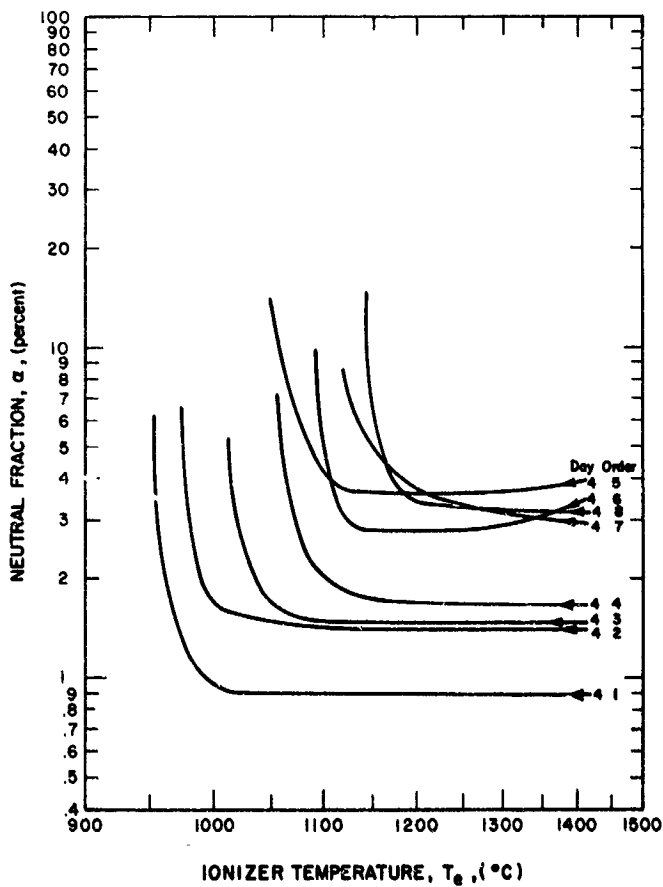   TEMPERATURE FOR E3-G-5,
            1-4μ IONIZER

FIG. 5-11

NEUTRAL FRACTION VS IONIZER
TEMPERATURE FOR E6-G-5, 3-6μ
IONIZER

from pore counts, was the lowest - 2.50μ and the pore density the highest - 4.01×10^6 pores/cm^2.

Upon brazing, these ionizers show the lowest reduction of nitrogen permeability (25-35 percent) which implies the lowest braze infiltration. Besides being the finest, these would be expected to be the most uniform ionizers.

These finest spherical powder ionizers had the highest cesium permeability, which suggests that the mechanism of cesium flow through the ionizer is different from that of nitrogen.

The E3-G-3 ionizer was operated for four days in a vacuum of $(1-3) \times 10^{-6}$ torr. This pressure level was not as low as standard due to a small leak. The final and most complete performance data were measured on the fifth day under 10^{-7} torr, as shown in Figs. 5-10, 5-13, 5-14, and 5-15.

The ion current density curve 51 in Fig. 5-13 and the neutral fraction curve 51 in Fig. 5-9 were measured simultaneously. The active area, measured by diode sputtering pattern, was 0.154 cm^2. After the second day there were three melted spots on the surface which reduced the area to 0.143 cm^2. Even without this correction, a maximum ion current density of 55 ma/cm^2 was reached. Stable operation with little sparking could be maintained up to 40 ma/cm^2. These limits are more contingent on the accelerator than on the ionizer, except that they depend indirectly upon the neutral fraction. The extended transition region at high ion current densities is due to large electron back currents, which locally heat the ionizer surface and produce non-uniform temperature. The solid points in Fig. 5-13 give the lower T_{CI}, the open circles the lower $T_{C\alpha}$ corresponding to minimum α in Fig. 5-9. Note that the T_{CI} points are lower than the corresponding Langmuir data for solid tungsten. Figure 5-9 represents the first ionizer to show such definite decrease of neutral fraction, in agreement with the Saha-Langmuir equation for solid tungsten
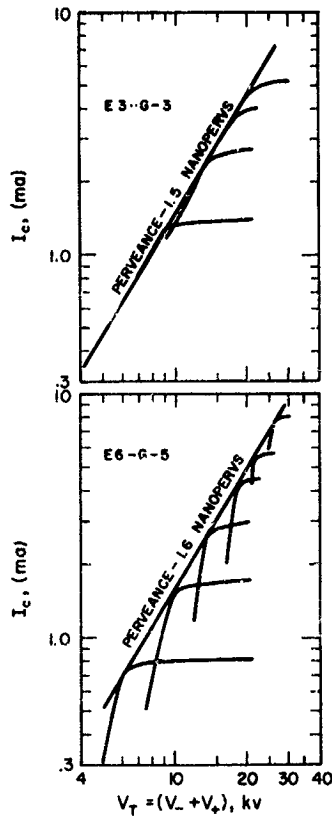
$$\alpha = 1 + 2 \times 10^{-5040\Delta E/T} .$$

FIG. 5-12

TYPICAL CURRENT - VOLTAGE
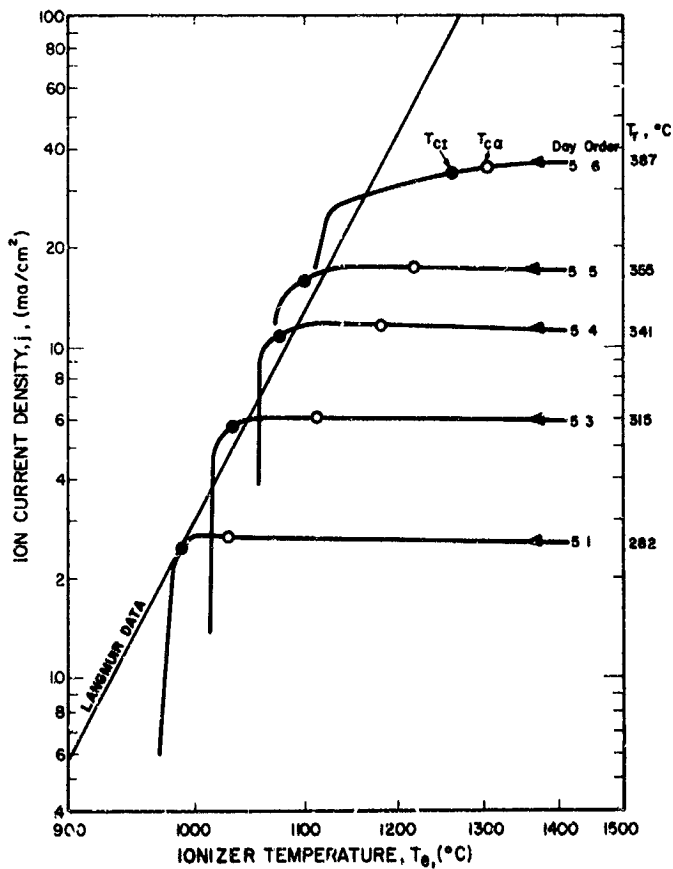CHARACTERISTICS FOR TWO
EXPERIMENTS

FIG. 5-13

ION CURRENT DENSITY VS
IONIZER TEMPERATURE FOR
E3-G-3, 1-4μ IONIZER

Theoretical curves for different work functions, shown in Fig. 5-9, give a work function for porous tungsten of between 4.65 and 4.70, which is somewhat higher than the preferred 4.5x handbook value.

The neutral fractions were generally very low and their minimum temperatures, shown by circles, were 60-120° above the T_{CI} points. These points form a straight line in Fig. 5-9, as well as in Fig. 5-13.

A new type of graph, obtained by combining data of Figs. 5-13 and 5-9, is given in Fig. 5-14. These curves show that for a given neutral fraction, dictated by engine life, there is a maximum ion current density at a given ionizer temperature.

Graphs in Fig. 5-15 show the increase of neutral fraction with ion current density.

A second ionizer of 1-4μ was tested under AF contract, yielding the similar set of data shown in Figs. 5-16, 5-10, 5-17, 5-18. The critical temperatures and neutral fractions were somewhat lower.

5.7 Performance of 3-6μ Spherical Powder Ionizer

This ionizer structure was definitely coarser than the 1-4μ structure. Average nitrogen permeability and pore size were about 30 percent higher, pore density and cesium permeability were similarly lower.

Final data on the fourth day of operation is shown in Fig. 5-19, 5-11, 5-20, and 5-21. The T_{CI} points are among the lowest, being 50-100° below the Langmuir lower T_c. The neutral fractions were not as small at low j levels as those of the 1-4μ ionizers, and did not exhibit the decline with temperature. The highest ion current density of 60 ma/cm^2 was reached with a neutral fraction of only 3 percent. Note that the slope in Fig. 5-21 is much lower than that of Figs. 5-15 and 5-18.

5.8 Performance of 4-8μ Spherical Powder Ionizer

This was the coarsest of the sized powder ionizer structures and it had a high nitrogen permeability. Two samples were tested because the first one accidentally was deeply infiltrated during brazing. Typical data are shown in Figs. 5-22, 5-23, 5-24, and 5-25.

3720-Final

FIG. 5-14 ION CURRENT DENSITY VS
IONIZER TEMPERATURE FOR
CONSTANT NEUTRAL EFFLUX
FOR E3-G-3, 1-4μ IONIZER

FIG. 5-15 NEUTRAL FRACTION VS ION
CURRENT DENSITY FOR
E3-G-3, 1-4μ IONIZER

FIG. 5-16

ION CURRENT DENSITY VS IONIZER
TEMPERATURE FOR E3-G-5, 1-4μ
IONIZER

FIG. 5-17   ION CURRENT DENSITY VS
            IONIZER TEMPERATURE FOR
            CONSTANT NEUTRAL EFFLUX
            FOR E3-G-5, 1-4μ IONIZER

FIG. 5-18   NEUTRAL FRACTION VS ION
            CURRENT DENSITY FOR E3-G-5,
            1-4μ IONIZER

FIG. 5-19

ION CURRENT DENSITY VS IONIZER
TEMPERATURE (T_e) FOR E6-G-5,
3-6μ IONIZER

FIG. 5-20   ION CURRENT DENSITY VS
IONIZER TEMPERATURE FOR
CONSTANT NEUTRAL EFFLUX
FOR E6-G-5, 3-6μ IONIZER

FIG. 5-21   NEUTRAL FRACTION VS ION
CURRENT DENSITY FOR
E6-G-5, 3-6μ IONIZER

FIG. 5-22

ION CURRENT DENSITY VS IONIZER
TEMPERATURE FOR E7A-G-8, 4-8μ
IONIZER

FIG. 5-23 NEUTRAL FRACTION VS IONIZER
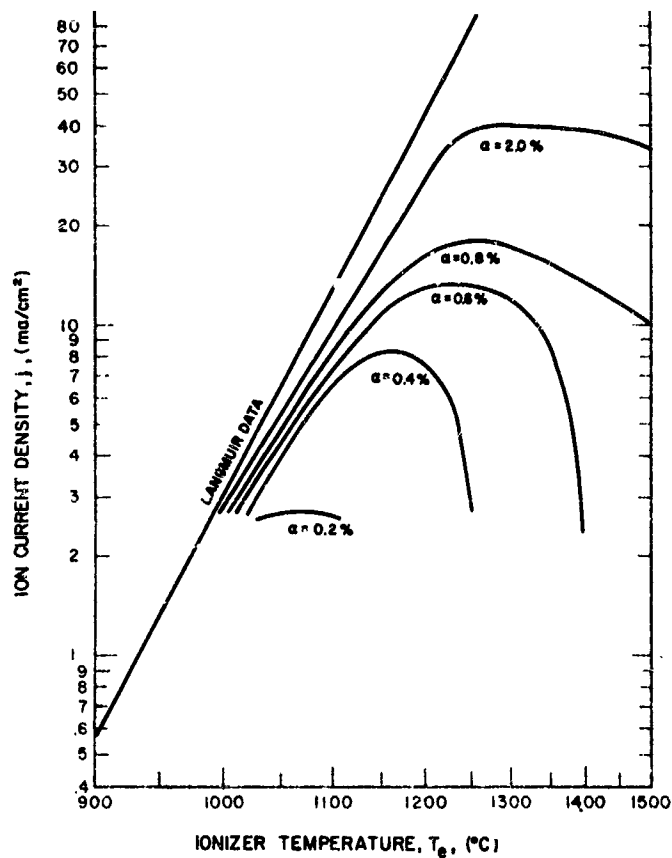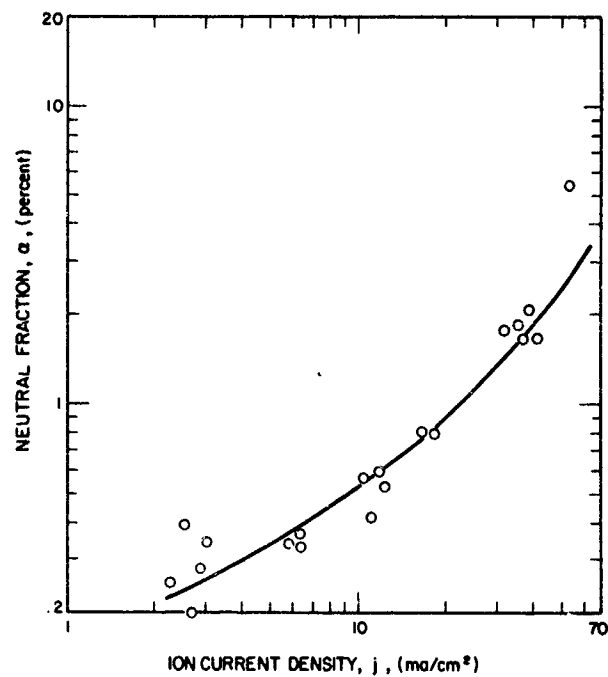TEMPERATURE FOR E7A-G-8,
4-8μ IONIZER

FIG. 5-24 ION CURRENT DENSITY VS
IONIZER TEMPERATURE FOR
CONSTANT NEUTRAL EFFLUX
FOR E7A-G-8, 4-8μ IONIZER
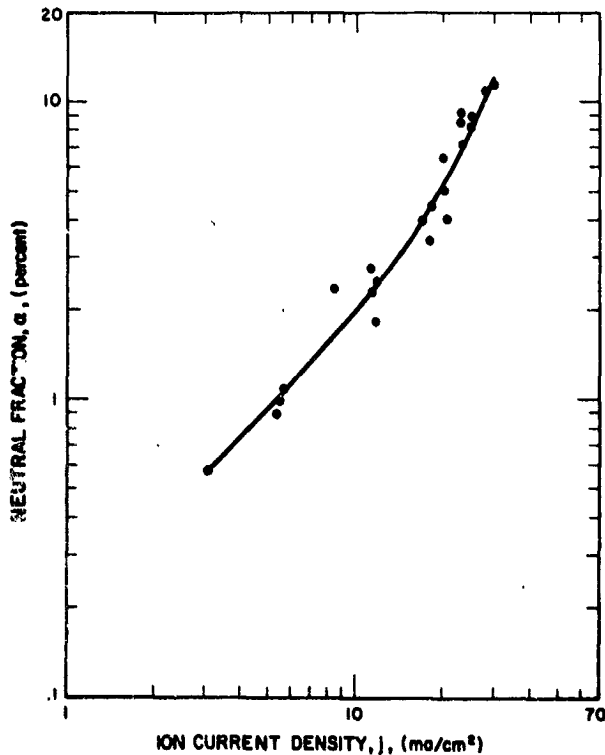
FIG. 5-25

NEUTRAL FRACTION VS ION
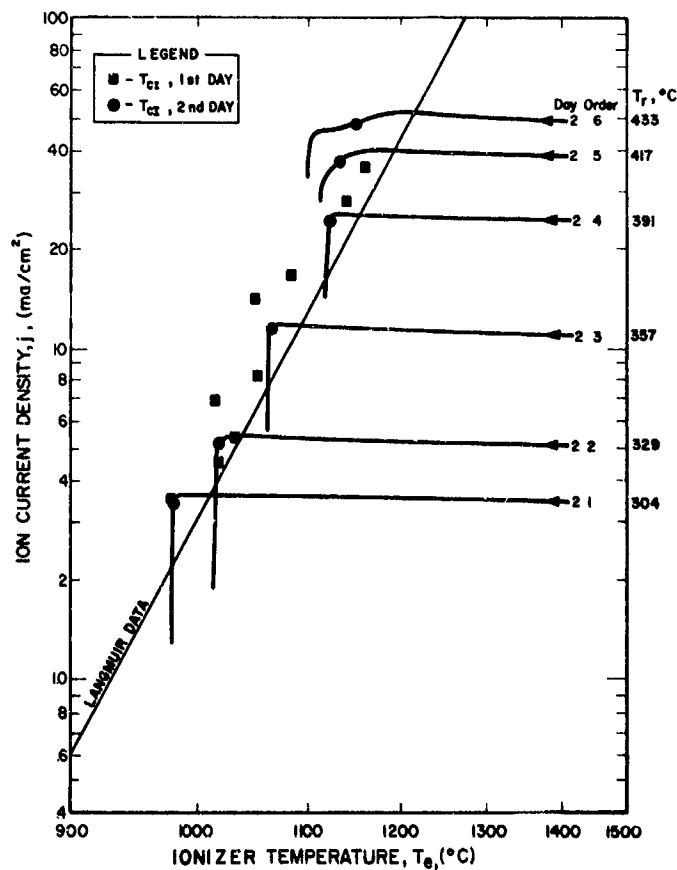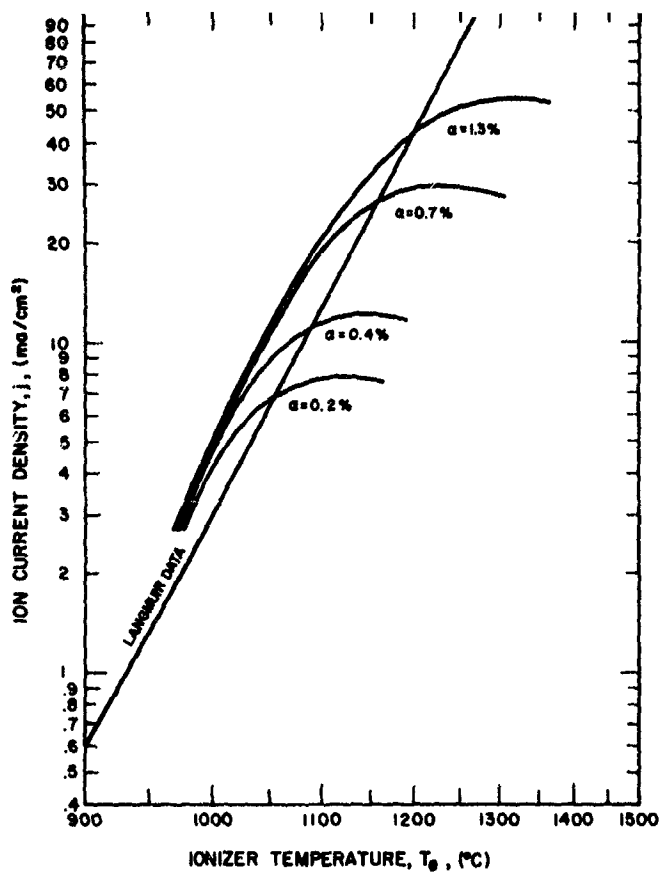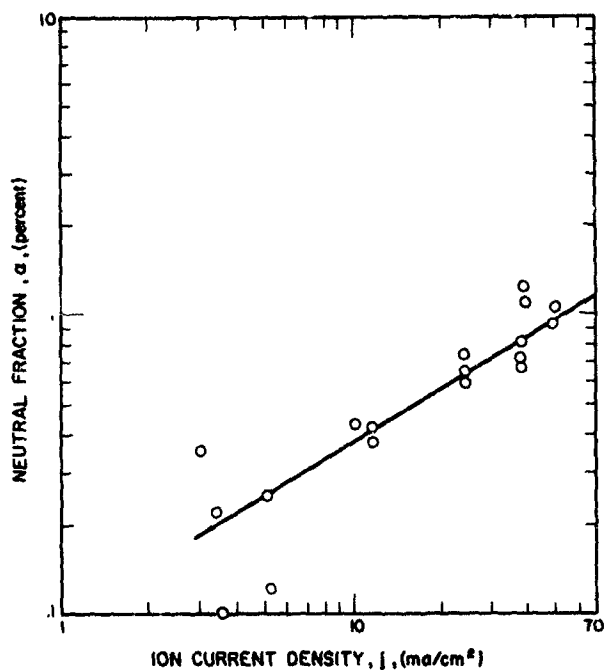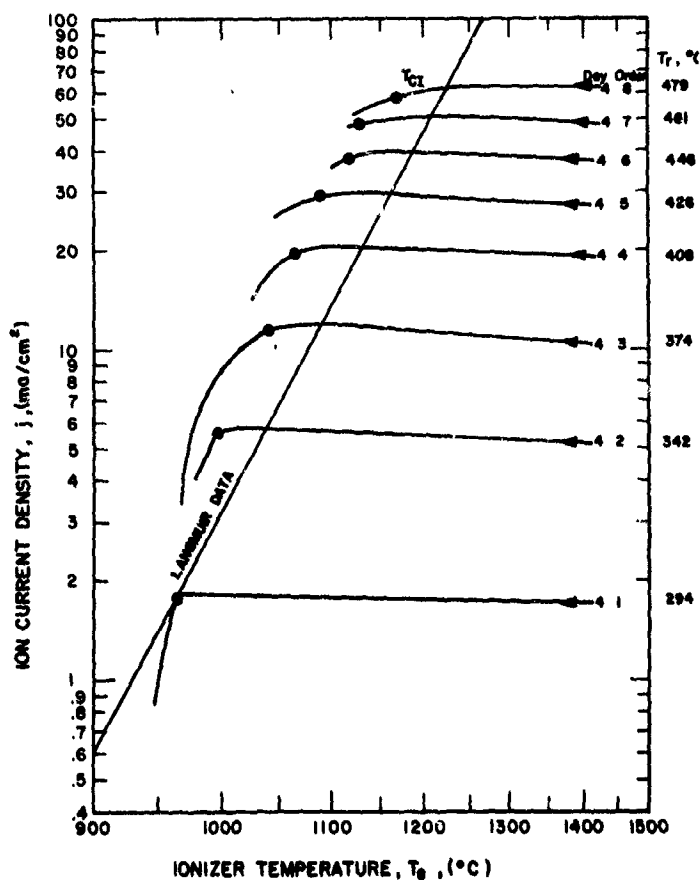CURRENT DENSITY FOR E7A-G-8,
4-8μ IONIZER

5.9 Performance of Coarse (Commercial) H_2-Reduced Powder Ionizers

Because the first coarse (Philips Mod. B) ionizer had poorer performance than the previously-tested fine commercial ionizers (which come in small sizes only), two ionizers were tested. A set of data for one of these ionizers is given in Figs. 5-26, 5-27, 5-28, and 5-29. The other ionizer had identical performance, and, therefore, data curves for it have not been included. Note that the two _ curves followed the theoretical slopes above $1200^{\circ}C$.

5.10 Comparison of Performance of Sized Spherical Powder and Philips Mod. B Structures

The lower ion current critical temperatures, T_{CI}, in Fig. 5-30 for the two types of finer structures, are below the Langmuir data for solid tungsten. The coarsest sized spherical powder and the coarse commercial ionizer critical temperatures are about 100° higher. This depends somewhat on the residual pressure, which was in the low 10^{-7} range for most of these tests.

A more meaningful comparison can be obtained from Fig. 5-31, which demonstrates the amazing fact that only 1 percent of neutrals was detected at 50 ma/cm^2 (of ions) for E-3-G-5. For all sized 1-4 and 3-6μ structures, α was below 3 percent. Predominance of the data, shown by the curves of Fig. 5-31, indicate that the slope of the E6-G-5 curve is too small. A probable explanation is that this ionizer was not aged sufficiently when the neutral fraction measurements were made at low current densities. All fine (sized spherical powder) structures achieved ion current densities of 50 ma/cm^2.

In conclusion, the fine sized powder ionizers have demonstrated a far better performance than spherical powder or commercial ionizers have previously shown.

3720-Final
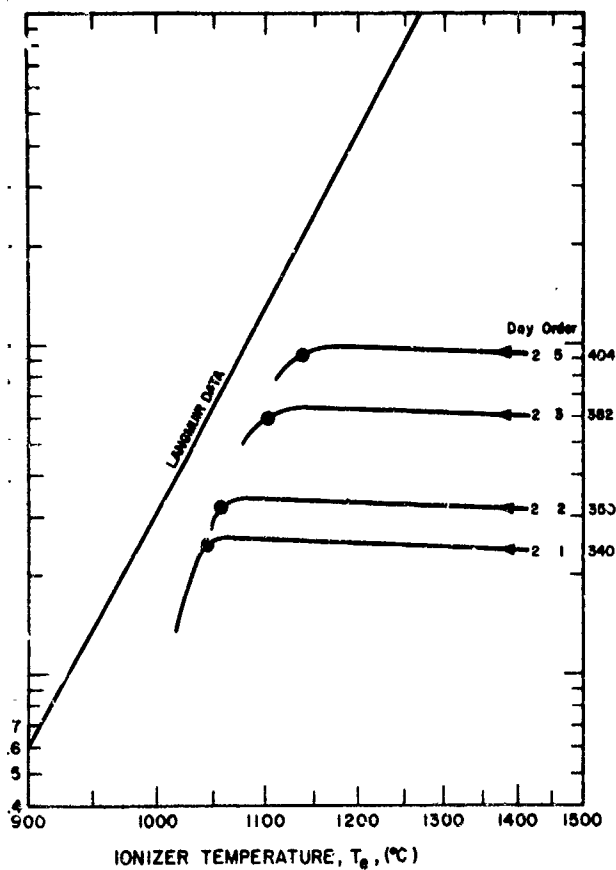
FIG. 5-26   ION CURRENT DENSITY VS
            IONIZER TEMPERATURE FOR
            PB-G-6 IONIZER
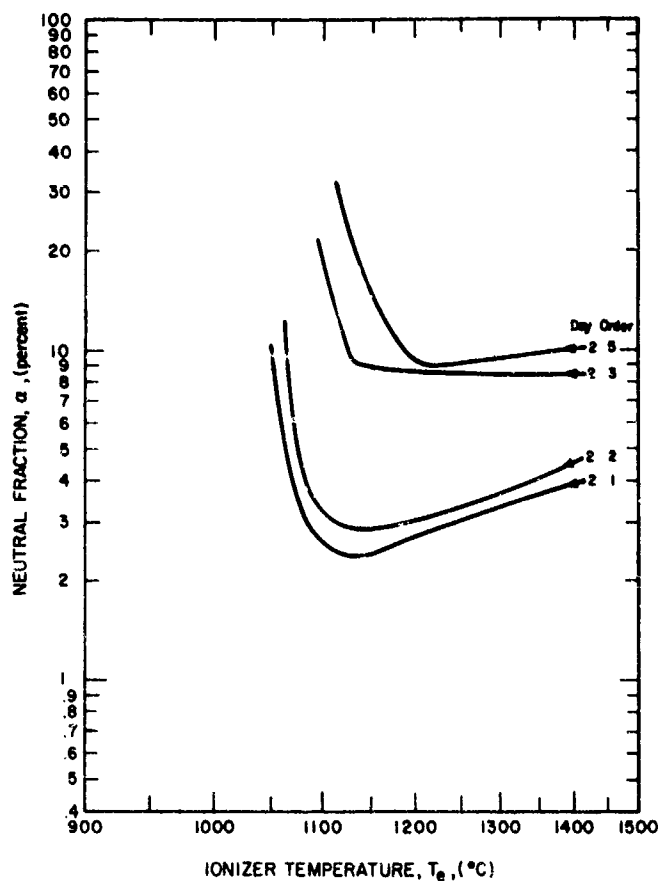
FIG. 5-27   NEUTRAL FRACTION VS
            IONIZER TEMPERATURE FOR
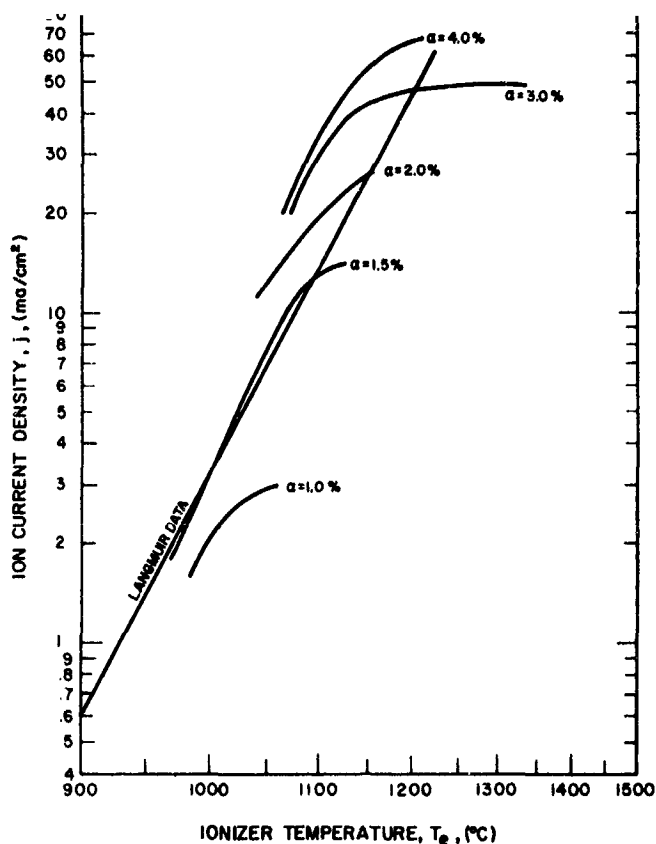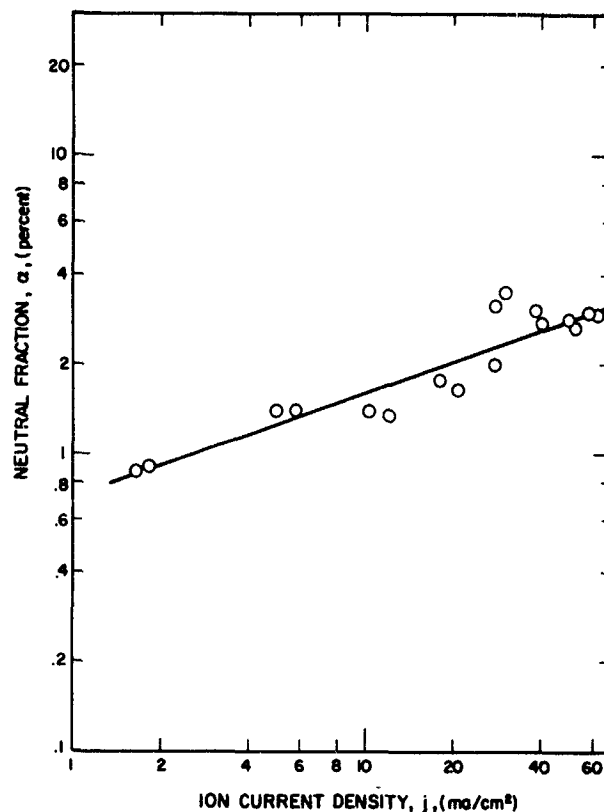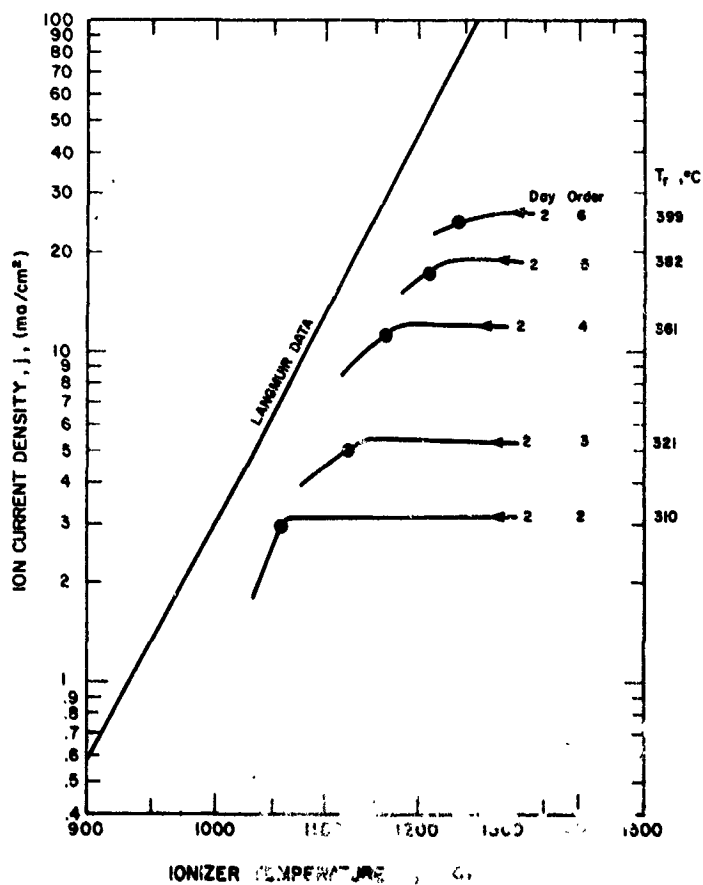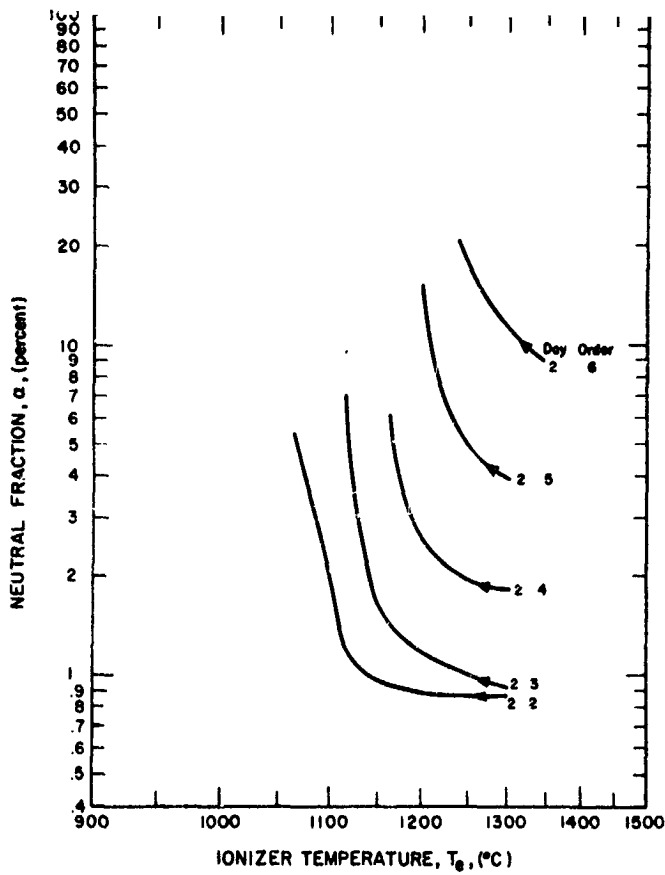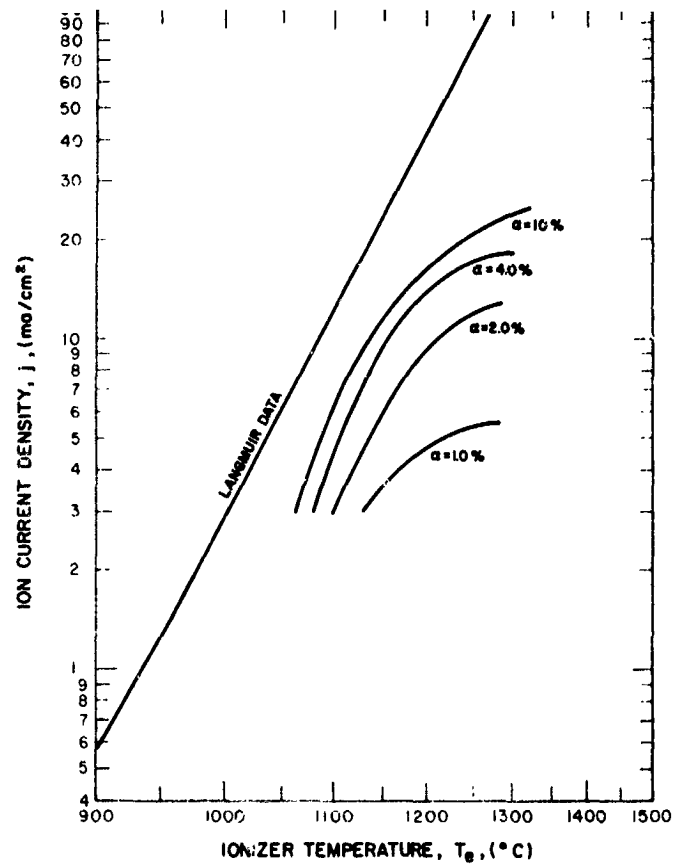   PB-G-6 IONIZER
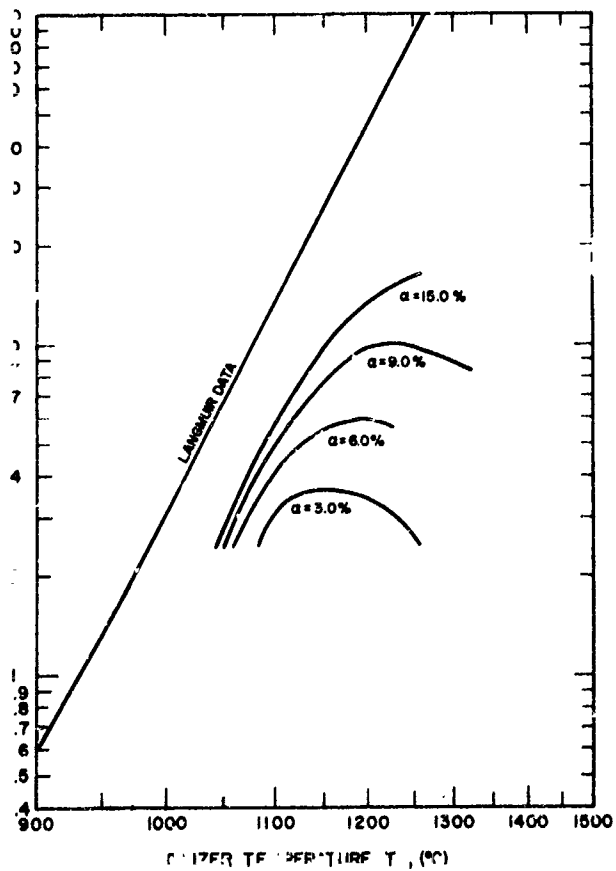
FIG. 5-28

ION CURRENT DENSITY VS
IONIZER TEMPERATURE (T_e) FOR
CONSTANT NEUTRAL EFFLUX FOR
PB-G-6 IONIZER
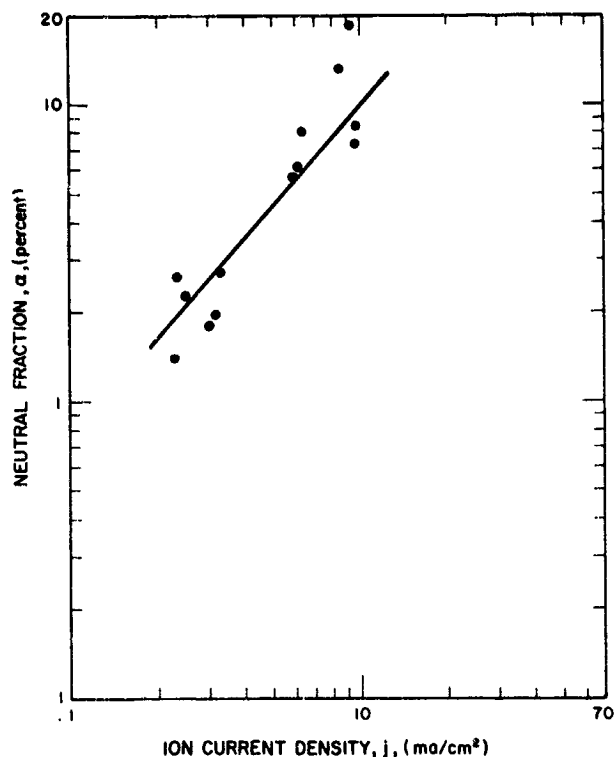
FIG. 5-29 NEUTRAL FRACTION VS
ION CURRENT DENSITY
FOR PB-G-6 IONIZER
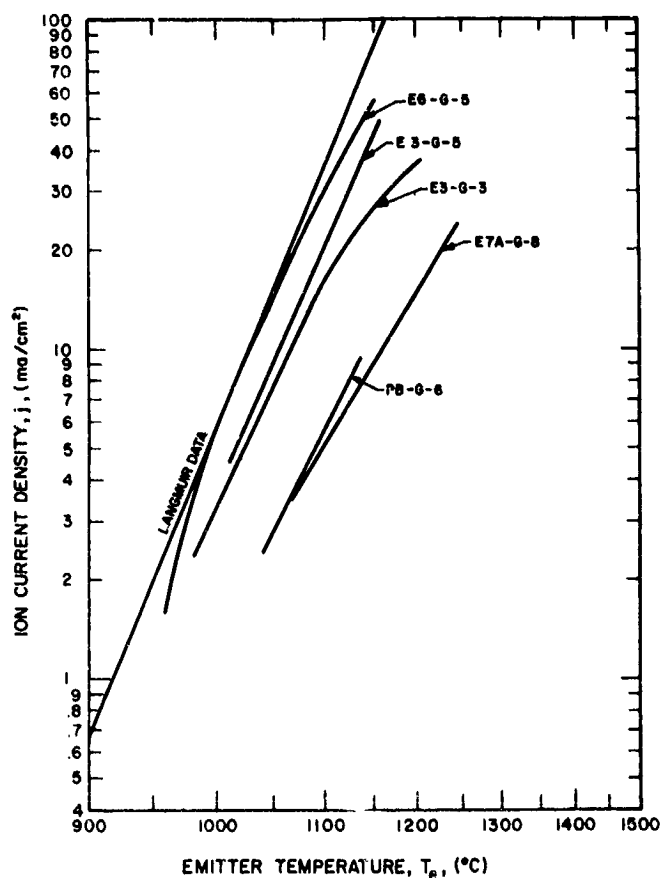
FIG. 5-30 CCMPARISON OF CRITICAL
TEMPERATURES FOR POROUS
IONIZER SAMPLES
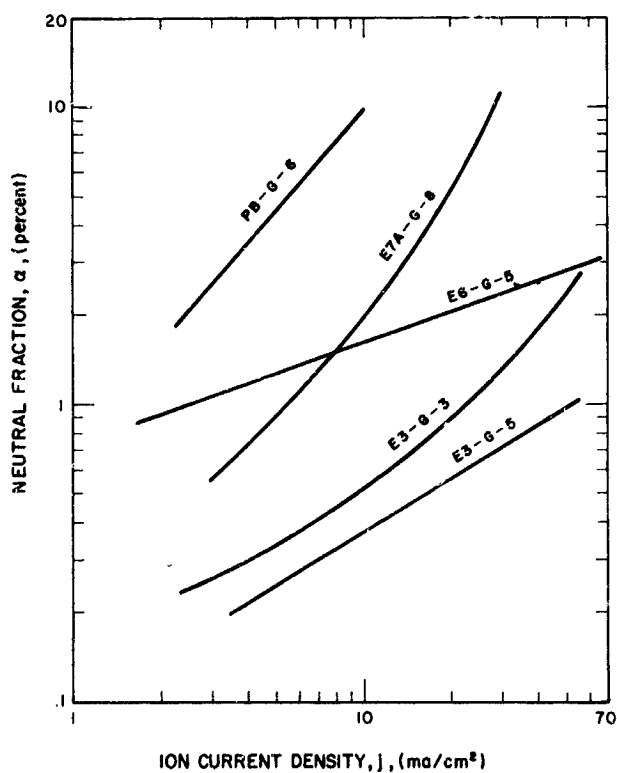
FIG. 5-31

COMPARISON OF NEUTRAL FRACTION
VS IONIZER CURRENT DENSITY FOR
POROUS IONIZER SAMPLES

6. EFFECT OF Ta AND Cr ON THE SINTERING AND STRUCTURE OF SPHERICAL TUNGSTEN POWDER

Toward the objective of increasing the thermal stability of spherical tungsten ionizers, three series of alloy compacts were prepared and evaluated with respect to sintering rate and microstructure. Selection of tantalum as a diffusion retarder was based on work of Braun et al[1] and on results obtained in the previous contract[2]. While it was initially hoped to obtain full pore characterization on the tungsten alloys selected, as well as an indication of ionization performance, this was prevented by infiltration difficulties (to be described subsequently).

6.1 Constituent Powders and Fabrication Method

Spherical powder fractions E7A and E4 (refer to Sections 2.2.1 and 2.4 for size and purity, respectively) were selected as the base powders for the alloy compacts. Chromium powder from Alloy Metal Powder, Inc. of Davenport, Iowa, was used. Its specified purity was 99.85 percent, min., with 200 ppm O, 20 ppm N, and 1280 ppm of other residuals. Tantalum powder, SGH Grade from National Research Corp. of Newton, Massachusetts, was also used. A typical analysis of this material indicated 99.98+ percent spectrographic purity, plus 1800 ppm O, 20 ppm N and 44 ppm C. Both the Cr and Ta powders used were the purest that could be obtained in the fine particle size required.

The as-received tantalum and chromium powders were classified in the Sharples K8 unit and analyzed by Micromerograph. Complete size

---

1. Braun, H., Kieffer, R., and Sedaltschek, K., "Contributions to the Technology of Tantalum-Tungsten Alloys", Chapter 19, Plansee Proceedings, 1958.

2. Electro-Optical Systems, Inc. Report 2150-Final on NAS 8-2547, pages 3-32, 33 and 34, May 1963.

analyses data for all particle fractions obtained are listed in Table 6-I. Tantalum fractions BF (predominantly 1-3μ) and EF (4-9μ), and chromium fraction 1F (3-8μ) were selected for use by mutual agreement with the NASA Technical Manager.

Fabrication of the alloy compacts was performed in a manner similar to that used for unalloyed compacts, with special emphasis on thorough blending. Mixtures of W-4 A/o Cr, W-10, 15 and 20 A/o Ta were calculated. After accurately weighing the component powder, they were blended in sample jars at a tumbling speed judged to provide the optimum lap-over action. For all compacts, except those of Series No. 1, 3/16"-dia. ball bearings were included in the blending jars to provide improved mixing action. Blending time for all powder mixtures was 3 hours or greater. All alloy compacts were pressed hydrostatically at 59000 psi in the standard barrel shape and sintered at 2000 or 2200°C under 5×10^{-5} torr pressure.

6.2 Alloy Series No. 1

The E7A (4-8μ) spherical tungsten powder base was used for the first alloy series. Samples of W-4 A/o Cr, W-10, 15 and 20 A/o Ta was sintered at 2000°C for incremental times totaling 240 minutes. In addition to having very poor green strength, the surface appearance of the sintered samples was not uniform, indicating inhomogeneity of sintered density. The densities were determined, nonetheless, and are reported in Table 6-II. Trends indicated here are as follows:

(a) Densification rate of W-4 Cr is higher than that of the unalloyed base sample.

(b) All tantalum additions retarded densification rate, the higher tantalum additions being the more retarding.

(c) The coarser (3-8μ) tantalum additive has a greater retarding effect on sintering than does the finer (1-3μ) tantalum (for equal percentage added).

TABLE 6-I

Particle Size Distribution Data Obtained by Micromerograph Analyses
for Tantalum* and Chromium** Powder Fractions (Powders separated in Sharples K-8 Superclassifier)

Sharples Run No.	% by	1-2	2-3	3-4	4-5	5-6	6-7	7-8	8-9	9-10	10-11	11-12	12-13	13-14	14-15	15-20	20-25	25-30	30-35	35-37	Remarks
								Tantalum Powder*													
BF	Wt.	27.5	36.3	23.5	9.0	3.7															BF used in the W-10, 15, and 27 Ta Alloys
	No.	73.14	20.85	4.92	0.89	0.20															
CF	Wt.	3.5	9.5	20.7	26.4	21.0	10.1	5.3	2.7	0.8											
	No.	39.91	23.40	18.58	11.15	4.86	1.42	0.48	0.17	0.04											
DF	Wt.		1.4	6.2	17.0	29.8	20.6	12.2	6.3	3.5	2.2	0.8									
	No.		12.44	20.07	25.89	24.86	10.41	4.01	1.42	0.57	0.26	0.07									
EF	Wt.		Nil	1.9	5.3	18.0	24.5	20.5	13.5	8.0	5.5	2.2	0.6								EF used in only the W-10 Ta Alloy
	No.	Nil	Nil	11.47	15.06	28.01	23.10	12.58	5.69	2.42	1.23	0.37	0.08								
FF	Wt.		Nil	0.5	3.7	8.3	14.0	19.4	17.3	14.0	11.6	6.6	2.8	1.5	0.3						
	No.	Nil	Nil	4.48	15.61	19.18	19.60	17.68	10.83	6.28	3.85	1.67	0.55	0.23	0.04						
GF	Wt.		Nil	0.9	2.2	3.6	6.3	15.1	16.8	15.4	11.9	8.9	7.0	5.2	2.7	4.0					
	No.	Nil	Nil	10.80	12.42	11.13	11.80	18.41	14.07	9.24	5.29	3.01	1.84	1.09	0.46	0.47					
GHF	Wt.		Nil	Nil	1.4	3.2	5.5	13.1	13.4	13.3	12.2	10.8	8.4	6.7	4.3	7.7					
	No.	Nil	Nil	Nil	10.19	12.76	13.29	20.60	14.48	10.29	6.99	4.71	2.85	1.81	0.94	1.09					
								Chromium Powder**													
1F	Wt.		Nil	1.6	3.7	5.0	6.4	7.4	10.0	11.2	9.8	8.5	7.4	7.0	4.8	9.9	2.9	2.2	1.7	0.5	1F used in the W-4Cr Alloy
	No.	Nil	Nil	18.39	20.00	14.81	11.48	8.64	8.02	6.44	4.17	2.75	1.87	1.40	0.78	1.04	0.13	0.05	0.03	0.01	
2F	Wt.		Nil	Nil	2.1	3.1	4.0	5.6	6.6	7.7	8.2	8.4	8.7	8.1	7.7	19.9	4.3	2.7	2.1	0.8	
	No.	Nil	Nil	Nil	19.68	15.91	12.44	11.34	9.18	7.67	6.05	4.72	3.80	2.81	2.16	3.73	0.34	0.11	0.05	0.02	
3F	Wt.		Nil	Nil	Nil	1.2	2.0	3.0	3.9	5.0	6.5	8.1	10.1	10.5	9.0	27.4	7.3	3.1	2.1	0.8	
	No.	Nil	Nil	Nil	Nil	11.33	11.44	11.17	9.98	9.16	8.82	8.37	8.12	6.70	4.64	8.79	1.11	0.25	0.10	0.03	

Bracketed subtotals (No. %): BF 93.99; CF 81.89, 83.26; EF 90.22; FF 82.90; GF 67.83; GHF 71.32; 1F 73.32; 2F 68.55; 3F 61.90.

* Grade SGH Nat. Res. Lab. Tantalum of 99.79+ percent purity
** Alloy Metal Powder, Inc. Chromium of 99.85+ percent purity

TABLE 6-II
Sintering Rate Data for W-Ta and W-Cr Alloys
(Obtained for 2000 and 2200°C)

.gsten ase owder	Additive Metal	Lot	Sintering Time at 5×10^{-5} torr, minutes 0 (as pressed)	15	30	60	120	240
			Sintered at 2000°C					
37A (4-8µ)	Unalloyed		67.93	---	72.23	74.15	76.94	---
"	10 A/o Ta	BF (1-3µ)	71.93	68.25	70.30	72.35	73.14	74.20
"	15 A/o Ta	"	---*	62.51	67.13	68.56	69.14	70.05
"	20 A/o Ta	"	---*	60.20	62.88	65.18	65.45	66.42
"	10 A/o Ta	EF (3-8µ)	---*	61.98	66.14	67.61	68.56	69.46
"	4 A/o Cr	1F (3-7µ)	---*	70.72	74.60	76.67	77.42	79.06
			Sintered at 2200°C					
37A (4-8µ)	Unalloyed		69.38	---	78.76	81.97	84.72	---
37A	10 A/o Ta	BF (1-3µ)	72.30	68.51	69.35	70.88	72.46	74.99
"	15 A/o Ta	"	73.82	66.33	67.23	68.72	70.05	72.12
"	20 A/o Ta	"	73.81	62.99	64.01	65.02	66.36	67.81
"	10 A/o Ta	EF (3-8µ)	69.56	65.24	66.03	67.51	68.98	71.83

Coherence of pressed samples too low for "green" density measurements.

The last trend appeared to be incorrect until it was again noted on the 2nd alloy series, sintered at 2200°C.

The density samples were immersed in pure copper at ~1300°C for 30 minutes under vacuum. Subsequent metallographic examination indicated no infiltration of W-4 Cr and relatively shallow infiltration of the W-Ta samples. Photomicrographs of the alloys are shown in Fig. 6-1, excluding the 10 A/o Ta (3-8μ) alloy which was particularly inhomogeneous. The relatively large pores of this sample series made metallographic polishing quite difficult, since the soft copper of the pores polishes in relief. However, Fig. 6-1 does show that agglomeration of the particles and width of the diffusion bridges both decrease with increasing tantalum. The W-4 Cr structure at the lower right contains no copper infiltrant. Having been sintered at 2000°C, with melting of the chromium additive, large voids are apparent. It is believed that the chromium liquation sealed the pore channels and excluded the infiltrant.

Based on the evidence that W-4 Cr, (1) sintered as rapidly as unalloyed tungsten, (2) could not be infiltrated, and (3) would require very long sintering to reach 80 percent density at below the melting point of Cr, no further study of this composition was indicated to be advisable. Therefore, efforts were concentrated on the W-Ta compositions.

6.3 Alloy Series No. 2

For the second W-Ta series, the same 4-8μ tungsten powder (E7A) was used. In preparing this series, precautions of vacuum drying the preweighed mixtures and of incorporating ball bearings in the blending jars were taken. Subsequent examination of the structures indicated that homogeneity was thereby increased. This sample series was sintered for a total of 4 hours at 2200°C to achieve densities closer to the 80 percent target. However, as the data of Table 6-II show, the 4 hour - 2200° sinter yielded densities only slightly higher than the 2000° sinter.
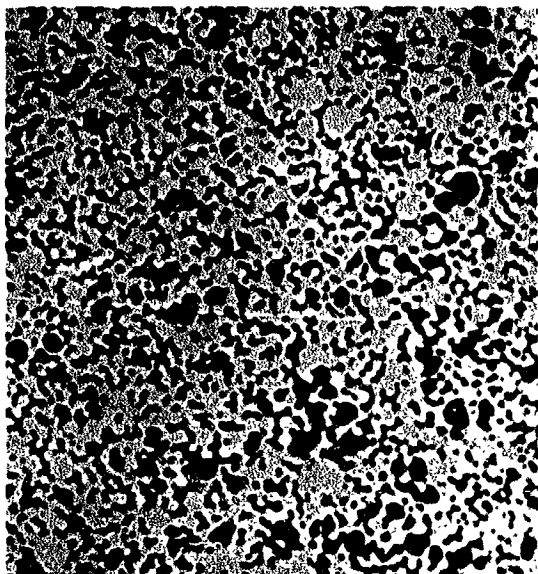
NEG. 1226   DENSITY = 74.20%

W-10 A/o Ta
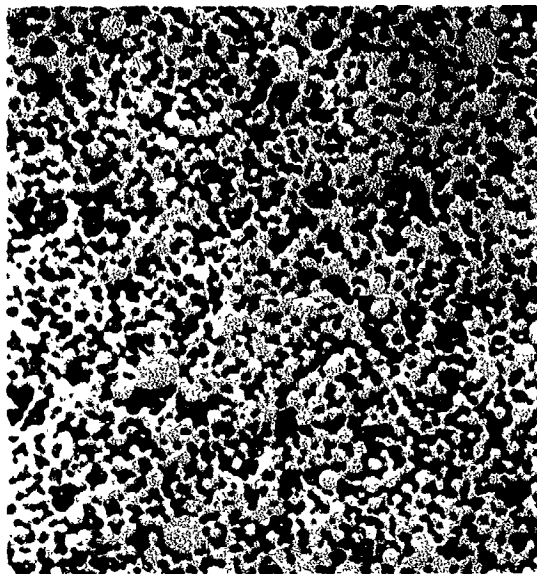
NEG. 1225   DENSITY = 70.05%

W-15 A/o Ta
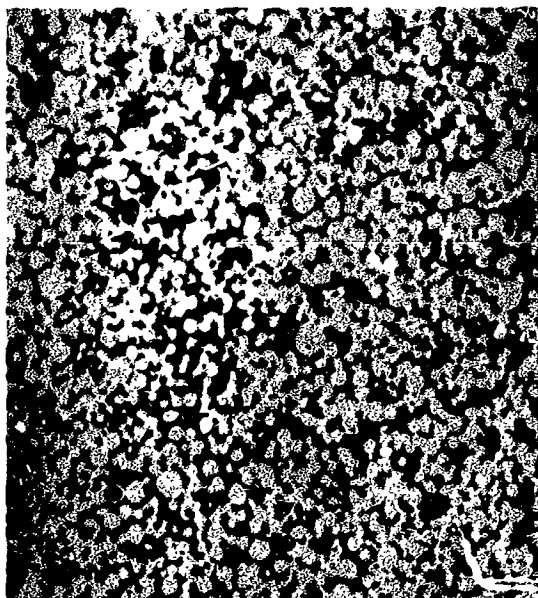
NEG. 1275   DENSITY = 66.42%

W-20 A/o Ta
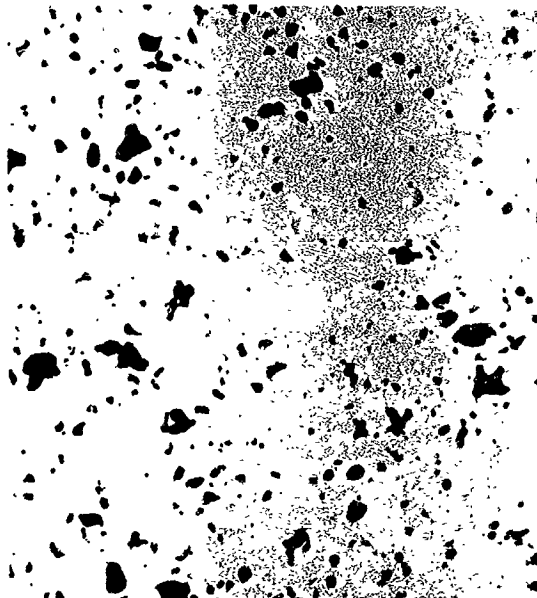
NEG. 1216   DENSITY = 79.06%

W-4 A/o Cr

FIG. 6-1   STRUCTURES OF TUNGSTEN ALLOYS, MADE FROM 4-8μ TUNGSTEN MICROSPHERES, 1-3μ TANTALUM AND 3-7μ CHROMIUM POWDERS. ALLOYS WERE SINTERED AT 2000°C FOR 240 MINUTES (Mag. = 300X)

The 2200° sintering data are plotted in Fig. 6-2. Here the markedly slower sintering rate of the tantalum alloys is compared with that of the unalloyed tungsten base. Again, the higher tantalum contents were the more effective in retarding sintering rate, and the 3-8μ tantalum was more effective than the 1-3μ particle additive. The reason for the latter effect is not at all well understood. Another very interesting feature of the W-Ta curves of Fig. 6-2 is the initial decrease in density with time. It is believed to be caused by initial rapid diffusion of tantalum into the lattice of the tungsten particles, with a resulting expansion rather than the normal shrinkage. This behavior, typical of the Kirkendall effect, also indicates the reason for the appearance of unduly large voids in the W-Ta structures.

The microstructures of the 2nd W-Ta series are shown in Fig. 6-3, where the degree of sintering is seen to have decreased markedly with increasing tantalum content. The effect of the $\triangle 200$°C sintering or particle growth is also apparent by comparing Fig. 6-3 with 6-1.

The hypothesis that large voids can be formed by the diffusion of tantalum into tungsten particles is supported by the micrographs of Fig. 6-4. These compare a W-10 Ta alloy, made using 3-8μ Ta particles, with the same composition made from 1-3μ Ta. Voids in the 3-8μ Ta sample are obviously much larger.

Figure 6-5 illustrates the structure of the W-20 Ta alloy at 400, 1000, and 3000 x magnifications. The relatively narrow width of the diffusion bridges is made evident by this figure. At 4000 x, it may be noted that each bridge is traversed by a grain boundary, indicating that each constituent particle retains a distinct crystallographic orientation.

6.4 Alloy Series No. 3

A third series of W-Ta alloys was prepared, wherein 2-5μ tungsten (Lot E4) was substituted for the 4-8μ fraction (E7A). This
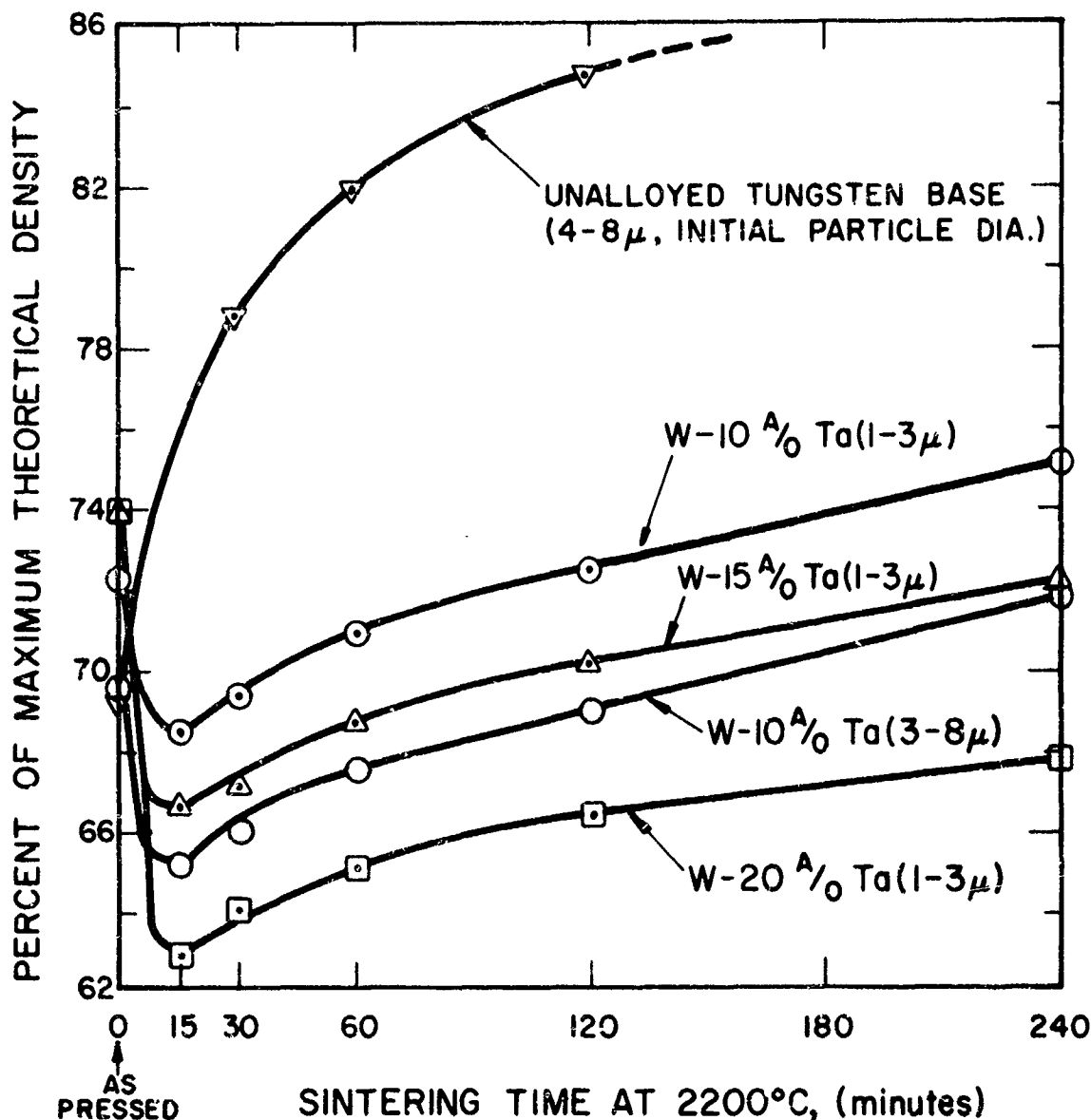
FIG. 6-2   EFFECT OF TANTALUM ON 2200°C SINTERING RATE OF LOT
          E7A TUNGSTEN MICROSPHERES OF 4-8μ DIAMETER   (Atom
          percentages and size ranges of the tantalum additives
          are rated on respective curves above. All sintering
          performed at 5 X 10⁻⁵ torr)
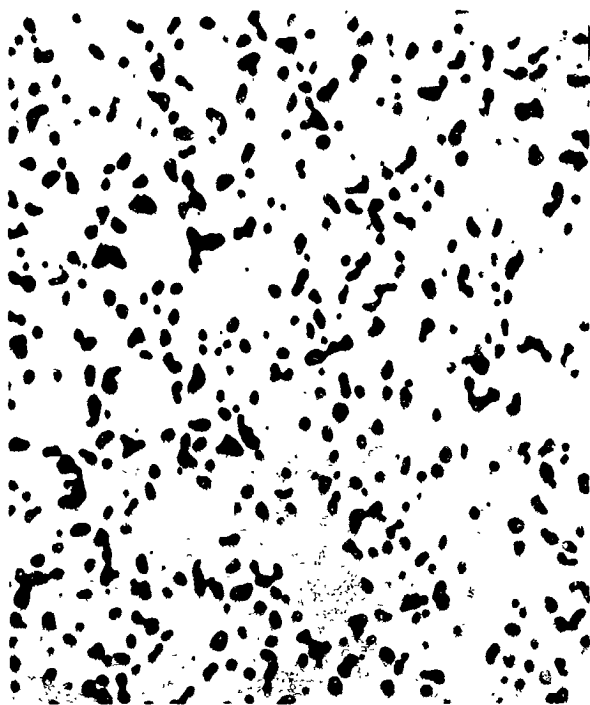
NEG. 1313   PURE TUNGSTEN
SINTERED 2 HRS. AT 2200°C
DENSITY = 84.7%
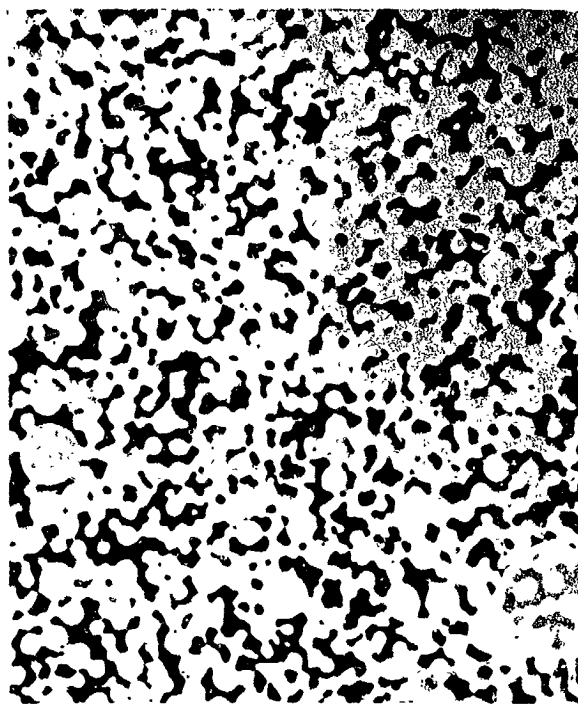
NEG. 1305   W-10 A/o Ta
SINTERED 4 HRS. AT 2200°C
DENSITY = 75.0%
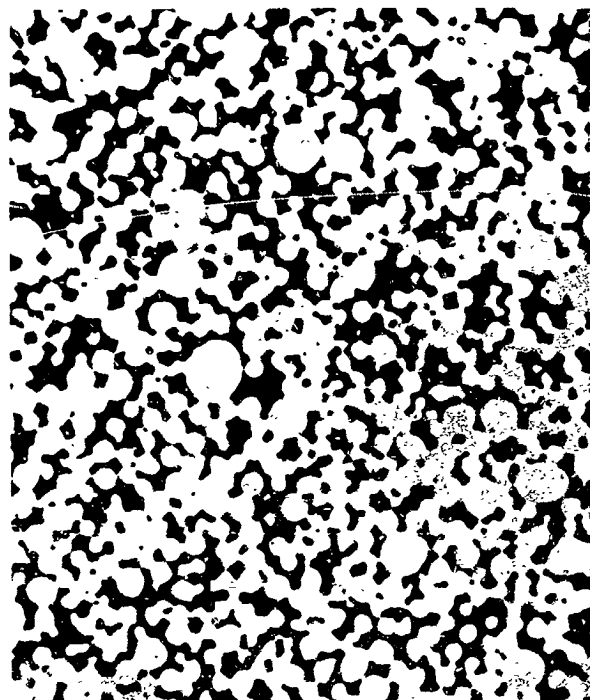
NEG. 1306   W-15 A/o Ta
SINTERED 4 HRS. AT 2200°C
DENSITY = 72.1%
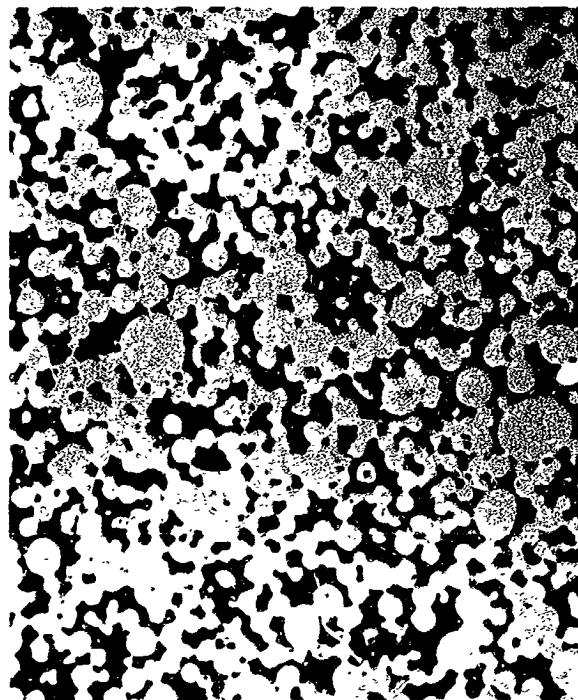
NEG. 1307   W-20 A/o Ta
SINTERED 4 HRS. AT 2200°C
DENSITY = 67.8%

FIG. 6-3. EFFECT OF TANTALUM PARTICLE ADDITIONS ON PORE STRUCTURE OF
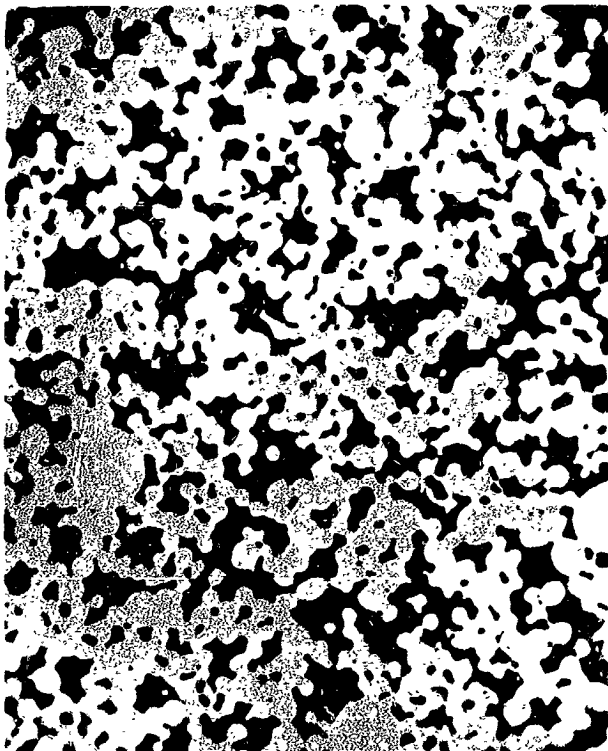
NEG. 1304   3-8μ Ta ADDED   NEG. 1305   1-3μ Ta ADDED

DENSITY = 71.8%   DENSITY = 75.0%

COMPOSITION, W-10 A/o Ta
SINTERED 4 HRS. AT 2200°C

FIG. 6-4   EFFECT OF TANTALUM PARTICLE SIZE ON THE PORE STRUCTURE OF SINTERED
           (4-8μ) TUNGSTEN MICROSPHERES (Mag. = 400X)
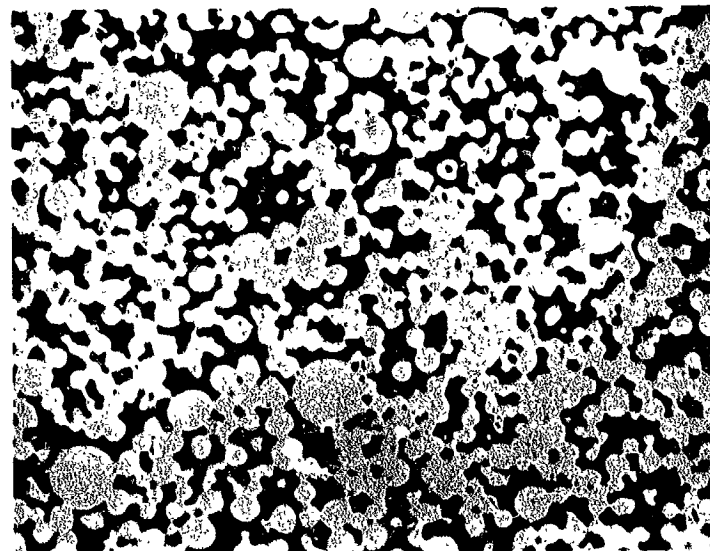
NEG. 1309   MAG. = 3000X
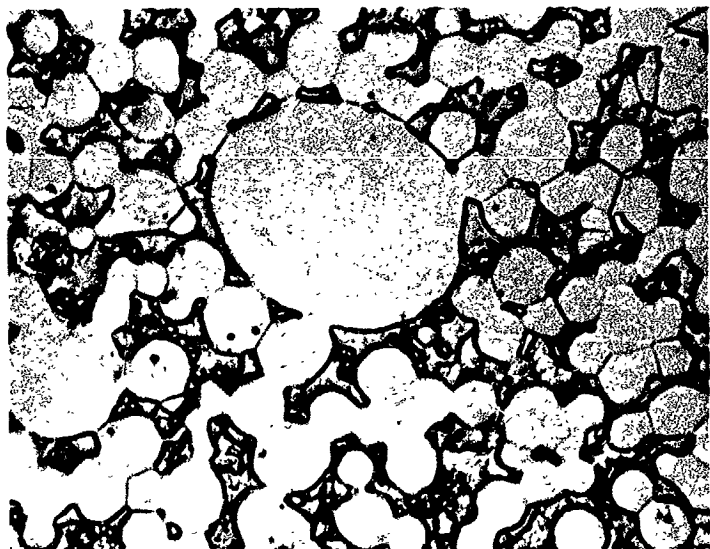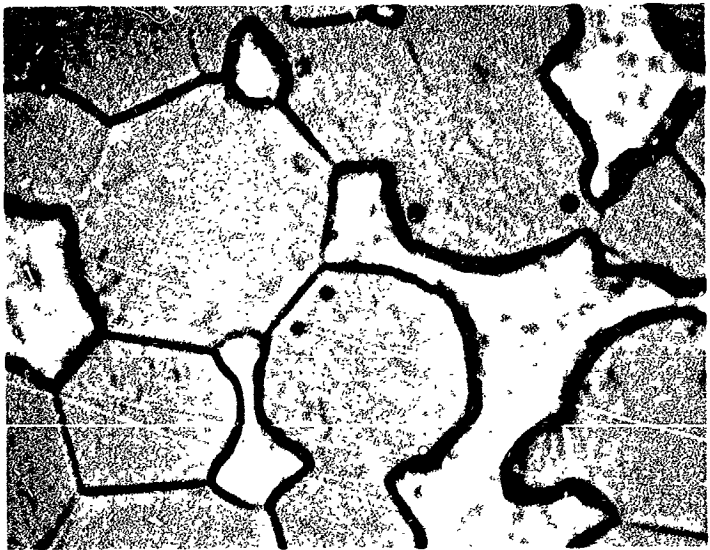
NEG. 1311   MAG. = 1000X

NEG. 1307   MAG. = 400X

COMPOSITION, W-20 A/o Ta
SINTERED 4 HRS. AT 2200°C
DENSITY = 67.8%

FIG. 6-5   PORE STRUCTURE OF W-20 A/o Ta AT VARIOUS MAGNIFICATIONS
(4-8μ Tungsten Microspheres; 1-3μ Tantalum Additive)

NEG. 1309　　　　　MAG. = 3000X
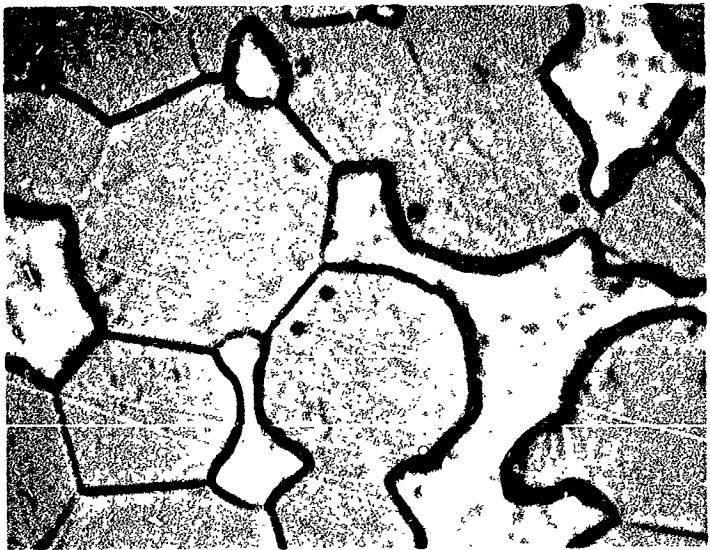
NEG. 1311　　　　　MAG. = 1000X

COMPOSITION, W-20 A/o Ta
SINTERED 4 HRS. AT 2200°C
DENSITY = 67.8%

NEG. 1307　　　　　MAG. = 400X

FIG. 6-5　PORE STRUCTURE OF W-20 A/o Ta AT VARIOUS MAGNIFICATIONS
(4-8μ Tungsten Microspheres; 1-3μ Tantalum Additive)

substitution was made in order (1) to refine the pore size of the resulting sintered material, and (2) to effect increased sintering rates, such that the 80 percent target density could be achieved within reasonable sintering time (less than 4 hours at 2200°C). Also, for this W-Ta series, the 1-3µ tantalum fraction (BF) was used in preference to the 3-8µ tantalum fraction (EF) in order to achieve more homogeneous and finer porosity.

Sintering rates of the third alloy series are listed in Table 6-III and plotted on a semi-log scale in Fig. 6-6. Comparison of Tables 6-III and 6-II shows that the as-pressed densities of the finer (2-5µ) powder samples of Series 3 were consistently and significantly lower than the pressed densities of the (4-8µ) Series 2. Further, the 4-hour sintered densities of Series 3 are also significantly higher than those of Series 2. The marked increase in sintering rate is due, obviously, to the higher free energy surface of the finer tungsten substituted, since all other conditions were held constant. The curves of Fig. 6-6 indicate that the retarding effect of tantalum on diffusion remains consistent with data derived on the previous two series. However, sintering time to reach the 80 percent density level has been reduced to less than 4 hours at 2200°C. It is also very interesting to note that, with the finer parent tungsten particles, a decrease in density (within the first 10 minutes of sintering) occurred only in W-20 Ta, as occasioned by a slight volume expansion. The reason for the appreciable initial expansion (Kirkendall effect) of the coarser (4-8µ) powder and the almost negligible expansion of the fine (2-5µ) powder is not known.

TABLE 6-III

SINTERING RATE DATA FOR W-Ta ALLOYS
(Alloy Series No. 3)

Tungsten Base Powder	Additive Metal Lot	Sintering Time, min., at 2200°C under 5×10^{-5} torr					
		0 (As-Pressed)	10	30	60	120	240
		% Theoretical Density					
E4 (2-5μ)	Unalloyed	65.49	78.29	85.54	88.55	91.30	93.58
E4 (2-5μ)	10 A/o Ta BF (1-3μ)	65.24	70.25	73.72	78.15	83.57	86.31
E4 (2-5μ)	15 A/o Ta BF (1-3μ)	66.38	67.23	71.91	74.56	81.09	83.43
E4 (2-5μ)	20 A/o Ta BF (1-3μ)	66.58	64.22	68.29	71.02	77.29	81.09
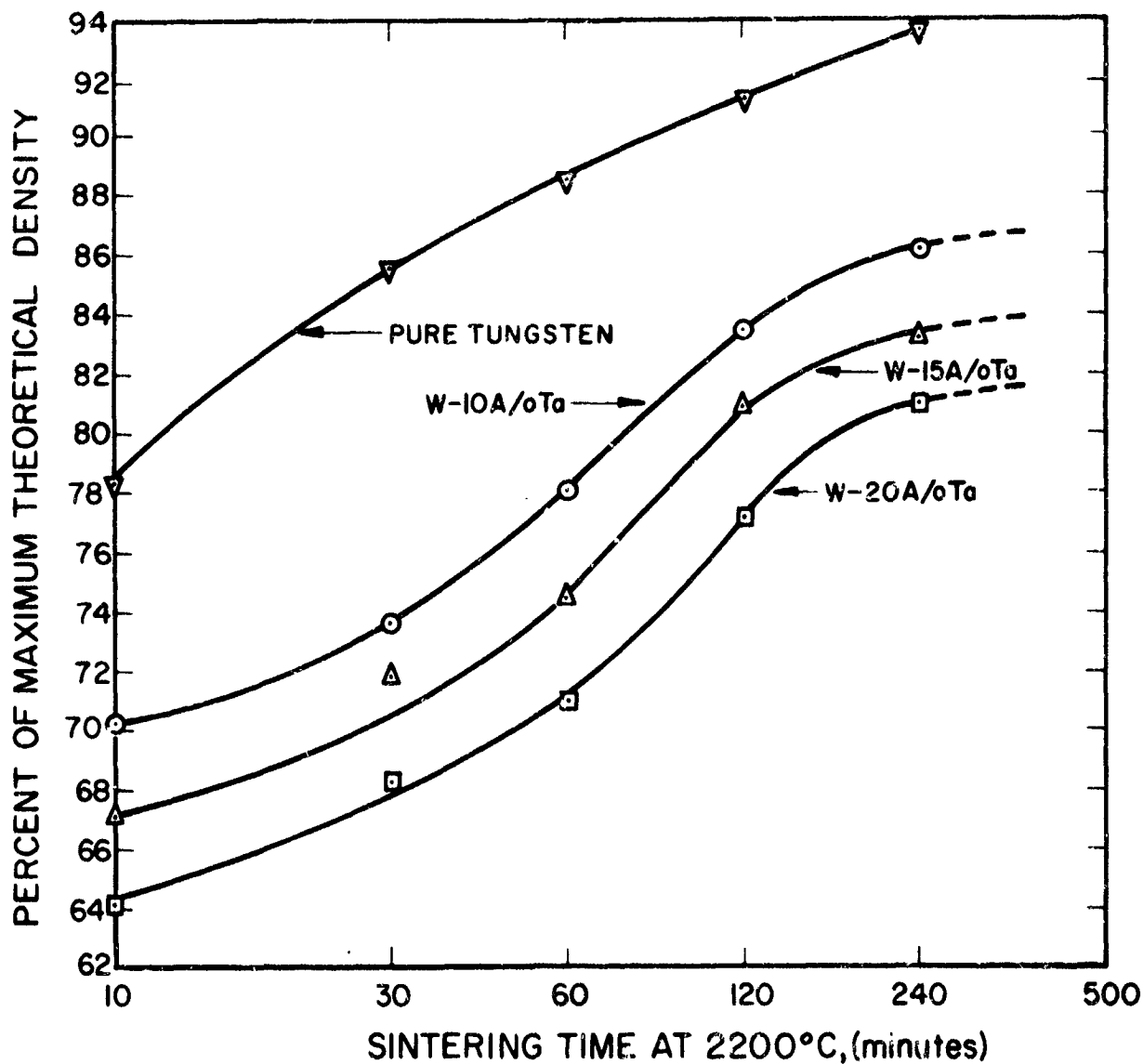
FIG. 6-6   EFFECT OF (1-3μ) TANTALUM PARTICLES ON 2200°C SINTERING
RATE OF (2-5μ) TUNGSTEN MICROSPHERES

6.5 Preparation of Series No. 3 at 80 Percent Density

Standard barrel compacts, five each of the unalloyed 2-5μ (E4) powder and of the 10, 15, and 20 Ta powder mixtures had been pressed initially. One compact of each composition was used for the density study described in Section 6.4. The remaining total of 16 compacts (4 of each composition) were vacuum sintered at $2200^{\circ}C$ for the following times, interpolated from previous densification rate curves (see Figs. 6-6 and 4-6) as being necessary to achieve 80 percent target density:

Composition*	Sintering Temp., $^{\circ}C$	Time, min.
Unalloyed tungsten	1800	105
W - 10 A/O Ta	2200	67
W - 15 A/O Ta	2200	97
W - 20 A/O Ta	2200	156

*2-5μ tungsten, 1-3μ tantalum

The <u>unalloyed</u> tungsten compacts were infiltrated successfully with Cu-2 Fe under hydrogen. To determine whether the standard Cu-2 Fe would penetrate W-Ta, 2 quartz capsules were prepared. Both were charged with scrap pieces of sintered W-20 Ta. Pure copper was put into one capsule and Cu-2 Fe into the other. Then the capsules were sealed under vacuum. After being heated at $1300^{\circ}C$ for 30 minutes, the test samples were sectioned. They revealed somewhat shallower Cu than Cu-2 Fe penetration. Thereupon, all 12 W-Ta compacts (4 of each composition) were immersed in the Cu-2 Fe under vacuum.

At this juncture, metallographic samples were taken from the ends of four compacts (one of each composition) and noninfiltrated compact interiors were again noted. Structures of the unalloyed tungsten and W-10 Ta compacts are compared in Fig. 6-7. These structures were resolved in better detail than in previous attempts through use of a final alternate etch-polish* technique. Comparison of the unalloyed

*Etchant - one part concentrated NH_4OH_4 + two parts Murakami's reagent.

tungsten structure of Fig. 6-7 with that of the lower left micrograph
of Fig. 4-15 reveals the presence of fine pores which had not been
defined by previous polishing techniques. This demonstrates the pit-
falls of placing complete reliance on optical analysis. Comparison
of the two micrographs of Fig. 6-7 indicates that considerable agglom-
eration of W-10 Ta occurred at the 2200°C sintering temperature, while
such agglomeration did not occur in the unalloyed tungsten (sintered
at only 1800°C). Because of this, the pore structure of the W-10 Ta is
less homogeneous than that of the unalloyed sample. In general, it
would appear that addition of tantalum _in discrete particle form_ does
not yield ionizer pore structures as favorable as do tungsten micro-
spheres alone. This is not to say that application of tantalum _as_
coatings on the tungsten microspheres will be ineffective. In fact,
all metallurgical indications point to this technique as being best.

Two more attempts were made to infiltrate the W-Ta alloys
at approximately 1200°C under vacuum. For these experiments, the
Ag-39.9 A/O Cu eutectic alloy was used. Its melting point of 779°C,
being 304° below that of Cu and 182° below that of Ag, indicates that
it should be more fluid at the 1200°C temperature of infiltration.
After the first immersion in Ag-Cu, it was observed that the interiors
of the samples were reasonably infiltrated, while the exteriors were
not. It was deduced from this that preferential oxidation of the sample
exteriors had occurred during processing, which oxidized surface zones
were not being wetted. The use of a parting layer of MgO, which had
been used to prevent diffusion welding of the samples to the tungsten
sheet base during sintering, came under suspicion. New samples of
W-15 and 20 Ta were pressed and sintered without use of the MgO film.
When immersed subsequently in the Ag-Cu eutectic, wetting of the samples
was excellent and infiltration was undoubtedly very thorough. In retro-
spect, the reason for the infiltration difficulties becomes quite ap-
parent. At 2200°C, the MgO vaporized to react with tantalum. Free-
energy data from Coughlin[2] indicate that the following reaction is in

_____

2. Coughlin, J. P., Bulletin 542, BuMines, 1954.
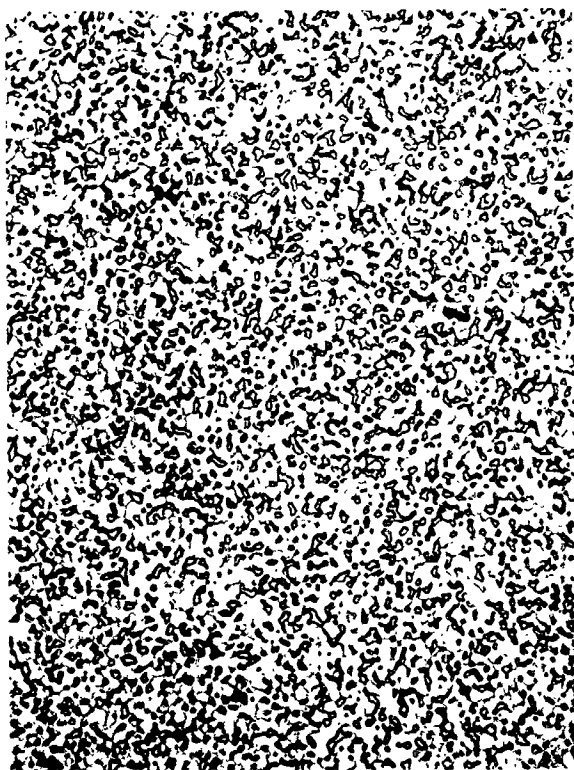
| NEG. 1399 | PURE TUNGSTEN | NEG. 1400 | W-10 A/o Ta |

| DENSITY = 81.55% OF THEORETICAL | DENSITY = 79.36% OF THEORETICAL |

FIG. 6-7   EFFECT OF TANTALUM PARTICLE ADDITIONS ON PORE STRUCTURES OF SINTERED
TUNGSTEN MICROSPHERES (2-5μ Tungsten; 1-3μ Tantalum)

equilibrium at about 2340°C and that it will proceed to the right at higher temperatures:

$$5 \text{ MgO} + 2 \text{ Ta} \rightleftharpoons 5 \text{ Mg} + \text{Ta}_2\text{O}_5$$
$$\sim 2340°C$$
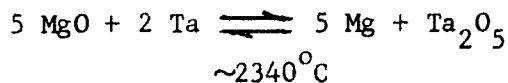
However, the impaired wetability of W-Ta surfaces (when heated in proximity with MgO) indicates that at least a tantalum suboxide, such as Ta_2O_4, does form at 2200°C. Having determined the apparent reason for the inability to obtain complete infiltration initially, it is entirely possible that satisfactory infiltration of W-Ta can be obtained with the standard Cu-2 Fe infiltrant in the future.

6.6 Conclusions of Alloy Study

Considerable information was derived from this alloy study, particularly on the W-Ta compositions. Conclusions are listed briefly as follows:

1. A 4 A/O addition of chromium is not indicated to retard the diffusion and sintering rate of spherical tungsten powder. The nonuniformity of pore structure of W-4 Cr, when sintered at 2000°C, is attributable to melting of the chromium. Such liquation cannot be tolerated in any sintering of powdered metals.

2. Addition of tantalum to tungsten, even as articulate particles, greatly retards diffusion and sintering rate.

3. W-Ta powder mixtures are appreciably more amenable to oxidation than is pure tungsten powder. Results of this study indicate that tantalum, e.g., can reduce MgO at 2200°C. The oxide layer formed by such reduction acts to prevent subsequent wetting and absorption of the infiltrant.

4. Three combinations of W-Ta particle sizes were investigated, with results generally as follows:

a. Coarse W + coarse Ta = lowest X   coarsest   least X

b. Coarse W + fine Ta = $\left(\begin{array}{c}\text{sintering}\\\text{rate}\end{array}\right) \left(\begin{array}{c}\text{pore}\\\text{structure}\end{array}\right)$ (agglomeration)

c. Fine W + fine Ta =   highest   finest X   greatest

Characteristics marked with X, above, being most favorable
for the ionizer application, it becomes clear that optimum
characteristics cannot be achieved by starting with articulate
powder mixtures.   It also becomes apparent that use of fine
Ta-coated microspheres offers the best probability of success.

7. TEST SAMPLES FOR NASA-LEWIS

In accordance with Article I, Phase V of the Contract, Scope of Work, samples of infiltrated tungsten and of tungsten alloys were prepared for NASA, as described in the following subsections. These have been submitted to the Contract Technical Manager.

7.1 Tungsten Samples from Phase II (All ~75 Percent Dense)

No. Submitted	Powder - Base Particle Size	Infiltrant	Date Submitted
2	4-8μ	Silver	11 Feb. 1964
2	4-8μ	Cu-2 A/o B	11 Feb. 1964
2	4-8μ	Cu-2 A/o Be	11 Feb. 1964
2	4-8μ	Cu-2 A/o Fe	11 Feb. 1964
2	4-8μ .	Cu-2 A/o P	11 Feb. 1964
2	4-8μ	Cu-2 A/o Te	11 Feb. 1964

7.2 Tungsten Samples from Phase III (All Infiltrated with Cu-2 A/o Fe)

No. Submitted	Powder - Base Particle Size	% Theoretical Density (From Control Sample)	Date Submitted
2	1-4μ	78.24	29 Oct. 1963
2	3-6μ	81.09	29 Oct. 1963
2	4-8μ	78.45	29 Oct. 1963

Recommended distillation treatment: 15 minutes at $1500^{\circ}C$ plus 45 minutes at $1750^{\circ}C$, under 10^{-5} torr pressure.

7.3 Alloy Samples from Phase IV (All ~80 Percent Dense)

No. Submitted	Base Powder Lot Tungsten	Tantalum	Infiltrant	Date Submitted
2	E4	None	Cu-2 A/o Fe	11 Feb. 1964
2	E4	10 A/o BF(Ta)	Ag-39.9 A/o Cu	11 Feb. 1964
2	E4	15 A/o BF(Ta)	Ag-39.9 A/o Cu	11 Feb. 1964
2	E4	20 A/o BF(Ta)	Ag-39.9 A/o Cu	11 Feb. 1964

8. CONCLUSIONS AND RECOMMENDATIONS

Main conclusions, derived from the research, will be reviewed in this section, together with recommendations where they are applicable. This summary will be made in sequence, starting with procurement of the powder and its classification, infiltration, pore characterization of sintered tungsten, ionization performance of graded spherical ionizers, and conclusions of the tungsten alloy study.

8.1 Procurement, Classification and Analysis of Tungsten Microspheres

A special fine grade of spherical powder was developed by the Linde Co. for use in this contract. Powder refinement achieved is indicated by the following frequency of minus 8μ-dia. particles:

	Percentage by Weight	Percentage by No.
Previous Coarse Grade	18.0	91.5
Special Fine Grade	90.0	99.9

This refinement is significant in that the narrower the size distribution of the feed powder, the narrower become the size fractions removed subsequently by cyclonic air classification. Since the percentage of unusable oversized powder is greatly reduced, an economy is also realized.

Having attempted to classify spherical tungsten powder by three wet methods, and also to conduct size analyses by a wet electronic method, it is concluded that such wet methods are ineffective because of tungsten particle agglomeration. Dry methods of both classification (cyclonic air) and size analyses (micromerograph) were found to be far superior. Therefore, cyclonic air classification was employed to size the basic powder required for work reported, and is recommended for use in the future. Results indicated that, by performing duplex classification steps, predominant particle-frequency groupings were obtained as follows:

Percentage by No.	Within Dia. Range
89	1-4μ
95	3-7μ
88	4-9μ

These frequencies are believed to represent the best present commercial practice, such that achievement of narrower distribution spectra may depend on first obtaining microspheres having greater as-produced size uniformity.

Analysis of fine spherical tungsten by micromerograph minimizes the agglomeration problem encountered in Coulter electronic counting and in slide dispersion samples (necessary for microscopic counting). With the micromerograph, using explosive deagglomeration of dry powder, it is still not possible to state that 100 percent dispersion is obtained. However, the micromerograph must be recommended as being the most feasible analytical tool from the standpoint of combined accuracy, speed and economy.

Spectrographic analyses indicated that the tungsten base powder used in this work exceeded 99.94 percent purity. It is apparent that the spectrographic method is most suitable for detecting the small residual impurity levels. Carbon determinations by the conductometric method indicated 115 and 60 parts per million for the coarse and fine spherical powder grades, respectively.

8.2 Infiltration Study

A summary of the advantages and disadvantages of various compositions used to infiltrate tungsten is as follows:

Infiltrant Composition	Main Advantage	Main Disadvantage
Pure Ag	Constant concentration of molten bath	Relatively high cost
Cu-2 A/o B	Low residual B after distillation	B renders tungsten unmachinable
Cu-2 A/o Be	Excellent machinability	Comp. instability of molten bath due to oxidation of Be (also toxicity)
Cu-2 A/o Fe	Excellent machinability	None detected
Cu-2 A/o P	Comp. stability of molten bath	High residual P after distillation
Cu-2 A/o Te	No outstanding advantage or disadvantage	

No differences were noted in the ability of the six compositions to infiltrate porous tungsten. No significant differences in microstructure or permeability of the variously infiltrated samples were noted after the infiltrants were removed. Evidence was obtained that boron diffuses rapidly into tungsten, accompanied by a lowering of the melting point, an increase in hardness, and a serious decrease in machinability. The principal conclusion reached is that Cu-2 A/o Fe is at least as effective as, or is better than, any of the other compositions included in this comparison study. Therefore, Cu-2 A/o Fe was used as the standard infiltrant in this contract and is recommended for use in the future.

8.3 Characterization of Ionizers Prepared from Three Spherical Powder Fractions

In fabricating the ionizer series several parameters were held as constant as was feasible, while only one parameter was varied intentionally:

Constant Parameters	Varied Parameter
Hydrostatic compaction and pressure level	Particle size (distribution) of spherical powder fractions
Compact size and configuration	
Vacuum sintering and ambient pressure level	
Vacuum distillation conditions	
Final density, surface finish and purity	

Evaluation of the spherical powder ionizers included determination of sintering rate and final density, measurement of mass permeability coefficient, calculation of transmission coefficient (plus necessary derivations), analysis of open and occluded pore volume by Hg intrusion, metallographic examination, determination of mean pore size and pores/cm^2, and spectrographic analysis of final purity.

Fabrication experiments on spherical powder fractions indicate that the finer the initial spherical powder used, the lower the pressed "green" density obtained. Further, the finer the powder, the more rapid the sintering rate and the lower the thermal stability of the ionizers obtained. These observations are in agreement with theoretical expectations. Because of higher total free energy surface, the finer powder fractions should be (and were) sintered at lower temperatures than coarser fractions. Hence, care should be (and was) taken not to exceed the powder-sintering temperature in post-sintering steps, lest additional sintering, shrinkage, and structural changes occur. Where the ionizer attachment operation makes overheating absolutely necessary, time at peak temperature should be (and was) minimal.

Ionizer buttons from three powder size categories (each category having three different surface finishes) were prepared. Average density and permeability coefficients were determined to be as follows:

Surface Finish*	E3 (1-4μ) Powder		E6 (3-6μ) Powder		E7A (4-8μ) Powder	
	Density	Perm.x10^6	Density	Perm.x10^6	Density	Perm.x10^6
Lathe turned	80.10	0.18	79.75	0.24	80.26	0.42
Machine ground	80.88	0.21	80.67	0.27	80.98	0.46
Polished	81.14	0.19	80.78	0.24	80.67	0.46
Overall average	80.71	0.19	80.51	0.25	80.66	0.45

*Finish: lathe turned = ~60 rms; machine ground = ~6 rms; polished = <1 rms.

Foregoing average values indicate that, sintered density being constant, increasing the initial powder-particle size yields ionizers of increasing permeabilities.

Plotting of individual "density vs. permeability" values for the nine ionizer categories indicated that surfacing by lathe causes significantly more surface distortion and pore closure than does either machine grinding or metallographic polishing. Surprisingly, such plots indicate also that any pore closure resulting from machine grinding is not significantly different from that resulting from metallographic polishing. Based on these data, the machine-ground surface was selected as the standard for all ionization performance testing.

Pore distribution analysis of ionizer material by mercury intrusion was investigated in the present contract. Pore spectra obtained on porous samples (of comparable densities) show a definite shift to finer pore size distributions with the use of finer spherical base powder. Based on careful pore counts at high magnification, the average pore diameters were calculated. Mean pore diameter values obtained were 3.83, 3.51, and 2.50 microns for sized spherical powders of 6.9, 4.9, and 2.7 microns, avg. particle diameters, respectively. For this same series, pore per cm^2 were determined to be 1.64, 1.99, and 4.01 x 10^6, respectively.

Overall correlation of the data indicates that, as the initial powder spectrum is shifted toward smaller particle sizes, the following trends occur in the final ionizers:

1. Mean pore diameter decreases;

2. Pore per unit area increase;

3. Volume of occluded pores increases slightly; and

4. Permeability and transmission coefficients decrease.

8.4 Ionization Performance of Classified Spherical-Powder Ionizers

Experimental data presented in this report show that ionization performance is improved by decreasing ionizer pore size and increasing density of pore packing. The classified spherical powder ionizers have exceeded all expectations in their ionization performance, and have made possible, for the first time, ion current densities of 30-60 ma/cm^2. Such high ion current densities were reached at the surprisingly low neutral fraction levels of 1-3 percent at 50 ma/cm^2. Critical temperatures for the finer 1-4 and 3-6μ spherical powder ionizers were lowest.

Based on the limited number of test buttons, the finest spherical powder ionizers are indicated to perform far better than any of the commercial porous ionizers. It would have been desirable to test not only a greater number of classified powder ionizers, but also a number of unclassified fine spherical powder ionizers. The excellent ionization performance of the fine classified spherical powder ionizers indicates their great potential for future application, assuming in this that their thermal stability is adequate, or can be made so, by the metallurgical techniques proposed for investigation in the follow-on contract.

8.5 Thermal Stabilization of Tungsten Microspheres by Alloying

The retarding effect of tantalum on the diffusion of tungsten, observed under the preceding NASA contract as well as by other investigators, has been verified. Addition of tantalum particles to spherical tungsten powder markedly decreased sintering rates. Increasing the tantalum added, over the range 10-20 atom percent, resulted in progressively lower sintering rates. While the reason for the effect of tantalum on diffusion rate is not known, results presented indicate that (at 2000-2200°C) tantalum particles diffuse very rapidly into their tungsten neighbors, with an attending expansion of the tungsten lattice. The similarity of atomic size dictating the formation of substitutional solid solutions, the speed of the initial diffusion is quite startling. Photomicrographs presented indicate that the diffusion of tantalum into tungsten particles leaves outsized voids, which voids destroy structural homogeneity. The larger the size of tantalum particles added, the larger these voids become. Experiments with three different combinations of constituent particle sizes indicate the following trends in final sintered structure:

Coarse W + coarse Ta =	lowest X	coarsest	lea.. X
Coarse W + fine Ta =	(sintering rate)	(pore structure)	(agglomeration)
Fine W + fine Ta =	highest	finest X	greatest

The "X" designations, above, indicating the directions favorable for best ionizer pore structures, it becomes apparent that the fabrication of optimum structures from mixtures of tungsten and tantalum is not feasible. The alternative, and that proposed for investigation in the follow-on contract, is to use sufficiently fine spherical tungsten particles, individually coated with a thin layer of tantalum or other diffusion-retarding element. This technique is expected to provide sintered structures having improved thermal stability, as well as pore size uniformity comparable to the best unalloyed tungsten.

Addition of chromium to spherical tungsten powder did not reduce subsequent diffusion and sintering rate. The very nonuniform pore structure resulting is attributed largely to melting of the chromium at the 2000°C sintering level. Use of chromium as a stabilizing addition to tungsten powder is not indicated to be beneficial.

APPENDIX   A

CLASSIFIER REPORT, ANALYTICAL REPORTS
AND DERIVATION OF TRANSMISSION COEFFICIENT

K-8 Sharples Super Classifier Test Report No. 1374

Company: Electro-Optical Systems, Inc.
300 North Halstead Street
Pasadena, California

Test Date: May 20, 1963

Requirements

Separate the 9 lbs. of Lot E Spherical Tungsten powder into 1-2 μ , 4-5 μ , and 7-8 μ fractions, with a goal to obtain 90% by number of the particles within the desired groups.

Test

The K-8 Classifier was setup and the sequence of separations is shown on the attached Table I. The Runs Nos. 1 and 2 are made at the finest settings and producing a minus 1 μ (Fine Run 2) and the 1-2 μ (Coarse Run 2) products using the minus 2 μ (Fine Run 1) as a feed.

Runs 3 to 7A were made according to the following program: Using the coarse fraction from Run 1 as a feed, and setting the Classifier for a 3 micron cut, the Fine Run 3 is a 3 micron product. The coarse from Run 3 was used as a feed for Run 3A which was made at the same Classifier setting as Run 3. This product Fine 3A is also a 3 micron product, but will be slightly coarser than Run 3 Fine. Run 4 was then made at the 5 micron adjustment using Run 3A coarse as a feed, etc.

Micromerograph analyses of the products 2F, 2C, 3, 4, 4A, 5, 6, 7, and 7AC. The comparison shown between 4 and 4A gives an indication as to the amount of variation in the first pass and second pass fine fractions.

Results & Conclusions

The analyses of the products show no significant change in the slope of the curves, which is characteristic of the Classifier operation, however, the top 10% and the bottom 10% (by weight) has been improved. This is possible because of the second pass to remove the carryover fines from the previous run.

K-8 Sharples Super Classifier Test Report No. 1374

Company: Electro-Optical Systems, Inc.
300 North Halstead Street
Pasadena, California

Test Date: May 20, 1963

Run No.	1	2	3	3A	4	4A
Feed Material	Tungsten	Fine Run 1	Coarse Run 1	3 Coarse	3A Coarse	4 Coarse
Vane Setting	AA	AA	B	B	C	C
Rotor Speed	7800	7800	5250	5250	4250	4250
Feed Wt. Kgm	3.97	.13	3.67	3.27	2.97	2.63
Coarse Wt. Kgm	3.67	.08 (2C)	3.27	2.97	2.63	2.37
Fine Wt. Kgm	.13	.02 (2F)	.27 (3)	.23 (3A)	.35 (4)	.24 (4A)
Loss Wt. Kgm	.17	.03	.13	.07	+.01	.02

K-8 Sharples Super Classifier Test Report No. 1374

Run No.	5	5A	6	6A	7	7A
Feed Material	4A Coarse	5 Coarse	5A Coarse	6 Coarse	6A Coarse	7 Coarse
Vane Setting	C-D	C-D	.583	.583	.586	.586
Rotor Speed	3650	3650	3650	3650	3050	3050
Feed Wt. Kgm	2.37	2.01	1.69	1.49	1.30	.93
Coarse Wt. Kgm	2.01	1.69	1.49	1.30	.93	.74 (7AC)
Fine Wt. Kgm	.35 (5)	.30 (5A)	.21 (6)	.18 (6A)	.33 (7)	.22 (7AF)
Loss Wt. Kgm	.01	.02	+.01	.01	.04	+.03

Note: In the "Loss column" the plus (+) valves are gains or increase in material after classification due to the small amount of material hold-up in the K-8 unit which cannot effectively be collected between each run.

Test & Report by

Michael J. Maggio
Classifier Technical Sales

3720-Final

A-3

K-8 TEST 1374

PROCESS SEQUENCE

FEED ORIGINAL FEED

RUN1

F2 RUN2 C2

-2   2

F3 RUN3 C1

3⁻

C3

F3A RUN3A

3·+

C3A

F4 RUN4

4+5⁻

C4

F4A RUN4A

4+5⁺

C4A

F5 RUN5

6⁻

C5

F5A RUN5A

6⁺

C5A

F6 RUN6

7+8⁻

C6

F6A RUN6A

7+8⁺

C6A

F7 RUN7

9⁻

C7

F7A RUN7A

9⁺

C7A

+9

A-5

NO. 31,192. 20 DIVISIONS PER INCH (120 DIVISIONS) BY TWO 4½-INCH CYCLES RATIO RULING.

CODEX BOOK COMPANY, INC.   NORWOOD, MASSACHUSETTS.
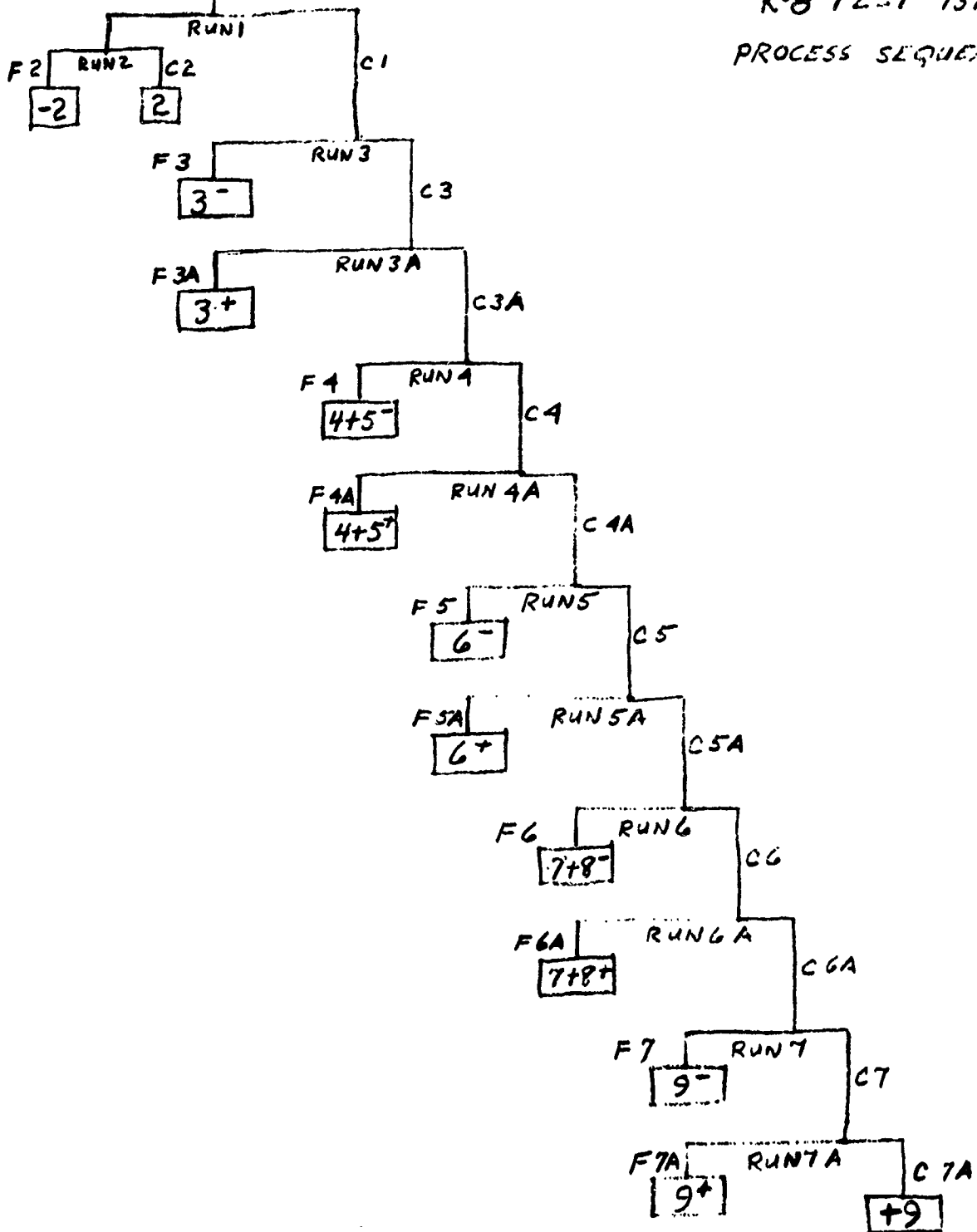
DEPARTMENT	ELECTRO-OPTICAL				RUN	SYMB	DEAGLM.	PRES.	COMMENT
MATERIAL	TUNGSTEN LOTE (SPHERES)								
SPECIFIC GRAVITY	19.3	DATE	5/20/63						
COMMENT	K-8 TEST 1374								

PARTICLE SIZE DISTRIBUTION ANALYSIS

LOTE

FEED

% WEIGHT LESS THAN DIAMETER

DIAMETER IN MICRONS

THE SHARPLES Micro-Centrifuge

FIG II

A-6

PARTICLE SIZE DISTRIBUTION ANALYSIS
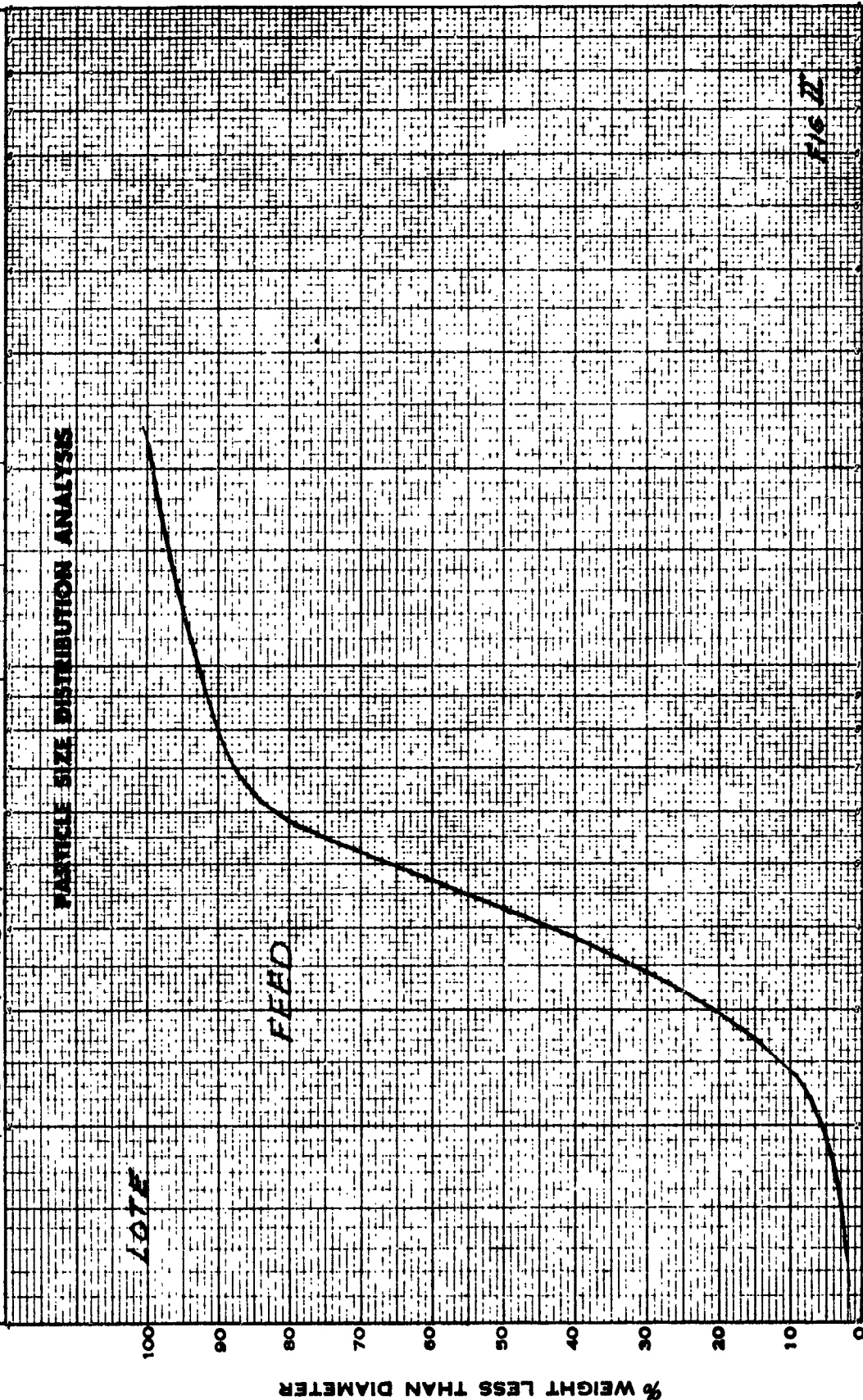
DEPARTMENT	ELECTRO OPTICAL	RUN	SYMB	DIAGLM.	PREP.	COMMENT
MATERIAL	TUNGSTEN LOT E					
SPECIFIC GRAVITY	19.3	DATE	5/23/63			
COMMENT	K-8 TEST 1374					

CODEX BGE COMPANY, INC.   N WOOD, MA A

% WEIGHT LESS THAN DIAMETER

100 90 80 70 60 50 40 30 20 10 0

DIAMETER IN MICRONS

1   2   5   10   20   50   100

THE SHARPLES *Micromerograph*

THE SHARPLES CORPORATION RESEARCH LABORATORIES, 424 W. 4TH ST., BRIDGEPORT, PA.

FORM NO. M-2
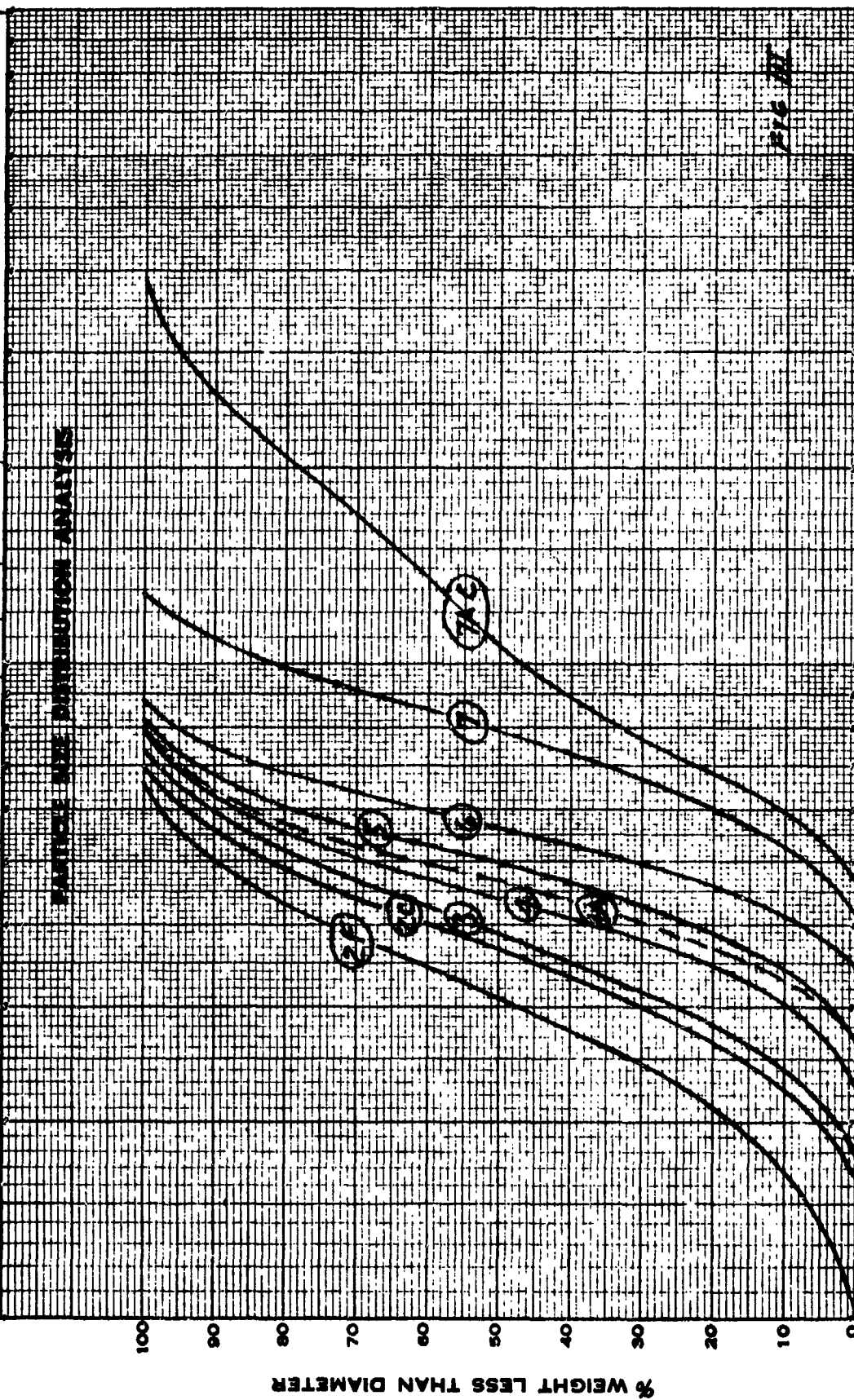
MATERIALS TESTING LABORATORIES

DIVISION OF MAGNAFLUX CORPORATION
6800 EAST WASHINGTON BOULEVARD
LOS ANGELES 22, CALIFORNIA
TELEPHONE 685-6001

TO: ELECTRO-OPTICAL SYSTEMS, INC.
300 N. Halstead Street
Pasadena, California

LABORATORY NO. 3282-4-1 & 3282-3-1

DATE 7-12-63

MATERIAL Tungsten Powder

SPECIFICATION ---------

YOUR P.O. No. 30829 Shipper # D 1016

CERTIFIED REPORT OF CHEMICAL ANALYSIS
QUANTITATIVE SPECTROGRAPHIC ANALYSIS

EOS Lot C

Lab. No. 3282-4-1

Molybdenum	30	ppm
Beryllium	1	ppm**
Iron	30	ppm*
Chromium	10	ppm**
Calcium	1	ppm*
Nickel	30	ppm**
Cobalt	100	ppm**
Zirconium	100	ppm**
Copper	3	ppm**
Aluminum	3	ppm*
Manganese	1	ppm**
Boron	10	ppm**
Total Other Elements	200	ppm*

*Less than
**Not detected less than

WET ANALYSIS

Lab. No. 3282-3-1

Conductometric Carbon-- 114.8 ppm

RESPECTFULLY SUBMITTED

MATERIALS TESTING LABORATORIES

3720-Final

MATERIALS TESTING LABORATORIES
DIVISION OF MAGNAFLUX CORPORATION
6800 EAST WASHINGTON BOULEVARD
LOS ANGELES 22, CALIFORNIA
TELEPHONE 685-6001

TO: ELECTRO-OPTICAL SYSTEMS, INC.

LABORATORY NO.   3282-4-2 & 3282-3-2

DATE   7-12-63

MATERIAL   Tungsten Powder

SPECIFICATION --------

YOUR P.O. NO.   30829 Shipper # D 1016

CERTIFIED REPORT OF CHEMICAL ANALYSIS
QUANTITATIVE SPECTROGRAPHIC ANALYSIS

3282-4-2

EOS Lot E

Molybdenum--------------------	30 ppm
Beryllium--------------------	1 ppm**
Iron--------------------------	30 ppm*
Chromium--------------------	10 ppm**
Calcium--------------------	1 ppm
Nickel--------------------	30 ppm**
Cobalt--------------------	100 ppm**
Zirconium--------------------	100 ppm**
Copper--------------------	20 ppm
Aluminum--------------------	3 ppm**
Manganese--------------------	1 ppm**
Boron--------------------	10 ppm**
Total Other Elements------	200 ppm*

*Less than
**Not detected less than

WET ANALYSIS

3282-3-2

Conductometric Carbon---- 60.4 ppm

RESPECTFULLY SUBMITTED

MATERIALS TESTING LABORATORIES

MATERIALS TESTING LABORATORIES

DIVISION OF MAGNAFLUX CORPORATION
6800 EAST WASHINGTON BOULEVARD
LOS ANGELES 22, CALIFORNIA
TELEPHONE 685-6001

TO: ELECTRO-OPTICAL SYSTEMS, INC.
300 N. Halstead Street
Pasadena, California

LABORATORY NO. 12383-4-1, 2, 3, & 4

DATE 12-26-63

MATERIAL Tungsten

SPECIFICATION ————

YOUR P.O. NO. 35850 Shipper # D 211

CERTIFIED REPORT OF CHEMICAL ANALYSIS
SPECTROGRAPHIC ANALYSIS

Lab Nos.	12383-4-1	12383-4-2	12383-4-3	12383-4-4
Identification:	EOS-E3	EOS-E6	EOS-7A	EOS-P.M.MOD-B
ELEMENT	PPM	PPM	PPM	PPM
Tungsten	Bal.	Bal.	Bal.	Bal.
Molybdenum	200*	200*	200*	200*
Beryllium	1.0*	1.0*	---	1.0*
Iron	170**	165**	94	290
Chromium	10.0*	10.0*	10.0*	10*
Calcium	1.0*	1.0*	1.0*	1.0*
Nickel	10*	10*	10*	10*
Cobalt	50*	50*	50*	50*
Zirconium	30.0*	30.0*	30.0*	30*
Copper	10*	10*	10*	10*
Aluminum	1.0*	1.0*	1.0*	1.0*
Manganese	1.0*	1.0*	1.0*	1.0*
Boron	10*	10*	10*	10*
Total Other Elements	200*	200*	200*	200*

*Not detected less than

**Corrected values are averages of
3 tests. Revision approved by
E. Duran of MTL.

RESPECTFULLY SUBMITTED

MATERIALS TESTING LABORATORIES

Derivation of Transmission Coefficient, C

From kinetic theory, the number of gas molecules striking unit area of solid surface in unit time

$$(1) \quad = \frac{n\bar{c}}{4}, \quad ------ \quad \frac{molecules}{cm^2 \cdot sec}$$

Total mass flux of arriving molecules is

$$(2) \quad \mu = \frac{\rho\bar{c}}{4}, \quad ------ \quad \frac{gm}{cm^2 \cdot sec}$$

From theory, the absolute pressure of gas is

$$(3) \quad P_d = \frac{\rho\bar{c}^2}{8}, \quad ------ \quad \frac{dynes}{cm^2}$$

From ideal gas law

$$(4) \quad P_d V = RRT \text{ or } \rho = \frac{P_d M}{RT}, \quad \frac{gm}{cm^3}$$

Solving (3) for $\bar{c}$ and substituting for ρ

$$(5) \quad \bar{c} = \sqrt{\frac{8 \, RT}{\pi \, M}}, \quad ------ \quad \frac{cm}{sec}$$

From (2), Mass Arrival Rate is

$$\mu = \frac{\rho\bar{c}}{4} = \frac{\rho}{4} \cdot \sqrt{\frac{8 \, RT}{\pi \, M}} = \frac{P_d M}{4 \, RT} \sqrt{\frac{8 \, RT}{\pi \, M}}$$

$$\mu = P_d \sqrt{\frac{M}{2\pi RT}} = \frac{P_d}{\sqrt{2\pi R}} \cdot \sqrt{\frac{M}{T}} = \frac{(1.333)(10)^3 \, P_{mm}}{\sqrt{2\pi R}} \cdot \sqrt{\frac{M}{T}}$$

$$(6) \quad \mu = 0.0584 \cdot \sqrt{\frac{M}{T}} \cdot P_{mm}, \quad ------ \quad \frac{gm}{cm^2 \cdot sec}$$

Mass Departure Rate is

$$(7) \quad \nu = \frac{dm}{A dt} = \frac{V M \delta P_d}{A R T \delta t} = \frac{(1.333)(10)^3 \, V M \, \delta P_{mm}}{A R T \delta t}, \quad ------ \quad \frac{gm}{cm^2 \cdot sec}$$

Transmission Coefficient is defined as

$$C = \frac{\text{Mass Departure Rate}}{\text{Mass Arrival Rate}} = \frac{\nu}{\mu}, \quad ------ \quad \text{dimensionless}$$

Dividing (7) by (6)

$$(8) \quad C = \frac{(1.333)(10)^3 \, V M \delta P_{mm}}{A R T \delta t} \cdot \frac{\sqrt{2\pi R}}{(1.333)(10)^3} \cdot \frac{\sqrt{2\pi M/RT} \cdot V \delta P_{mm}}{A \delta t \, P_{mm}}$$

$$= \frac{(8.428)(10)^{-5} V \, \delta P_{mm}}{A \delta t \, P_{mm}}$$

For N_2 at 298°K, C =

Conversion Factors Used

1 dyne/cm² = (1.333)(10)³ mmHg

R = (8.317)(10)⁷ ergs/mole·deg

1 erg = 1 dyne·cm = 1 gm·cm²/sec²

Symbol	Definition	Units
A	Area of porous medium perpendicular to gas flow.	cm²
$\bar{c}$	Mean velocity of gas molecules.	cm/sec
M	Molecular weight of gas.	gm/mole
m	Mass of gas.	gm
dm	Increment of mass (infinitesimal).	"
δm	" " " (finite).	"
N	Number of moles.	moles
n	" " molecules/cm³	molecules/cm³
P_d	Mean absolute pressure of gas in chamber.	dynes/cm²
δPd	Decrement of pressure in δt seconds.	" / "
ρ	Mean density of gas in test chamber.	g/cm³

Symbol	Definition	Units
P_{mm}	Mean absolute pressure of gas in chamber.	mm Hg
δP_{mm}	Decrement of pressure in δt seconds.	" "
R	Ideal gas constant.	erg/mole·deg
T	Temperature of gas.	°K
t	Time.	seconds
dt	Increment of time (infinitesimal).	"
δt	" " " (finite).	"
V	Volume of gas in test chamber.	cm³
μ	Mass arrival rate or total mass of molecules striking unit area.	gm/cm²·sec
ν	" departure " " total mass of molecules flowing through.	" " "